Università degli Studi di Palermo

Properties of the O_2 diffusion process in amorphous SiO_2 nanoparticles

G. Iovino

Ph.D Thesis

Palermo, Gennaio 2014

(S.S.D. FIS/01)

DIPARTIMENTO DI FISICA E CHIMICA

DOTTORATO DI RICERCA IN FISICA – XXIV CICLO

Supervisore: Dott. S. Agnello

Coordinatore: Prof. A. Cupane

Contents

Contents ii

Introduction iii

1 Background 1

1.1 Diffusive equilibrium . . . 1
1.2 Diffusion process . . . 4
1.2.1 Diffusion equation in a sphere . . . 6
1.2.2 Variable diffusion coefficient . . . 8
1.2.3 Temperature dependence of diffusion coefficient and solubility . . . 14
1.2.4 Measurement of the diffusion coefficient . . . 18
1.2.5 Non-Fickian diffusion . . . 21
1.2.6 Dependence of diffusion coefficient on size of molecules and structure of the medium . . . 21
1.3 Amorphous SiO_2 . . . 23
1.4 Properties of oxygen molecule . . . 26
1.5 Diffusion of O_2 in bulk silica . . . 28
1.6 Silica nanoparticles . . . 33
1.6.1 Effects of thermal treatments of silica nanoparticles . . . 36
1.6.2 O_2 in silica nanoparticles . . . 37

2 Materials and methods 41

2.1 Materials . . . 41
2.1.1 Commercial nanoparticles . . . 41
2.1.2 Laboratory nanoparticles . . . 43
2.2 Luminescence spectroscopy . . . 43
2.3 Raman spectroscopy . . . 45
2.4 Thermal treatments . . . 50
2.5 Determination of diffusion coefficient . . . 51
2.6 Determination of interstitial O_2 concentration . . . 53

3 Study of diffusion in AEOX50 **57**
3.1 Results . . . 57
3.1.1 Desorption kinetics . . . 57
3.1.2 Sorption and sorption-desorption kinetics . . . 58
3.1.3 Equilibrium concentration . . . 60
3.2 Discussion . . . 60
3.2.1 Diffusion kinetics . . . 60
3.2.2 Equilibrium concentration . . . 71
3.3 Conclusion . . . 74

4 Size dependence of diffusion process in fumed silica **78**
4.1 Results . . . 78
4.1.1 Desorption kinetics . . . 78
4.1.2 Sorption kinetics . . . 79
4.1.3 Equilibrium concentration . . . 84
4.1.4 Effect of amorphous structure of nanoparticles on the diffusion process . . . 85
4.2 Discussion . . . 86
4.2.1 Equilibrium concentration . . . 86
4.2.2 Diffusion kinetics . . . 90
4.3 Conclusion . . . 96

5 Dependence of diffusion process on surface chemistry in fumed silica **99**
5.1 Results . . . 99
5.2 Discussion . . . 103
5.3 Conclusion . . . 105

6 Diffusion process in silica particles produced by microemulsion method **106**
6.1 Results . . . 106
6.2 Discussion . . . 109
6.3 Conclusion . . . 113

7 Conclusions **114**

A Diffusion process in silica nanoparticles distributed by Sigma Aldrich **117**

B Origin of interstitial O_2 in as-received samples **121**

C List of related papers **123**

Bibliography **131**

Introduction

Amorphous silicon dioxide (a-SiO_2), or silica, is a relevant, widely used material in current technology due to its physicochemical properties. Indeed, properties such as radiation hardness, chemical resistance, high transparency in the Near-Infrared (NIR) and visible range of the electromagnetic spectrum, high dielectric constant and wide band gap make silica a very useful material for electronic and optical applications [1, 2, 3, 4, 5]. The relevant properties of silica are related both to its intrinsic structural features and to the presence of defects [1]. Indeed, defects, related for example to impurities such as interstitial molecules, could affect the material performances so the investigation of their physical behavior is fundamental for the material final use. In particular, due to the open structure of silica, small molecules can diffuse from environment into and through silica under working conditions compromising the material features. Effects related to interstitial molecules could be very important in presence of ionizing radiation in the environment or at high temperature due to the activation of chemical reactions able to deteriorate silica based devices [6]. On the other hand, for many years silica is considered a prototype material in the study of the properties of amorphous solids [1, 2] and the investigation of physical processes involving interstitial impurities under irradiation or upon thermal treatments is important from a strictly scientific point of view in addition to the above mentioned technological aspects [6].

The miniaturization on nanoscale of optical and electronics devices in which silica plays an important role, as well as in the case of microscale [4, 5], makes interesting the investigation of the physical properties of silica when one or more dimensions are reduced to nanoscale, indeed, at this limit the properties of a solid can show a strong dependence on its size. Furthermore, nanometer silica has a great importance not only in manufacturing of electronic and optical devices but also in many industrial fields and biomedical researches [7, 8, 9, 10]. Whereas in some of these applications the properties of pure silica are required, in other ones a functionalization is necessary to give to silica useful properties for specific applications. Since interstitial molecules can increase absorption and emission bands or, under certain working conditions, can react with silica matrix to give defects, the study of the diffusion process and of the solubility of interstitial molecules is useful either for applications in which these molecules can degrade silica based devices, or for ones in which they give interesting properties for

functionalization. In particular, the diffusion process of oxygen in nanometer silica is important because oxygen is a common element in the atmosphere and silica often is the material composing the shell in core-shell systems whose core properties can be damaged by oxygen molecules [11]. Moreover, diffusion of oxygen in silica is relevant even in the synthesis of materials as in the case of core-shell systems such as Si-SiO_2 ones. Indeed, such systems are produced by thermal oxidation of silicon nanoparticles and the growth of the oxide layer is related to the diffusion of oxygen through this latter [12, 13, 14].

Concerning the functionalization, interstitial oxygen molecules are optically active and this property can be used to obtain luminescence probes of nanometer size emitting in the NIR [15, 16]. In particular, the presence of interstitial oxygen can be achieved by means of thermal treatments of silica nanoparticles in oxygen atmosphere to induce the diffusion of the gas into and through the nanoparticles [15]. In this respect, the dependence of diffusion process on thermodynamic parameters of the treatment, such as pressure and temperature, is important in order to optimize the functionalization procedure. Moreover, the dependence on the synthesis method of the nanoparticles and their morphological features have to be investigated to clarify if they can be of any relevance.

Apart from this technological point of view, the study of the diffusion process in nanometer silica allows to investigate the role of the size in the diffusion process and of some structural properties of silica nanoparticles that have been shown to be size dependent [17, 18, 19, 20, 21, 22, 23, 24]. Moreover, the study of the oxygen diffusion in silica nanoparticles makes possible to extend the range of temperature in which this process has been investigated until now. Indeed, whereas oxygen diffusion in silica is a well investigated topic at temperature above 500°C for external pressure of diffusing gas below 3 atm, no experimental data exist at lower temperature due to small values of the diffusion coefficient below 500°C that makes the diffusion process in bulk silica too slow to be investigated in laboratory times. On the other hand, in the case of silica nanoparticles, the small size reduces the diffusion time making possible to investigate the diffusion process at temperature below 500°C.

Basing on the above reported points of interest, in this thesis, the diffusion process of interstitial oxygen was investigated in nanoparticles of silica in the temperature range below 250°C and pressure from 0.2 bar up to 76 bar. The study was carried out on silica nanoparticles differing in synthesis methods, size, network structure, internal porosity and surface chemistry and morphology. This wide range of parameters has enabled to highlight many aspects of the dynamics of diffusion both from a physical and an applicative point of view, shedding new light on the diffusion process and on the nanomaterials investigations.

This thesis is organized as follows:

• The chapter 1 is an overview on the physics of the diffusion, the properties of silica, silica nanoparticles and oxygen molecules in silica and on the actual knowledge on the diffusion of oxygen in bulk silica.

• The investigated materials and the experimental techniques used to study the diffusion process are described in chapter 2.

• The chapter 3 deals with the diffusion of oxygen in fumed silica with average radius of primary nanoparticles equal to 20 nm.

• The study of the diffusion process in fumed silica with radii of primary nanoparticles smaller than 20 nm is reported in chapter 4.

• In chapter 5, the influence of the surface morphology and surface chemistry on the diffusion process are investigated.

• The diffusion process in silica nanoparticles synthesized by microemulsion method is discussed in chapter 6.

• The main conclusions are resumed in the chapter 7.

A list of published articles related to results contained in this thesis is reported at the end.

Chapter 1

Background

1.1 Diffusive equilibrium

When a solid or a liquid is put in a given atmosphere, molecules of the gas enter into it until an equilibrium state is reached. This latter depends on the interaction between the host material and the guest molecules and on the thermodynamic conditions such as temperature and pressure of the gas. In the experiments reported in this thesis the host system is silica put in O_2 atmosphere inside a container of fixed volume held at a given temperature. In order to analyze its thermodynamic behavior, the system can be schematized as depicted in Fig. 1.1.

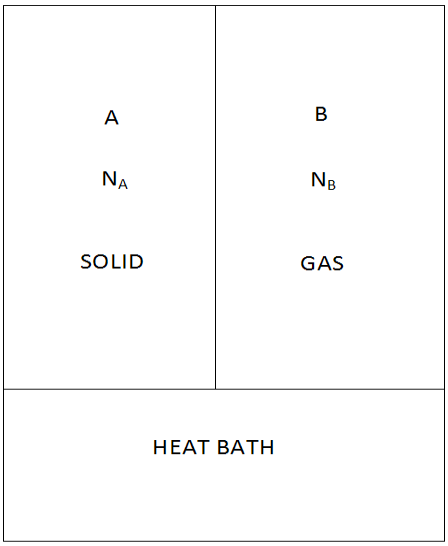

Figure 1.1: Schematic representation of a solid system at the diffusive equilibrium with a gas. A represents the solid in which molecules of the gas phase B are dissolved. N_A and N_B are the numbers of dissolved molecules in solid and in gas phase, respectively. Solid and gas are held at constant temperature by a heat bath.

The part A represents a solid, silica in our case, the part B the gas phase, O_2 in our

case. N_A and N_B are the numbers of molecules dissolved in the solid and in the gas phase, respectively. Molecules can enter into the A part or exit from it so the numbers N_A and N_B can change with the constraint that their sum is constant. N_A and N_B change until the number of molecules outgoing from the part A per unit time is equal to the incoming ones. When this condition is achieved, diffusive equilibrium is attained. N_A and N_B at the diffusive equilibrium are given by the minimum of Helmholtz free energy of the system defined as [25]

$$F = U - T\sigma = F_A + F_B \tag{1.1}$$

where T is the temperature, U is its internal energy, σ the entropy and F_A and F_B the Helmholtz free energies of the part A and B, respectively. In a transformation in which temperature and volume are constant, the differential of free energy for the system of Fig. 1.1 can be written as

$$dF = \frac{\partial F_A}{\partial N_A} dN_A + \frac{\partial F_B}{\partial N_B} dN_B \tag{1.2}$$

and using the constraint N_A+N_B = constant, it can be written in the form

$$dF = (\frac{\partial F_A}{\partial N_A} - \frac{\partial F_B}{\partial N_B}) dN_A \tag{1.3}$$

since at equilibrium F has a minimum, dF must be equal to zero, that is

$$\frac{\partial F_A}{\partial N_A} = \frac{\partial F_B}{\partial N_B}. \tag{1.4}$$

The derivative of F with respect to the number of particles is the chemical potential, so the diffusive equilibrium state is reached when chemical potential of the molecules in gas phase is equal to the one of molecules dissolved in the solid whereas, if this condition is not fulfilled, there is a flux of molecules towards the part of the system where the chemical potential is lower. The equality between chemical potentials determines the numbers of molecules in the two parts of the system. For a given solid and gas, these numbers depend on temperature and pressure of the gas due to the dependence of the chemical potential on these thermodynamic variables. In particular, the concentration of dissolved molecules at a given temperature is proportional to the external pressure in the limit of dilute system; this finding is expressed by the eq. 1.5, known as Henry's law [26]

$$C = SP \tag{1.5}$$

where C is the concentration of dissolved molecules, P is the external pressure and the constant S is the solubility of the gas in the solid.

Henry's law no longer applies at high concentration when the number of dissolved molecules tends to be independent on the external pressure [27]. This behavior can be accounted by a simple model supposing that only a finite number of sites of the solid can be occupied by molecules and that the entering rate is proportional to the external pressure and to the number of available sites not yet occupied. This model, known as Langmuir model, was first developed for absorption on a surface but can be applied also to a three-dimensional solid [26]. The variation of the concentration of dissolved molecules per unit time due to absorption can be written as $\frac{(C_{max}-C)}{C_{max}}k_{in}P$, where C_{max} and C are the maximum and the actual concentrations of absorbed molecules, k_{in} is the absorption rate constant and P is the external pressure, that is proportional to external concentration of molecules. The variation of the concentration of absorbed molecules per unit time due to the desorption can be written as $-k_{out}C$, where k_{out} is the desorption rate constant and C is the actual concentration of absorbed molecules. The rate equation governing the process is

$$\frac{d}{dt}C = -k_{out}C + \frac{(C_{max} - C)}{C_{max}}k_{in}P. \tag{1.6}$$

The stationary solution of eq. 1.6 gives the Langmuir isotherm (eq. 1.7) [28, 29, 30, 31, 32, 33, 34]

$$C(P) = \frac{SP}{1 + \frac{S}{C_{max}}P} \tag{1.7}$$

where $C(P)$ and C_{max} are the concentrations of dissolved molecules at external pressure P and its maximum value, respectively, and $S = \frac{k_{in}}{k_{out}}$ is a constant, depending on temperature, corresponding to the solubility of Henry's law. According to eq. 1.7, the concentration increases on increasing the pressure. If $\frac{S}{C_{max}}P \ll 1$, eq. 1.7 takes the same form as Henry' law whereas if $\frac{S}{C_{max}}P \gg 1$, $C = C_{max}$ independently on the external pressure.

Until now the equilibrium between the part A and B of the system of Fig. 1.1 was dealt. Now, let us consider the part A of the system by dividing it in several subsystems. At the initial stage of the dissolution process only the subsystems near to the surface contain dissolved molecules so there is a difference in the chemical potential among the subsystems in which A was divided. Obviously, this is not the equilibrium condition and the difference in the chemical potential among the subsystems, or its gradient, produces a flux of molecules until the gradient of the chemical potential is zero over all the system [25]. The gradient of the chemical potential, or equivalently the gradient

of the concentration if A is homogeneous, is the driving force that drives the system toward the equilibrium state by means of a transport process named diffusion [25] that will be discussed in the next paragraphs.

1.2 Diffusion process

The diffusion is a transport process of the matter due to random molecular motion [35]. Suppose to have a solution in which the solute is initially confined only in a region of the solvent. If the concentration is low enough, dilute solution, the molecules of the solute move independently on each other following a random walk that is the consequence of molecular collisions with molecules of the solvent. Due to the randomness of this motion, only the mean square distance traveled by the molecule in a given time interval can be predicted but nothing can be said about the direction of the motion. The randomness of the motion of each molecule results in a transfer of solute from the part of the solution in which it was initially confined to the whole solution until a uniform concentration is reached. In general, during the diffusion process there is a transport of matter from the part of the system in which the concentration is higher towards the lower concentration parts. To understand how a net flux of matter can result from the random walk of each molecule, consider the case in which there is a gradient in the concentration along a given direction. The number of molecules traveling a surface perpendicular to this direction in a given time interval is different from zero because even if all directions are equally probable, the concentration is higher on a side of the surface. Indeed, a molecule has the same probability to cross the surface independently on the concentration but the greater concentration in a side results in a greater number of molecules traveling the surface from this side towards the lower concentration one. This concept was first realized by Fick [36] who studied the diffusion process in a quantitative way by using the equation governing the conduction of the heat. In particular, Fick supposed the flux of matter in a given direction to be proportional to the gradient of its concentration:

$$\mathbf{F} = -D\mathbf{grad}C \tag{1.8}$$

where $\mathbf{F}$ is the flux density of the matter in a point of the system, that is the number of molecules crossing in the unit time a unitary surface perpendicular to the gradient, $\mathbf{grad}C$, of the concentration of diffusing substance, C, in that point and D is the diffusion coefficient. The minus sign on the right side of the equation takes into account that the flux is towards lower concentration region. Furthermore, according to eq. 1.8, the flux in a given point is perpendicular to the surface of constant concentration in this point. In order to obtain the differential equation describing the time and spatial

evolution of concentration, the conservation law of mass has to be taken into account

$$\frac{\partial C}{\partial t} = -div\mathbf{F} \tag{1.9}$$

where **F** is the flux density at a given point of the system, C is the concentration of diffusing substance at this point and *div* is the divergence operator. By substituting eq. 1.8 in eq. 1.9 and supposing the system homogeneous so that the diffusion coefficient is independent on spatial coordinates, the differential equation of the diffusion is obtained:

$$\frac{\partial C}{\partial t} = D\nabla^2 C \tag{1.10}$$

where $\nabla^2 = div\mathbf{grad}$ is the Laplacian operator. According to this equation the concentration at every point of the system satisfies eq. 1.10 and the boundary conditions. In particular, at the stationary state the concentration must satisfy eq. 1.11

$$\nabla^2 C = 0. \tag{1.11}$$

For example, in the case of diffusion of solute initially unevenly distributed in a solution, the stationary state is reached when the spatial distribution is uniform and the flux is zero everywhere. On the other hand, let us consider a plane sheet at whose ends different concentrations of diffusing substance are held. For this case, in the stationary state there is a gradient of the concentration and a non zero flux.

So far only homogeneous and isotropic systems were dealt. If the system is not homogeneous the differential equation governing the diffusion takes the following form [35]:

$$\frac{\partial C}{\partial t} = div(D\mathbf{grad}C). \tag{1.12}$$

If instead the system is homogeneous but not isotropic, the previous equations are not valid and must be substituted by a more general equation in which the flux along a given direction depends even on components of the concentration gradient orthogonal to this direction [35]. This refinement can be attained by the equation

$$\frac{\partial C}{\partial t} = D_{ij}\frac{\partial^2 C}{\partial x_i \partial x_j}. \tag{1.13}$$

In this equation, valid in the homogeneous case, the dependence of the diffusion coefficient on the direction is accounted by introducing the 3×3 diffusion matrix whose elements are D_{ij}, whereas $\frac{\partial^2 C}{\partial x_i \partial x_j}$ are the second partial derivatives with respect to spatial coordinates ($i, j = 1, 2, 3$). The diffusion matrix is usually not diagonal but there is

always a geometrical transformation which makes it diagonal (transformation to rectangular coordinates). Moreover, with a further transformation consisting in dividing each rectangular coordinate by the square root of the diffusion coefficient along it, the diffusion equation assumes the same form as in the isotropic case [35].

1.2.1 Diffusion equation in a sphere

Consider a diffusion process in a homogeneous sphere. In this case it is appropriate to write the differential equation of diffusion in spherical coordinates in order to simplify the solution process. In spherical coordinates eq. 1.10 takes the form

$$\frac{\partial C}{\partial t} = D[\frac{1}{r^2}\frac{\partial}{\partial r}(r^2\frac{\partial C}{\partial r}) + \frac{1}{r^2 sin\theta}\frac{\partial}{\partial \theta}(sin\theta\frac{\partial C}{\partial \theta}) + \frac{1}{r^2 sin^2\theta}\frac{\partial^2 C}{\partial^2 \phi}] \tag{1.14}$$

where r is the distance from the origin of the reference frame (the center of the sphere) and θ and ϕ are the polar and azimuthal angles, respectively.

In the particular case of radial diffusion, the concentration is only a function of r and t so derivatives with respect to angular coordinates are zero and eq. 1.14 becomes

$$\frac{\partial C(r,t)}{\partial t} = D\frac{1}{r^2}\frac{\partial}{\partial r}(r^2\frac{\partial C(r,t)}{\partial r}). \tag{1.15}$$

In the following, the solution of eq. 1.15 will be determined in the case of uniform initial concentration C_i in a sphere and supposing that the concentration on the sphere surface has a time independent value C_f equal to the equilibrium value inside the sphere at the end of the diffusion process. The initial and the boundary conditions are mathematically expressed by

$$C(r < a, t = 0) = C_i \tag{1.16}$$

$$C(r = a, t) = C_f \tag{1.17}$$

where a is the radius of the sphere. Defining the auxiliary function $u(r,t)$ as [35]

$$u(r,t) = rC(r,t) \tag{1.18}$$

the differential equation 1.15 and the initial and boundary conditions transform in:

$$\frac{\partial u(r,t)}{\partial t} = D\frac{\partial^2 u(r,t)}{\partial r^2} \tag{1.19}$$

$$u(r < a, t = 0) = rC_i \tag{1.20}$$

$$u(r = 0, t) = 0 \tag{1.21}$$

$$u(r = a, t) = aC_f \tag{1.22}$$

This differential equation can be solved by the method of separation of variables consisting in considering a solution of the form

$$u(r, t) = T(t)R(r) + Er + F \tag{1.23}$$

where T and R are functions only of time t and spatial coordinate r, respectively, and E and F are two constants that have to be determined by initial and boundary conditions. By substituting the function given in eq. 1.23 in the differential equation 1.19, due to the independence between time and spatial variables [37], it is found that

$$\frac{1}{DT}\frac{\partial T}{\partial t} = \frac{1}{R}\frac{\partial^2 R}{\partial r^2} = -\lambda^2 \tag{1.24}$$

where λ is a constant to be determined. The forms of the T function (not giving time divergence) and of R function satisfying eq. 1.24 are respectively:

$$T = e^{-\lambda^2 Dt} \tag{1.25}$$

$$R = Acos(\lambda r) + Bsin(\lambda r). \tag{1.26}$$

Since eq. 1.19 is linear, a linear superposition of solutions of the form 1.23 is also a solution so the most general solution of eq. 1.19 is:

$$u = \sum_n (A_n cos(\lambda_n r) + B_n sin(\lambda_n r))e^{-\lambda_n^2 Dt} + Er + F \tag{1.27}$$

where the constants A_n, B_n, E, F and λ_n have to be determined by the initial and boundary conditions. The boundary condition in eq. 1.21 gives

$$\sum_n A_n e^{-\lambda_n^2 Dt} + F = 0 \tag{1.28}$$

that is satisfied if $A_n = F = 0$. By applying the boundary condition in eq. 1.22, the following equation is obtained

$$\sum_n B_n sin(\lambda_n a)e^{-\lambda_n^2 Dt} + Ea = aC_f \tag{1.29}$$

which is satisfied only if $\lambda_n = \frac{n\pi}{a}$, where n is a positive integer number, and $E = C_f$.

Taking into account the values found for all the constants and eq. 1.18, the solution for the concentration is:

$$C = \sum_{n=1}^{\infty} \frac{B_n}{r} sin(\frac{n\pi r}{a}) e^{-\frac{n^2\pi^2 Dt}{a^2}} + C_f. \tag{1.30}$$

The values of the B_n constants has to be determined by the initial condition of eq. 1.16. In particular, the substitution of eq. 1.30 in eq. 1.16 gives

$$\sum_{n=1}^{\infty} \frac{B_n}{r} sin(\frac{n\pi r}{a}) + C_f = C_i. \tag{1.31}$$

Multiplying both sides of eq. 1.16 by $rsin(\frac{m\pi r}{a})$ and integrating over r from 0 to a, only a term of the sum is non zero due to the orthogonality of the sin functions [37], and the value of each B_n constant can be calculated obtaining

$$B_n = (-1)^n (C_f - C_i) \frac{2a}{n\pi}. \tag{1.32}$$

by this procedure the solution obtained for eq. 1.15 with the conditions 1.16 and 1.17 is

$$C = \sum_{n=1}^{\infty} (-1)^n (C_f - C_i) \frac{2a}{n\pi r} sin(\frac{n\pi r}{a}) e^{-\frac{n^2\pi^2 Dt}{a^2}} + C_f. \tag{1.33}$$

A plot of the solution 1.33 relative to a sphere initially empty is shown in Fig. 1.2. The concentration inside the sphere changes until it reaches the uniform value C_f. It is worth noting that no hypothesis was made about the values of initial and final concentrations. The solution 1.33 is valid either in the case of $C_i > C_f$ or vice versa, the only difference being that in the former case the diffusing substance leaves the sphere whereas in the latter one it enters into the sphere. Moreover, the boundary condition 1.17 is an idealization because the adsorption process on the surface takes a finite time. Obviously this approximation is good as long as the diffusion process is much slower than the adsorption one.

1.2.2 Variable diffusion coefficient

In the previous paragraph, the diffusion equation was solved in an isotropic and homogeneous sphere. In the inhomogeneous case, a dependence of the diffusion coefficient on the spatial variables has to be taken into account. Furthermore, the diffusion coefficient could depend even on the concentration [35]. In general, physical systems in which the diffusion is either space or concentration dependent are hard to treat analytically so the diffusion equation has to be solved by means of numerical methods. When the diffusion

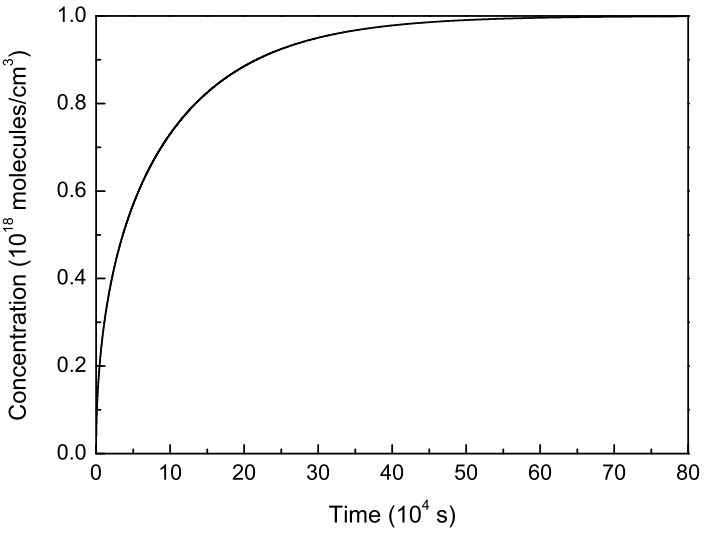

Figure 1.2: Solution of Fick's diffusion equation in an initially empty sphere of 200 cm radius. The solution is determined for D = 4 cm^2/s and $C_f = 10^{18}$ molecules/cm^3.

coefficient is not constant the Fick's diffusion equation 1.10 takes the form 1.12. In the following some solutions of the diffusion equation with variable D in one-dimensional systems will be discussed.

Suppose to have a plain sheet of finite thickness and infinite surface. In such a system the diffusion is one-dimensional in the direction perpendicular to the plane. If D is constant and the concentrations at the ends of the sheet are held fixed at different values, the steady state solution gives a linear dependence of the concentration on the position inside the membrane. On the other hand, if the diffusion coefficient is variable the dependence of the concentration on the spatial variables is tightly related to the functional dependence of the diffusion coefficient on both concentration and spatial coordinates. Fig. 1.3 shows some calculated results for stationary state obtained by using numerical techniques in the case of diffusion across a plain sheet of thickness l when the diffusion coefficient depends on the concentration following the law $D = D_0(1 + aC)$ with a values as reported in the caption of the figure. The above cited case of constant diffusion coefficient is also shown with label (4) [38].

From the figure it can be seen that if the diffusion coefficient increases as the concentration increases the steady state distributions are concave whereas are convex if the diffusion coefficient decreases on increasing the concentration. Moreover, if the diffusion coefficient has a maximum there will be an inflection point in the distribution. Even if the concentration distributions reported in the figure are relative to particular dependencies of the diffusion coefficient on the concentration, they illustrate a general

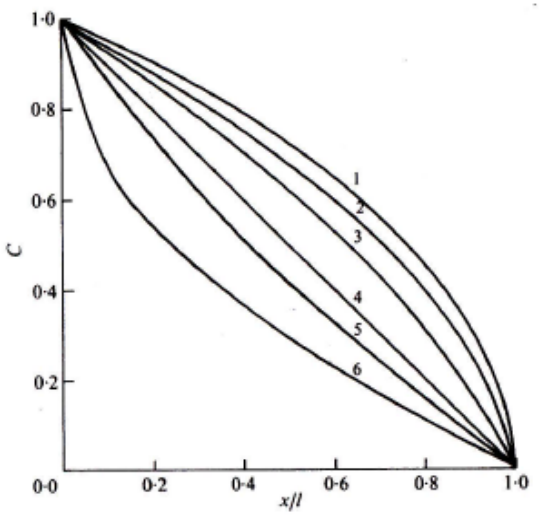

Figure 1.3: Steady state distributions of the concentration of a diffusing substance in a plain sheet of thickness l and having concentration dependent diffusion coefficient, when the surface concentrations are held at 0 and 1 at $x = l$ and $x = 0$, respectively. The dependence of D on the concentration is given by the law $D = D_0(1 + aC)$ with $a = 100$ (1), $a = 10$ (2), $a = 2$ (3), $a = 0$ (4), $a = -0.5$ (5) and $a = -1$ (6). Adapted from Ref. [35].

aspect of the steady state.

Similar statements can be made if the diffusion coefficient is position dependent. The steady state distributions relative to permeation across a plain sheet in which the diffusion coefficient is position dependent are shown in Fig. 1.4. In particular, the curves are relative to permeation of a plain sheet of thickness l with fixed concentration at its ends and having diffusion coefficient depending on the position according to the equations reported in the caption of the figure.

If the diffusion coefficient depends both on concentration and position, in general the diffusion depends on the direction. If the boundary conditions at the ends of the plain sheet are exchanged, the direction of the flux changes as well as its value [39]. In non-steady state no general statements as the previous can be made about the shape of the concentration distribution or its time evolution. In particular, the shape of the concentration distributions at each given time is strictly related to the functional dependence of the diffusion coefficient and on the boundary conditions [40]. In the following, some results obtained by means of numerical methods are reported. The shown curves are obtained by solving sorption and desorption problems in one-dimensional semi-infinite system. The system is a medium infinite along the y and z directions and semi-infinite along the x direction, extending to the positive x-axis. In sorption,

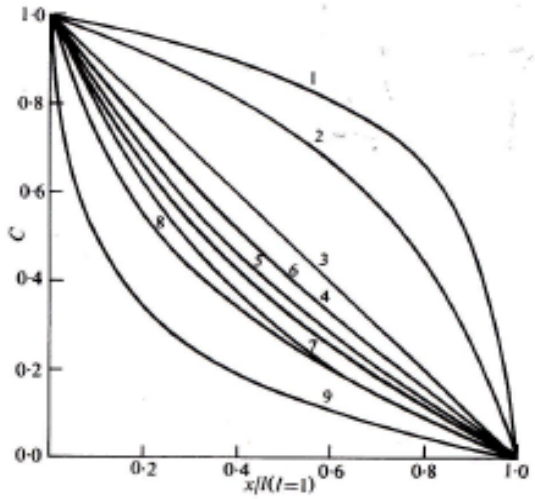

Figure 1.4: Steady state distributions of the concentration of a diffusing substance in a plain sheet of thickness l and space dependent diffusion coefficient when the surface concentrations are held at 0 and 1 at $x = l$ and $x = 0$, respectively. The dependence on the concentration is given by the law $D = D_0(1 + f(x))$ with $f(x) = -0.99x$ (1), $f(x) = -0.9x$ (2), $f(x) = 0$ (3), $f(x) = x$ (4), $f(x) = 2x$ (5), $f(x) = x^2 + 2x$ (6), $f(x) = 2.25x^2 + 3x$ (7), $f(x) = 9x$ (8)and $f(x) = 99x$ (9). Adapted from Ref. [35].

concentration is fixed to C_0 at $x = 0$ whereas it is initially zero inside the medium and increases with time. In desorption, concentration is constantly zero at $x = 0$ whereas it is initially C_0 inside the medium and decreases with time. In this geometry and under these boundary conditions, the concentration can be written as a function of $\frac{x}{(D_0 t)^{1/2}}$, where D_0 is a constant having the dimensions of a diffusion coefficient. Fig. 1.5 shows the concentration inside the medium as a function of $\frac{x}{(D_0 t)^{1/2}}$ when the diffusion coefficient depends exponentially on the concentration in a sorption experiment. The quantity reported on the x-axis is proportional, at a given time, to the spatial variable so the curves have the same shape as the concentration distributions. Unlike the distributions in steady state case, there is a change of concavity even if the diffusion coefficient changes monotonically with the concentration.

When the diffusion coefficient depends on the concentration, sorption and desorption have different rates, unlike the case of constant diffusion coefficient. In particular, the fractional variation of mass of diffusing substance inside the medium at a given time t does not depend on the process (sorption or desorption) if D is constant whereas it does if D is variable [35]. Fig. 1.6 shows the fractional variation of mass of diffusing substance for sorption and desorption when D depends on concentration as reported in the legend of the figure in the case of a plain sheet of thickness l at whose surfaces

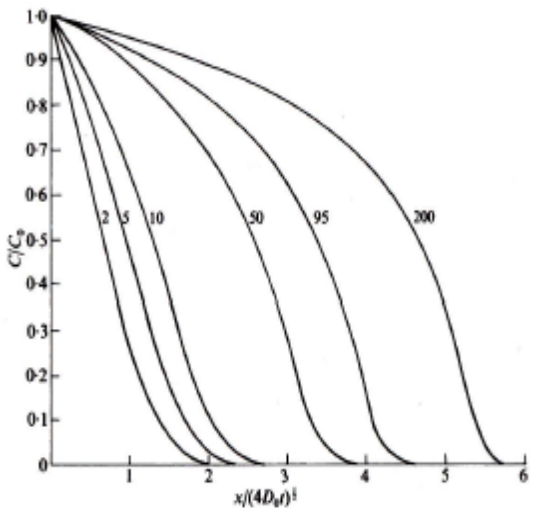

Figure 1.5: Normalized distributions of the concentration of a diffusing substance, $(\frac{C}{C_0})$, in a semi-infinite medium extending in the region $x > 0$ in a sorption experiment when the diffusion coefficient depends on the concentration according to the law $D = D_0 e^{\frac{kC}{C_0}}$. Numbers on the curves are the values of e^k. Adapted from Ref. [35].

a constant value of concentration is held [41]. In general, curves for sorption and desorption are different but coincide if D is a symmetrical function under exchange of C with $C_0 - C$ ($C_0 = 1$ in this case) as in the case of the dependence (i). In Fig. 1.6 it is also evident that no general statements can be made about the relative rate of sorption and desorption. Indeed, for the law (ii) desorption is faster than sorption whereas for the law (iii) sorption is faster than desorption. It is worth noting that if C is changed to $1 - C$ in the law (ii), the law (iii) is obtained and sorption for (ii) coincides with desorption of (iii) and vice versa. Moreover, if the diffusion coefficient has a maximum, sorption and desorption curves could intersect depending on the position of the maximum.

Till now, some results were reported about variable diffusion coefficient in non-steady state if D depends on the concentration only. Now an example of spatial dependence will be considered. In particular, the diffusion in a composite cylinder will be discussed. The medium is a cylinder infinite along its axis so that only radial diffusion has to be considered. The cylinder is composed by an internal cylinder of radius b and a cylindrical shell of thickness $a - b$. The diffusion coefficients in the two regions, D_b in the core part and D_a in the shell one, are different. This problem was solved numerically in the case in which the cylinder is immersed in a solution containing the diffusing molecules and supposing the concentration of the solution to be uniform at

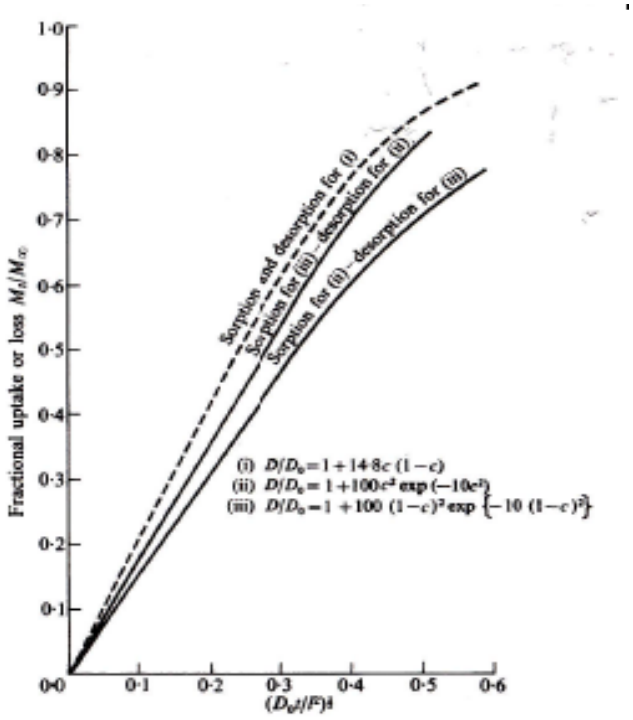

Figure 1.6: Fractional variation of mass of a diffusing substance inside a plain sheet of thickness l in sorption and desorption experiments when the diffusion coefficient, D, depends on the concentration as follows: (i) $D/D_0 = 1 + 14.8c(1-c)$, (ii) $D/D_0 = 1 + 100c^2 exp(-10c^2)$, (iii) $D/D_0 = 1 + 100(1-c)^2 exp(-10(1-c)^2)$. Adapted from Ref. [35].

every time [42]; this means that the diffusion of molecules in the solution is much faster than inside the cylinder. The solid lines drawn in Fig. 1.7 are the distributions of concentrations at different time when $\frac{D_b}{D_a} = 30$ whereas the dashed line is the distribution in the case of uniform cylinder with diffusion coefficient D_b. The numbers labeling the curves are values of $\frac{D_b t}{a^2}$, so for a given D_b, they are essentially a measure of the time. By comparing the dashed line, relative to $\frac{D_b t}{a^2} = 4$ and the solid one corresponding to $\frac{D_b t}{a^2} = 21$, it is evident that the diffusion is faster in the homogeneous cylinder due to the lower value of the diffusion coefficient in the shell in the composite cylinder. Moreover, a discontinuity in the derivative of the distribution is present at the boundary between the core and shell regions. By increasing the time the distribution in the core region becomes less sharp because the diffusion in this region is faster than in the shell. Opposite results are obtained if the diffusion coefficient is higher in the shell region [42].

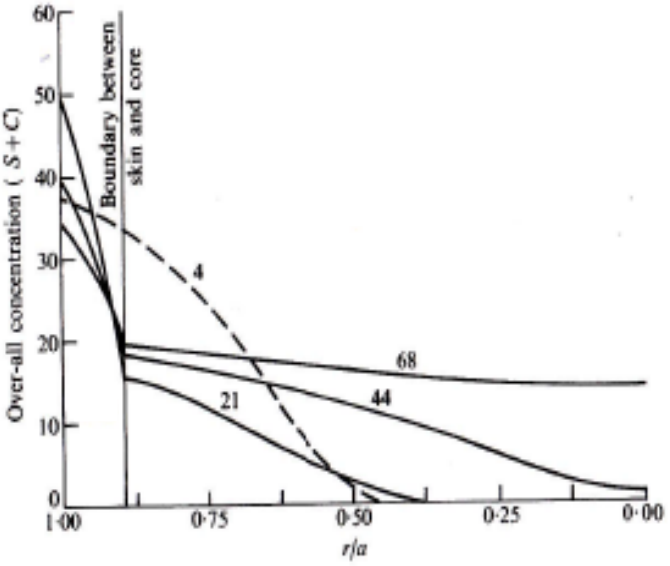

Figure 1.7: Concentration distributions in a homogeneous cylinder (dashed line) and in a composite one (solid lines). The homogeneous cylinder has radius a and diffusion coefficient D_b, whereas the composite cylinder is formed by a shell of thickness $a - b$, with diffusion coefficient D_a, and a core region of radius $b = \frac{9}{10}a$ with D_b. Solid lines are relative to $\frac{D_b}{D_a} = 30$. Numbers on curves are values of $\frac{D_b t}{a^2}$. Adapted from Ref. [35].

1.2.3 Temperature dependence of diffusion coefficient and solubility

It is experimentally known that the diffusion coefficient depends on temperature [26]. In some systems this dependence could be related to changes in the medium structure induced by temperature as in the case of polymers [35]. Apart from these complex systems, changes of the diffusion coefficient with temperature are observed even if the structure of the medium does not undergo changes due to temperature. In these systems the diffusion coefficient varies with temperature following an Arrhenius law:

$$D = D_0 e^{-\frac{E_a}{K_B T}} \tag{1.34}$$

where E_a is the activation energy, K_B the Boltzmann constant, T the absolute temperature and D_0 is the pre-exponential factor that is temperature independent. The Arrhenius law is strictly related to the temperature activated nature of the diffusion process [26, 25]. An activated process is one in which the system has to overcome an energy barrier to go from the initial to the final state. In general, such processes are characterized by temperature dependent rates that follow an Arrhenius law.

The diffusion process belongs to this class of phenomena because an interstitial

molecule has to overcome an energy barrier to jump from an interstice to another. The pre-exponential factor is related to geometrical factors whereas the temperature dependence is related to the increase of the population of molecules having energy greater than the activation one when the temperature is increased. In particular, the exponential dependence is related to the factor $e^{-\frac{E_a}{K_B T}}$. Indeed, the diffusion coefficient is proportional to the number of molecules able to overcome the energy barrier, and this number increases according to Boltzmann factor. Fig. 1.8 shows the energy distribution of molecules, that is proportional to Boltzmann factor, for two different temperatures (T_{low} and T_{high}) and illustrates what happens when the temperature of the system is increased.

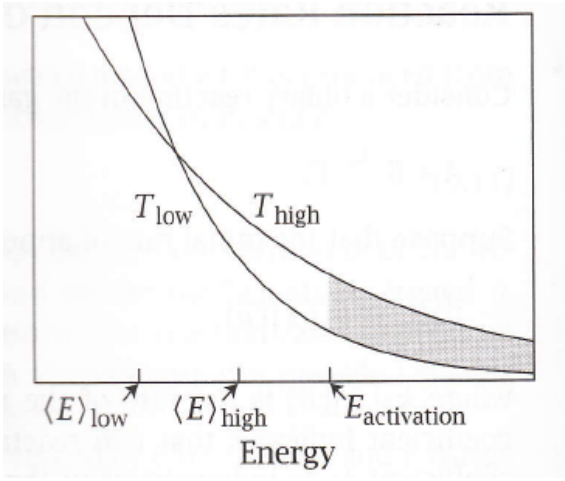

Figure 1.8: Qualitative energy distribution of molecules for two temperatures. $\langle E \rangle_{low}$ and $\langle E \rangle_{high}$ are the average energies at temperatures T_{low} and T_{high}, respectively, whereas $E_{activation}$ is the activation energy of the process. The shaded area represents the increase in the population of the states with energy greater than the activation one. Adapted from Ref. [26].

Since the average energy of diffusing molecules is proportional to temperature, an increase of this latter, that increases of a small amount the average energy, produces a relevant variation of the population of molecules able to overcome the energy barrier. This population relative to T_{low} is given by the area under the relative curve corresponding to $E > E_{activation}$ whereas the increase due to temperature variation is given by the area between the two curves in the region $E > E_{activation}$. In Fig. 1.8 is evident that the fractional variation of the population is much greater than that of the average energy. This strong dependence on temperature is a feature common to all activated

processes.

The Arrhenius law can be obtained even under the hypothesis that molecules must overcome an activation barrier of Gibbs free energy Δg [43] :

$$\Delta g = \Delta h - T\Delta\sigma \tag{1.35}$$

where Δh and $\Delta\sigma$ are the enthalpy and the entropy of activation, respectively, and T is the absolute temperature. Under this hypothesis, the diffusion coefficient is proportional to the factor $e^{-\frac{\Delta g}{K_B T}}$. In particular, for interstitial diffusion the law takes the form

$$D = \gamma\alpha^2\nu e^{\frac{\Delta\sigma}{K_B} - \frac{\Delta h}{K_B T}} \tag{1.36}$$

where α is the distance between two adjacent interstices, γ is a geometrical factor and ν is a frequency factor, K_B the Boltzmann constant and T the absolute temperature. By comparing eqs. 1.34 and 1.36 the following equalities are obtained:

$$D_0 = \gamma\alpha^2\nu e^{\frac{\Delta\sigma}{K_B}} \tag{1.37}$$

$$E_a = \Delta h \tag{1.38}$$

In many systems the diffusion coefficient follows the Arrhenius behavior in a wide range of temperature, as in the case of diffusion of a carbon atom in iron for which the diffusion coefficient follows the Arrhenius law over 14 orders of magnitude [44]. On the other hand, there are systems for which the experimental dependence of the diffusion coefficient fits better with a modified Arrhenius law in which a temperature dependence of the pre-exponential coefficient is introduced [45, 46].

$$D = D_1 T e^{-\frac{E_a}{K_B T}} \tag{1.39}$$

where D_1 is constant. The temperature dependence in the pre-exponential factor can be justified because the diffusion coefficient is proportional to the fraction of molecules having energy higher than the activation one. This fraction is proportional to the area below the Boltzmann factor for $E > E_a$

$$\int_{E_a}^{\infty} e^{-\frac{E}{K_B T}} dE = K_B T e^{-\frac{E_a}{K_B T}} \tag{1.40}$$

In some systems, such as glassy systems, both the pre-exponential factor and the activation energy are function of the experimentally explored temperature range [47].

These data can be fitted in the overall range by supposing that the pre-exponential factor depends on temperature whereas the activation energy is temperature independent [47, 48, 49, 50]. In some cases, it was supposed that the pre-exponential factor is proportional to the square root of temperature [48, 49]. On the other hand the departure from the Arrhenius law can be explained by introducing a distribution of the activation energy in the Arrhenius law due to the structural disorder in the glass [51]. In particular, a Gaussian distribution of the activation energy was supposed [51]:

$$n(E_a) = (\pi\epsilon^2)^{-\frac{1}{2}} e^{-\frac{(E_a - \langle E_a \rangle)^2}{\epsilon^2}} \tag{1.41}$$

where $n(E_a)$ is the sites distribution as a function of the activation energy, $\langle E_a \rangle$ is the mean activation energy and $\epsilon ln(2)^{\frac{1}{2}}$ is the HWHM of the distribution. Under this hypothesis the following expression is found for the diffusion coefficient [51]

$$D = \int_0^\infty n(E_a) D_0 e^{-\frac{E_a}{K_B T}} dE_a = D_0 e^{\frac{\epsilon^2}{4K_B^2 T^2}} e^{-\frac{\langle E_a \rangle}{K_B T}} \tag{1.42}$$

where the pre-exponential factor is temperature-dependent.

Like the diffusion coefficient, even the solubility changes with temperature following the Arrhenius law [26]:

$$S = S_0 e^{-\frac{\widetilde{E}_a}{K_B T}} \tag{1.43}$$

Solubility is given by the ratio between the equilibrium concentration and the external pressure (see eq. 1.5) so it is proportional to the ratio between the concentration of molecules inside and outside the medium. Solubility can be interpreted as the equilibrium constant of two "reactions": the forward reaction by which molecules from the gas phase enter in the medium and the backward reaction by which molecules leave the medium to return to the gas phase. Both these "reactions" are activated, but the activation energies are different. The equilibrium constant K of these "reactions" is given by the ratio between the forward and backward rate constants [26]:

$$K = \frac{K_f}{K_b} \propto e^{-\frac{E_f - E_b}{K_B T}} \tag{1.44}$$

where K_f and K_b are the forward and backward rate constants, respectively, E_f and E_b the activation energies of the forward and backward reactions, respectively, K_B is the Boltzmann constant and T is the absolute temperature. Coming back to diffusion, for analogy it can be written

$$S \propto \frac{C_{in}}{C_{out}} = \frac{K_f}{K_b} \propto e^{-\frac{E_f - E_b}{K_B T}} \tag{1.45}$$

where C_{in} is the equilibrium concentration of dissolved molecules and C_{out} is that of the molecules in the gas phase. By inspection, it can be seen that the activation energy in the Arrhenius law of the solubility corresponds to the difference between the energy barriers that molecules must overcome to enter or exit the medium and corresponds to the heat absorbed or released when a molecule dissolves in the medium. If $\widetilde{E}_a < 0$, that is $E_f < E_b$, the dissolution process is exothermic and the solubility increases on decreasing the temperature. Otherwise the process is endothermic and the solubility decreases on decreasing the temperature. The Arrhenius behavior of the solubility can also be derived by means of statistical mechanics directly by minimizing the Helmoltz free energy of the system but this derivation will not be treated in the present work [26].

1.2.4 Measurement of the diffusion coefficient

As shown in the previous paragraph, the diffusion coefficient is defined by the eq. 1.8. This definition is valid if diffusion takes place in a rigid medium. If diffusion is investigated in a two components system in which both components are mobile, two equations of the type of eq. 1.8 have to be considered to define the diffusion coefficient of each substance. However, if no change in volume occurs, the diffusion process is described by the Fick's diffusion equation 1.10 by using a mutual diffusion coefficient. By contrast, this equation cannot be used if the volume of the system varies during the diffusion process. However, in this case it is possible to substitute the differentiation with respect to spatial coordinates with the derivative with respect to some appropriate variables to obtain a differential equation formally equal to Fick's diffusion equation 1.10 [35, 52].

This thesis work deals with diffusion in a solid matrix that can be considered rigid so in the following only methods to measure the diffusion coefficient in such a system will be described. Diffusion coefficient can be measured by means of experiments under steady state conditions, during the transients or by the time-lag method that is a combination of the previous two methods [35]. In steady state conditions, the flux of the diffusing substance through a plane sheet, a spherical shell or a hollow cylinder is measured when the stationary state is reached. Usually, in these experiments the different concentrations on the two surfaces are kept fixed and the diffusion coefficient is determined by substituting the measured flux in the steady state analytical solution relative to the geometry of the used experimental system. By this method, it is easy to measure the diffusion coefficient if it is constant, whereas only an average value is obtained if this is not the case. However, methods to estimate the spatial and concentration dependence of D in steady state experiments were developed [53]. One of these methods consists in supposing that the diffusion coefficient can be written as the product of a function of concentration and a function of space. In this method, the flux is measured when the concentration is fixed at zero on a surface and either changing

the thickness of the medium with a fixed concentration on the other surface, or fixing the thickness and varying the concentration on this surface. The diffusion coefficient is then found by fitting the experimental results with the mathematical predictions arising from the assumed hypothesis.

Whereas in the steady state methods the flux at the stationary state is measured, in time-lag methods the behavior of the system approaching to this state is studied. Suppose to have, for example, a plane sheet that initially does not contain the diffusing substance. If a constant concentration of diffusing species is kept on a surface and a zero concentration on the other one, the flux will be zero until the substance covers the distance between the two surfaces, then it will increase until a constant value is reached. In this state the amount of diffusing substance crossing the plain sheet is a linear function of time. This behavior is illustrated in Fig. 1.9

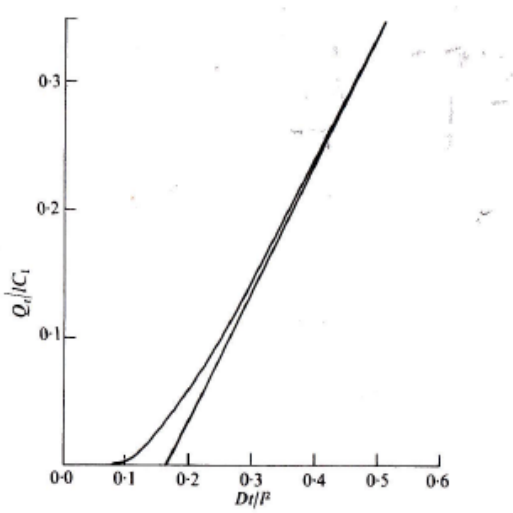

Figure 1.9: Time evolution of the mass of diffusing substance through a plain sheet (curve) of thickness l and diffusion coefficient D when the concentration is kept to zero on a surface and C_1 on the other one. Q_t is the quantity of substance that traveled the sheet at the time t. The straight line is the asymptote. Adapted from Ref. [35].

In the above described case the equation of the asymptote is

$$Q_t = \frac{DC_1}{l}(t - \frac{l^2}{6D}) \tag{1.46}$$

where Q_t is the mass that have traveled the plain sheet at time t, l is the thickness of the sheet, D the diffusion coefficient and C_1 the concentration on one of the surface of the sheet whereas on the other one the concentration is kept to zero. The time relative

to the intercept of the asymptote with abscissa axis (t_0) is named the time-lag and is given by

$$t_0 = \frac{l^2}{6D} \tag{1.47}$$

The diffusion coefficient is determined by eq. 1.47.

In general, when different concentrations are imposed on the edges of a medium, a flux of diffusing matter across the medium arises and it changes until the steady state is reached. Since the flux is constant at the steady state, the amount of matter traveling the medium per unit time is a linear function of time independently on the geometry of the system and on the dependence of the diffusion coefficient on concentration and spatial variables so the time-lag method can be applied to any system. In particular, if the diffusion coefficient is concentration dependent, an expression of the time-lag can be written by providing a functional form of the diffusion coefficient and the constant parameters in this form can be determined by measuring the time-lag for various boundary conditions by fitting the experimental data with the predicted law [54].

Diffusion coefficients can also be measured by studying the transient. In such experiments the distribution of diffusing matter inside the medium or the total amount of adsorbed or desorbed matter is measured as a function of time [55, 56]. The diffusion coefficient is then estimated by fitting the experimental data with the solution of the diffusion equation in the used experimental geometry and for the supposed dependence of the diffusion coefficient on concentration and position. Usually, as a first approximation, a constant diffusion coefficient is hypothesized. A dependence of the diffusion coefficient on the concentration can be revealed by repeating the diffusion experiment by changing the boundary conditions. For example, in a sorption experiment in which the medium is initially empty and the concentration at the surface is constant, the time dependence of the fractional amount of uptaken matter must not depend on the external concentration, and hence on the final one inside the medium, under the hypothesis of constant diffusion coefficient. If such a dependence is found, the diffusion coefficient is variable. If the experimental data relative to a system with concentration dependent diffusion coefficient are fitted with a mathematical law relative to a constant diffusion coefficient, the estimated value is an average value. In particular, the obtained diffusion coefficient is a good approximation of the integral [41]

$$\langle D \rangle = \frac{1}{C_0} \int_0^{C_0} D(C) dC \tag{1.48}$$

where C_0 is the final concentration in the medium.

The dependence of D on the concentration can be found by measuring the diffusion coefficient, supposed constant, at different values of C_0 (by changing the boundary

condition) and then by fitting this dependence with the integral 1.48. Moreover, a variable diffusion coefficient can be evidenced by sorption and desorption experiments made in a sequence. First an empty medium is loaded by imposing a fixed external concentration on its surface and, after the system reached the diffusive equilibrium, it is emptied by putting it under vacuum. If the diffusion coefficient is constant, the time dependence of the fractional mass of uptaken matter in the sorption and of lost matter during the desorption must be equal. A difference in time dependence between sorption and desorption experiments reveals a variable diffusion coefficient and provides a method to find the dependence law. Indeed, the average value between the diffusion coefficients measured in sorption and desorption experiments, under the hypothesis of constant diffusion coefficient, is a good approximation to the integral 1.48 [57, 58].

1.2.5 Non-Fickian diffusion

There are systems for which diffusion cannot be described by using the Fick's diffusion equation not even by introducing a dependence of diffusion coefficient on concentration and spatial variables. The diffusion in such systems is said non-Fickian or anomalous. A class of materials in which the diffusion can be anomalous are the polymers. Indeed, polymers can undergo structural changes due to temperature or to concentration of diffusing substance [59]. If the rate of relaxation of the medium is much faster than the rate of diffusion, the system can be treated as Fickian with good approximation. If this is not the case, the diffusion process is not Fickian and the structural changes have to be accounted by writing a differential equation for the diffusion coefficient which leads to a generalized diffusion equation different from the Fickian one.

1.2.6 Dependence of diffusion coefficient on size of molecules and structure of the medium

Diffusion coefficients of atoms and molecules in solids and liquids are strictly related to size of diffusing species, to that of the constituents of the medium in which diffusion occurs and to packaging of the atoms in it [43]. As a first approximation, atoms are supposed to be hard spheres. This approximation is good for metallic atoms for which the radius of the sphere can be determined by measuring the interatomic distance between the atoms in various solids and molecules [60]. This approximation can be extended even to ionic compounds in which the bonding is nondirectional as in the case of metallic bonding. On the other hand, atoms in covalent solids cannot be described as hard spheres due to strong variation of the size from a solid to another and to directionality of the covalent bonding [61, 62, 63]. In this case, two identical bound atoms can be considered as two hard spheres connected by a cylinder to take into account the distribution of the electrons along the direction of the bonding. If the two atoms are different, the space they occupy can be approximated by a truncated circular

pyramid with its symmetry axis along the bonding direction.

For what concerns the size of the dissolved atoms and molecules, a reliable method to calculate their size is by means of measurements of viscosity in the gas phase. If the diffusion of molecules is interstitial, as in the case of silicate glasses [46, 64, 65], it can be assumed that the activation energy in the Arrhenius law is equal to the work that a molecule must do to jump from an interstice to the adjacent one [66]. In particular, this work is equal to the energy required to expand the doorway connecting each interstice with the neighboring one so that the molecule can cross it. If the doorway is supposed to be a spherical cavity of radius r_d and the molecule to be an incompressible sphere of radius r, this energy is the elastic energy required to increase the radius of a spherical cavity in a liquid from r_d to r. This is given by [67]

$$E_a = 8\pi G r_d (r - r_d)^2 \tag{1.49}$$

where G is the elastic shear modulus of the medium. This equation was used to explain the dependence of the diffusion coefficient of different molecules and atoms in silica. Fig. 1.10 shows the dependence of the square root of the activation energy on the size of diffusing entities [46].

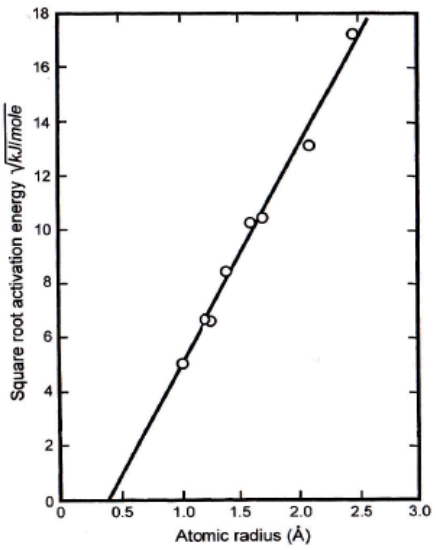

Figure 1.10: Dependence of the square root of activation energy on the radius of diffusing atoms and molecules in silica. Adapted from Ref. [43].

The linear trend of the experimental data suggests that the model is appropriate to describe the behavior of the diffusion coefficient, however, according to the found value

of the slope of the best line, the factor of 8 in eq. 1.49 should be changed in 4. This departure from the model was attributed to the uncorrected used value of the shear modulus G. Indeed, the value was calculated for a close-packed liquid and could be higher than that relative to the more open structure of silica.

1.3 Amorphous SiO_2

Silicon dioxide (SiO_2) exists in nature in various crystalline polymorphs [68] and in the amorphous form, named silica, characterized by the lack of spatial periodicity exhibited by crystalline polymorphs [69]. Silica can be easily obtained by quenching a melt to frozen atoms in the position they have in the liquid phase. Silica structure can be described by the continuous random network model [70, 71]. According to this model, silica is built up by corner-sharing SiO_4 tetrahedra.

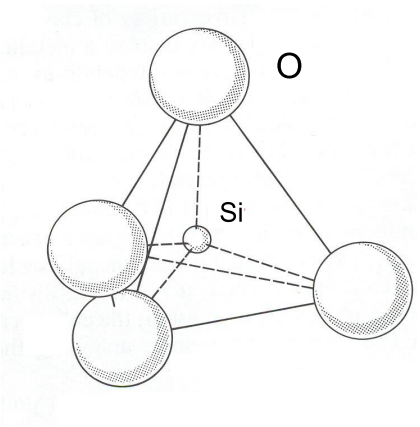

Figure 1.11: SiO_4 tetrahedron, the structural unit of silica network.

As depicted in Fig. 1.11, each SiO_4 tetrahedron contains one silicon atom at the center and four O atoms at the corners. This unit, that is the structural one in most SiO_2 polymorphs, is supposed to be the same as in the α quartz [68]. In particular the O-Si-O angle is 109.5° and each O atom is bound to two Si ones forming one short-bond and one long-bond whose bond-lengths are 0.1608 and 0.1611 nm, respectively [72]. Unlike crystalline polymorphs, tetrahedra are randomly connected in silica so the resulting structure is not periodic as evidenced by X-ray diffraction and neutron scattering experiments [1, 73] and the structure of silica cannot be described by few parameters as in the case of crystals.

The silica structure is described by referring to structural order in four different spatial ranges [74, 75]. The range I involves the fundamental structural unit (SiO_4 tetrahedron). The parameters describing the structure in this range are the distribution of O-Si-O angle and bond-lengths. The range II involves the connection between two corner-sharing tetrahedra. The order in this range is related to the distribution of the Si-O-Si angle and that of the dihedral angles describing the relative orientation of two adjacent tetrahedra when the Si-O-Si angle is fixed. The range III regards the network topology and involves several tetrahedra. In this range the silica structure can be studied by means of the ring statistics. A ring is defined as the shortest path along Si-O bonds starting from and ending on the same Si atom and is named with the number of Si atoms in the ring. The ring statistic deals with the distribution of the ring size. The range IV involves the density fluctuations on a scale length of several nanometers.

Experimental diffraction data are compatible with the structural model according to which silica is built up by a fundamental structural unit, equal to that of α quartz, sharing corners with other units. The connection between two tetrahedra in silica can be described by supposing the dihedral angles uniformly distributed and the Si-O-Si angle distributed as shown in Fig. 1.12 [69].

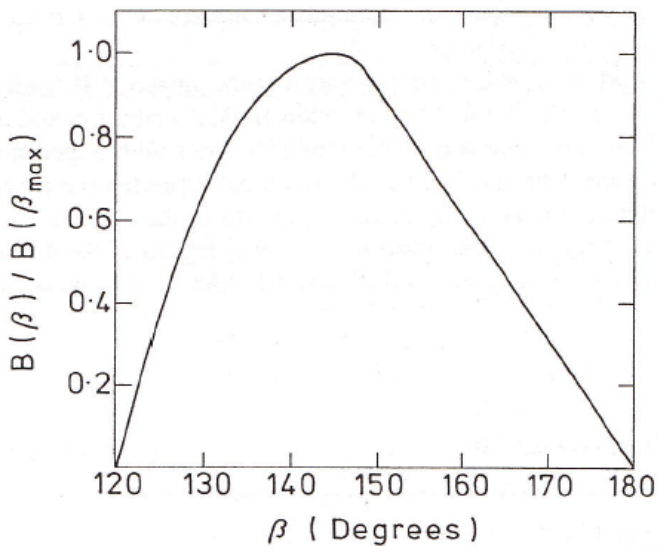

Figure 1.12: Distribution of the Si-O-Si bond angle (β). Adapted from Ref. [1].

For what concerns the ring statistics, the comparison between simulative works and experimental data suggests that the most probable rings are the six-membered ones. Moreover, the smaller rings (three and four-membered) are energetically unfa-

vorable [76].

Fig. 1.13 shows a typical Raman spectrum of a pure silica bulk sample. The band peaked at 440 cm^{-1} is attributed to the bending motion of O atoms in rings with more than four members and is usually named the R-band [77, 76, 78]. The lines at 490 and 605 cm^{-1} are related to the breathing vibration modes of 4-membered and 3-membered rings and are usually named D1 and D2 bands, respectively [77, 76, 78]. The bands at 800, 1065 and 1200 cm^{-1} are associated to the stretching vibration modes of the Si-O-Si bonds [77, 79].

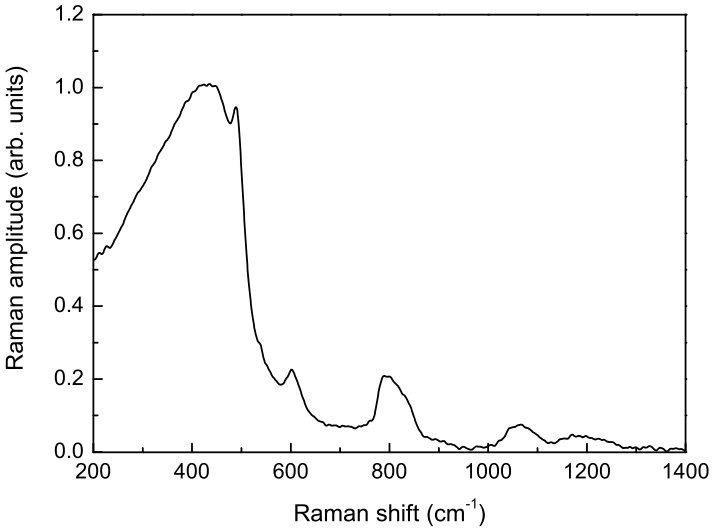

Figure 1.13: Typical Raman spectrum of bulk silica.

A departure from the structure predicted by the continuous random network model that decreases the order of the silica matrix is defined as a defect [1]. Defects in the material are related to manufacturing and post-manufacturing processes such as irradiation or thermal treatments [1]. Defects are said extrinsic if they involve impurity atoms, otherwise they are named intrinsic. Typical defects are broken bonds, impurity atoms bound to the matrix or interstitial impurities [80]. Common extrinsic defects in silica are the silanol groups (SiOH). The silanol content affects the properties of silica: it changes viscosity, density, refraction index and limits the optical transparency in infrared region [81, 82, 83, 84]. Silanol groups are present in various configurations: they can be isolated inside the matrix or in interacting hydrogen bonded pairs [85]. Silanol concentration is related to the manufacturing process and can be changed by post-synthesis thermal treatments [86]. One of the most common interstitial impurities in silica are O_2 molecules whose properties will be treated in the next paragraphs.

1.4 Properties of oxygen molecule

Oxygen molecule (O_2) is a diatomic molecule whose ground electronic configuration, in terms of molecular orbitals calculated by the LCAO method (Linear Combination of Atomic Orbitals), is $(1\sigma_g^+)^2(1\sigma_u^+)^2(2\sigma_g^+)^2(2\sigma_u^+)^2(3\sigma_g^+)^2(1\pi_u)^4(1\pi_g)^2$ [87, 88]. 1σ and 2σ molecular orbitals are linear combinations of $1s$ and $2s$ atomic orbitals of oxygen atoms whereas 3σ is obtained by combining $2p_z$ atomic orbitals (z-axis is the molecular axis). π orbitals are combinations of $2p_x$ or of $2p_y$ atomic orbitals. Superscripts are the numbers of electrons occupying the molecular orbitals, whereas + superscript and g and u subscripts refer to molecular spatial symmetry properties [87].

The ground electronic configuration gives the three lower energy molecular states $^3\Sigma_g$, $^1\Delta_g$ and $^1\Sigma_g$ referred also as X, a and b (see Fig. 1.14) [87, 88, 89, 90, 91, 92]. The superscripts are the spin multiplicities, Σ and Δ are the 0 and 2 quantum numbers of the electronic orbital angular momentum, respectively, and the subscripts are related to spatial symmetry properties of the state (g and u mean respectively even or uneven under inversion of spatial coordinates) [87]. According to Hund's rules [88], the lowest energy state is $^3\Sigma_g$ (having the highest spin multiplicity) whereas the first and the second excited states are $^1\Delta_g$ and $^1\Sigma_g$, respectively. Ground vibrational states of $^1\Delta_g$ and $^1\Sigma_g$ are distant from the ground state 1260 and 762 nm, respectively for free molecules [89]. The bond order in the ground state is 2 and the dissociation energy is 494 KJ/mol ($\sim$ 5 eV per molecule), the nuclear interatomic distance is 1.207 Angstrom and the wavenumber of the nuclear vibration is 1580 cm^{-1} [89]. Nuclear interatomic distance in excited states is higher than in the ground one whereas the wavenumber of nuclear vibration has the opposite behavior [89].

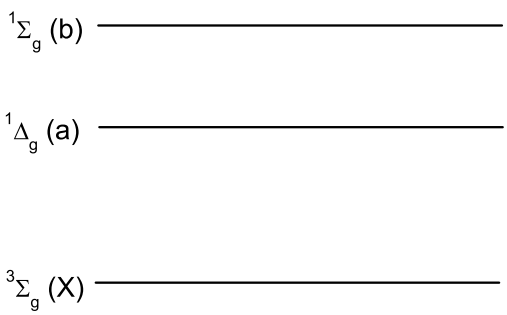

Figure 1.14: The three lower energy states of O_2.

Electric-dipole transitions between any two of the states of the ground electronic configuration are parity forbidden (all the states have the same parity g) [87, 88, 90]. Furthermore, transitions involving the X state are spin forbidden whereas those involving the a one are forbidden due to orbital angular momentum selection rules

[87, 88, 90]. Due to their forbiddeness, radiative lifetimes of the transitions involving the states of ground electronic configuration are long. In particular, under room conditions, $\tau_{b-X} = 11.3$ s, $\tau_{b-a} = 588$ s and $\tau_{a-X} = 72$ min that makes the $a \rightarrow X$ transition probably the most forbidden in nature [93, 94, 90].

Data above reported are relative to quite unperturbed molecules. If molecules are interacting, collisions perturb the electronics states of O_2 lowering the forbiddenness of radiative processes. Studies on the dissolved O_2 shown that the forbiddenness is greatly affected by the polarizability of solvent [95, 96, 97]. Whereas the radiative transitions become partially allowed, so that absorption and emission processes become much more probable, only small variations in the transition energies are observed [90]. In particular, for the $a - X$ transition of O_2 in solution in a great variety of solvents, a maximum spectral shift of about 6 nm with respect to the in air transition was observed against a variation of τ_{a-X} of about seven orders of magnitude [96, 97, 98, 90]. In addition, due to interactions with the solvent, emission and absorption lines broaden and non-radiative deactivation channels, such as electronic to vibration energy transfer, start [90].

When O_2 is dissolved in solids, transitions among states of the ground electronic configuration become partially allowed due to the perturbation by the host matrix [90]. Skuja et al., in Ref. [99], observed the luminescence signal of O_2 by recording the Raman spectrum of O_2 rich silica samples using a Nd:YAG laser source emitting at 1064.1 nm (see Fig. 1.15). Spectra labeled 1, 2 and 3 in Fig. 1.15 feature, in addition to the Raman bands of the active vibrational modes of silica matrix, a strong band at 1535 cm^{-1} Raman shift corresponding to 1272.2 nm absolute wavelength and a weak band at 3072 cm^{-1} Raman shift corresponding to 1584.6 nm absolute wavelength. Due to the spectral position of these two bands and to the wavelength of the laser source, Skuja et al. related these two bands to downward photoluminescence transitions among O_2 molecule states $^1\Delta_g(\nu = 0) \rightarrow^3 \Sigma_g(\nu = 0)$ and $^1\Delta_g(\nu = 0) \rightarrow^3 \Sigma_g(\nu = 1)$ after the upward transition $^3\Sigma_g(\nu = 0) \rightarrow^1 \Delta_g(\nu = 1)$ excited by the Nd:YAG laser source (ν is the vibrational quantum number). In a further investigation, Skuja et al. measured the lifetime of the $^1\Delta_g(\nu = 0) \rightarrow^3 \Sigma_g(\nu = 0)$ transition finding $\tau_{a-X} \sim 0.8$ s [100]. Kajihara et al. [101] investigated the dependence of this lifetime on silanol concentration and fictive temperature [1] of the glass. They found that lifetime decreases from $\tau_{a-X} \sim 0.82$ s down to $\tau_{a-X} \sim 0.69$ s if the silanol concentration is raised from $\sim 10^{17}$ cm^{-3} up to $\sim 10^{20}$ cm^{-3} whereas no dependence on the fictive temperature was found.

[1] The fictive temperature is the temperature at which the glass would be in metastable equilibrium if it were brought instantaneously to this temperature. [102]

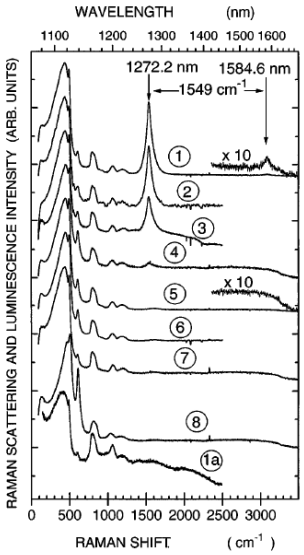

Figure 1.15: Raman spectra of bulk silica. Spectra labeled 1, 2 and 3 are relative to O_2 rich samples and are taken by a Raman spectrometer equipped with a Nd:YAG laser source. Adapted from Ref. [99]

1.5 Diffusion of O_2 in bulk silica

F. J. Norton first measured diffusion coefficient and solubility of O_2 in bulk silica [103]. He measured the permeation rate of molecular oxygen trough the wall of a spherical bulb of silica inside which the O_2 pressure was kept constant. The outside of the bulb was directly connected to a mass spectrometer in order to measure the permeation rate of oxygen by the height of the peak at mass 32. The experiment was carried out by applying a difference of pressure in the range from 300 to 800 mmHg in the temperature range from 950°C to 1080°C. The diffusion coefficient was determined by the time-lag method [104, 105] by measuring the time evolution of O_2 flux during the transient towards the stationary state. O_2 solubility was worked out by measuring the permeation rate at the stationary state. Norton found that the temperature dependence of the diffusion coefficient agrees well with an Arrhenius dependence with a pre-exponential factor $2.7 \cdot 10^{-4}$ cm^2/s ($1.62 \cdot 10^{13}$ nm^2/min) and an activation energy of 113 Kcal/mol (1.18 eV per molecule) [103, 43]. Moreover, the permeation rate was found to increase linearly with pressure demonstrating that oxygen diffuses interstitially without involving either molecular dissociation at the silica surface or significant interactions with the silica matrix.

Diffusion of oxygen and reactivity with silica network was studied also by measuring the profile of isotopically labeled $^{18}O_2$. These works were done mainly on thin silica

films obtained on silicon by thermal oxidation [106, 107, 108, 109]. Experimental data obtained in these systems, and in particular the accumulation of $^{18}O_2$ near the silicon-silica interface, demonstrated that oxygen diffuses as interstitial molecule. Moreover, experiments in which exchange of oxygen atoms between the guest $^{18}O_2$ molecules and the silica network was revealed [110, 111, 107, 108], demonstrated that oxygen diffuses without appreciable "interaction" with the matrix, the average distance between two subsequent exchanges being about 40-80 nm below 1000°C.

Progress in the study of the oxygen diffusion in bulk silica were done by Kajihara et al. [112, 56] that were able to reveal selectively the interstitial O_2 [99, 113]. Using this procedure, they could measure the profile of interstitial O_2 inside silica and determine the diffusion coefficient accurately by fitting the experimental profile with that obtained by solving the Fick's diffusion equation. Kajihara et al. investigated the diffusion in the temperature range from 800°C to 1200°C at pressure lower than 3 bar so extending the range investigated by Norton. Furthermore, they studied the influence of the OH content on diffusion by carrying out experiments on samples with $2 \cdot 10^{18}$ and 10^{20} cm^{-3} OH concentration. Moreover, unlike Norton, they annealed the samples under vacuum before diffusion experiments in order to induce the thermal relaxation of the network. Indeed, if relaxation occurred during the diffusion process, the obtained values of the diffusion coefficient could have been influenced. Kajihara et al. were the first to fit the profile of interstitial O_2 with either the solution of Fick's diffusion equation obtained by supposing that O_2 instantaneously reaches its equilibrium value at the sample surface, or the solution in which an exponential uptake of O_2 on the surface is assumed. They found that the time scale of the absorption of the O_2 in the surface is much shorter than the diffusion one so they neglected the surface absorption time. The agreement between experimental data and the model in which an instantaneous absorption on the surface is assumed, is shown in Fig. 1.16

Diffusion coefficients values found by Kajihara et al. are plotted in the Arrhenius plot of Fig 1.17. These values were estimated by fitting the measured average concentration in the direction of the diffusion as a function of time with the solution of Fick's equation averaged over the sample volume.

Experimental data follow Arrhenius laws (solid lines in Fig. 1.17) whose parameters are summarized in Table 1.1 together with those relative to Arrhenius laws of the solubility shown in Fig. 1.18. The agreement between the values found by Kajihara et al. and those of previous works, also shown in the Figs. 1.17 and 1.18, is good.

Solubility decreases on increasing the temperature and does not follow the Arrhenius law in all the investigated temperature range, being constant above 1000°C independently on the OH content. Kajihara et al. related this behavior to the glass transition. Both, solubility and diffusion coefficient are lower in the sample with higher OH content and the authors impute this effect to the decrease of the number of sites able to

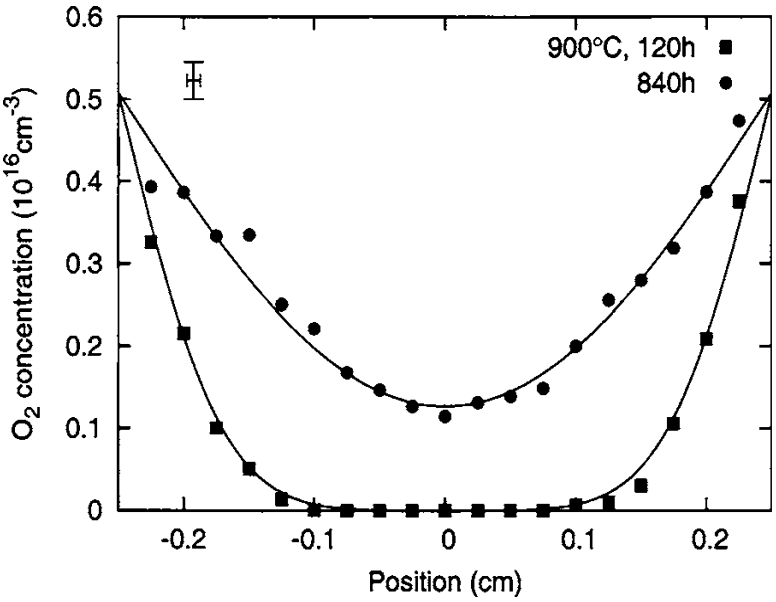

Figure 1.16: Distribution of O_2 concentration inside a bulk silica sample with $2 \cdot 10^{18}$ cm^{-3} OH concentration at two different times (120 h (squares) and 840 h (circles)). Experiments were carried out at 900°C. The lines are the best fit curves obtained by fitting the experimental data with the solution of Fick's diffusion equation supposing the surface absorption to be instantaneous. Adapted from Ref. [56].

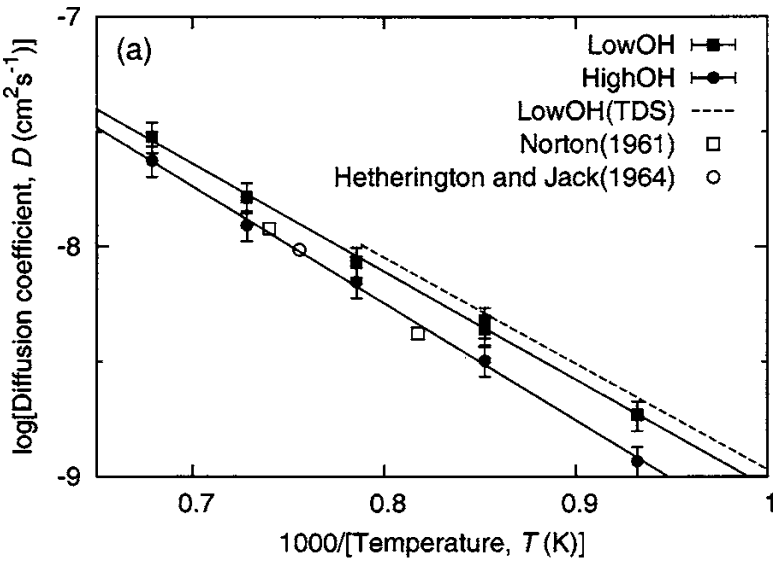

Figure 1.17: Arrhenius plots of O_2 diffusion coefficient in bulk silica determined by Kajihara et al.. Values found in other experimental investigations are also shown. Solid lines are the best fit Arrhenius laws whose parameters are collected in Table 1.1. Data Norton(1961) and Hetherington and Jack (1964) are from Refs. [103] and [114], respectively. Adapted from Ref. [56].

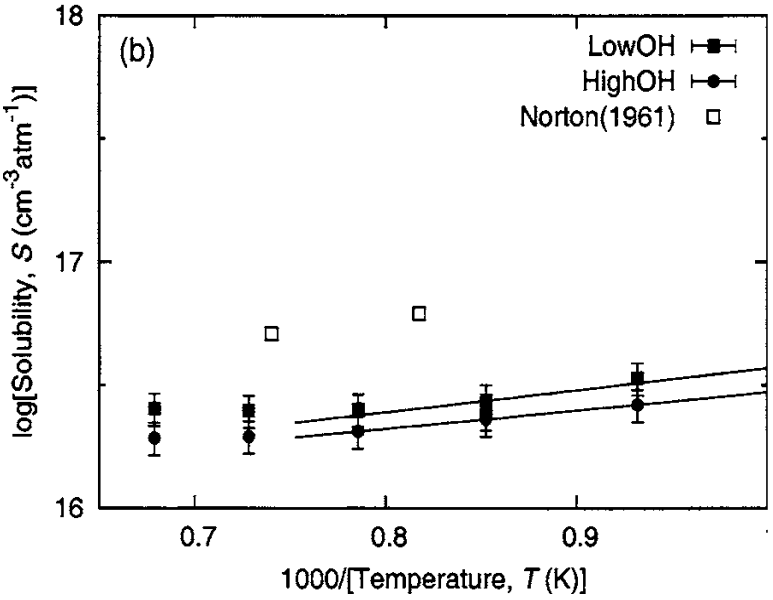

Figure 1.18: Arrhenius plots of O_2 solubility in bulk silica determined by Kajihara et al.. Values found in other experimental investigations are also shown. Solid lines are the best fit Arrhenius laws whose parameters are collected in Table 1.1. Data Norton(1961) are from Ref. [103]. Adapted from Ref. [56].

Table 1.1: Parameters of Arrhenius laws for diffusion coefficient and solubility. D_0 and S_0 are the pre-exponential factors, E_a and $\widetilde{E}_a$ are the activation energies of the diffusion coefficient and solubility, respectively. Adapted from Ref. [56].

OH concentration (cm^{-3})	D_0 (cm^2)/s	E_a (eV)	S_0 (cm^{-3}/atm)	$\widetilde{E}_a$ (eV)
$2 \cdot 10^{18}$	$4.5 \cdot 10^{-5\pm0.2}$	0.93 ± 0.05	$4.8 \cdot 10^{15\pm0.2}$	-0.18 ± 0.03
10^{20}	$6.7 \cdot 10^{-5\pm0.2}$	1.02 ± 0.05	$5.4 \cdot 10^{15\pm0.2}$	-0.15 ± 0.03

accommodate interstitial O_2 due to the presence of OH groups. The equilibrium values of the concentration were found to be proportional to O_2 partial pressure in agreement with Henry's law over the investigated pressure range.

In order to study the interaction between the interstitial O_2 molecules and the silica network, Kajihara et al. investigated the diffusion of $^{18}O_2$ [112]. During the diffusion process, $^{18}O_2$ molecules exchange O atoms with the silica network becoming $^{18}O^{16}O$ or $^{16}O_2$ interstitial molecules. These three types of molecules can be selectively revealed due to the isotopic shift of the vibrational side band of the photoluminescence transition used to reveal interstitial oxygen. Authors measured the time variations of these three oxygen species and fitted the experimental data with the diffusion equation corrected to take into account the possible exchange of one O atom between interstitial molecules

and the network. Experiments were carried out from 500°C to 900°C in two samples with different OH contents and in a fluorine-doped samples. Authors found that the exchange rate increases on increasing the temperature following an Arrhenius law with activation energy of about 2 eV. Moreover, they found that the exchange-free diffusion length increases on decreasing the temperature varying from about 1 μm at 900°C up to 100 μm at 500°C. The above findings are almost independent on the presence of impurities (fluorine and OH groups) suggesting that they are not preferential sites for exchange reactions.

1.6 Silica nanoparticles

A nanoparticle is a body whose size is less than few tens of nanometer in all three dimensions. Some physical properties are size-independent for a macroscopic body whereas a dependence on size is observed when one or more of its dimensions fall into nanoscale. Both simulative and experimental works evidenced that many physical properties of silica nanoparticles are size dependent [17, 18, 19, 20, 21, 22, 23, 24]. In particular, simulative works [19, 20] on spherical silica nanoparticles having diameter ranging from 1.8 to 5 nm predicted a radial density distribution, as shown in Fig. 1.19 for two representative cases.

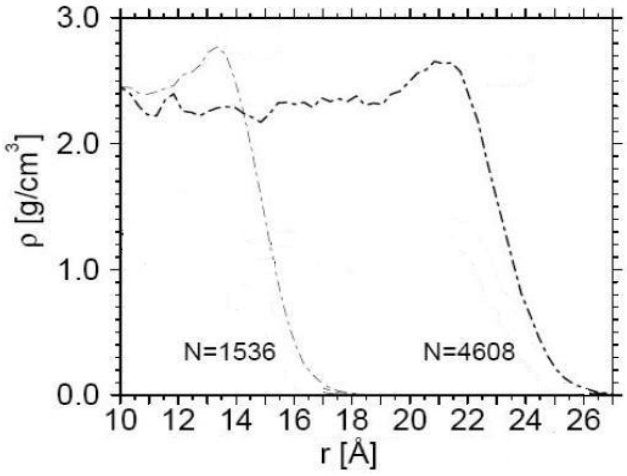

Figure 1.19: Theoretical radial density profile in spherical silica nanoparticles containing 1536 atoms (radius ∼3 nm) and 4608 atoms (radius ∼5nm). Adapted from Ref. [19].

Density is almost constant in the inner part of nanoparticles and shows a peak near the surface. The peak extends over a region of about 0.6 nm independently on the nanoparticle size. This outer region is named surface shell, whereas the inner part of the particle is named core region. Density profile shown in Fig. 1.19 evidences that

the average density depends on the particle size. In particular, the model predicts an increase of the average density on decreasing the size due to the greater ratio between the surface shell volume and the core region one for the smaller particles.

Besides density, the ring distribution in nanoparticles is different from that in the bulk materials. Indeed, the former is shifted towards smaller rings [19, 20]. Furthermore, simulative works predicted a ring distribution in the shell surface different from that of the core region [19, 20]. In particular, the ring distribution in the core region is equal to that of bulk silica (having the maximum at 6-membered ring) whereas the distribution in the surface shell has the maximum corresponding to 5-membered rings. These features suggest that the mean value of the Si-O-Si angle in the surface shell is smaller than in the core region so its average value is smaller in silica nanoparticles with respect to bulk silica.

Experimental works confirmed the size dependence of the physical properties of silica nanoparticles [115, 22, 23, 24]. Fig. 1.20 shows the Raman spectra of silica nanoparticles produced by the pyrogenic technique, fumed silica, with diameter ranging from 7 to 40 mn [22]. A typical Raman spectrum of bulk silica is reported for comparison [22].

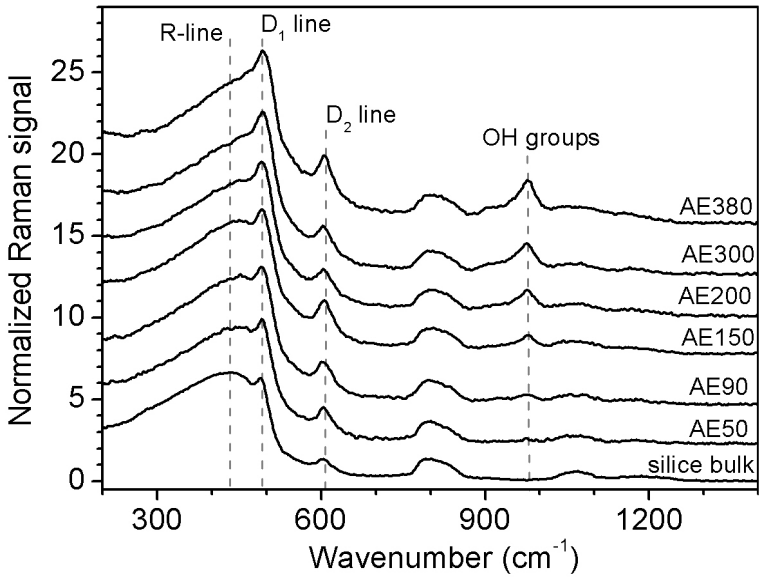

Figure 1.20: Raman spectra of spherical silica nanoparticles. Numbers of the labels of the spectra are values of the specific surface in m^2/g. Radii of particles are in the range from 3.5 nm (AE380) up to 20 nm (AE50). A Raman spectrum of bulk silica is also reported for comparison. Adapted from Ref. [22].

The R-line is shifted towards higher wavenumber and the amplitude of the D1 and D2 lines is higher in nanoparticles with respect to bulk silica. Moreover the Raman shift of R-line and the amplitude of D1 and D2 lines increase on decreasing particles size. These features were demonstrated to be in agreement with the core-shell structure predicted by simulative works. In particular, the spectrum can be obtained as a combination of the spectrum of the core region, having physical properties similar to that of bulk silica, and that of the surface shell having a density about 10% higher than the core and a thickness of about 1 nm independently on particles size [116]. Raman spectra of silica nanoparticles also show a band peaked at 980 cm^{-1} related to the Si-OH stretching vibration that is not visible in the bulk silica [117, 118].

OH groups on silica surface have an important role in the physical adsorption of small molecules and in chemical reactions on the surface [119, 120]. In details, OH surface groups can be classified as isolated (free), vicinal and geminal (see fig. 1.21).

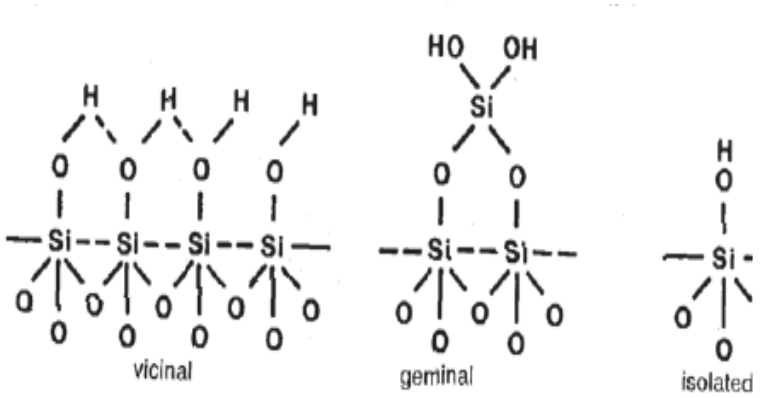

Figure 1.21: OH species on silica surface. Adapted from Ref. [119].

Isolated OH groups do not interact each other because their average distance is more than 0.3 nm [121]. Vicinal groups are formed by two OH groups linked to silicon atoms belonging to neighboring tetrahedra whereas geminal OH groups are constituted by groups linked to the same silicon atom [122, 119]. Experimental data relative to a lot of silica materials with specific surface ranging from few m^2/g to 900 m^2/g evidenced that surface density of OH groups is almost independent on the specific surface value [123]. Fig. 1.22 shows the dependence of the area of the band at 980 cm^{-1} (that is proportional to the OH concentration per mass unit) on the specific surface in commercial fumed

silica nanoparticles [124]. The linear dependence suggests that the greater contribution to OH density in these silica nanoparticles is from surface OH groups in agreement with a constant surface concentration independently on the specific surface.

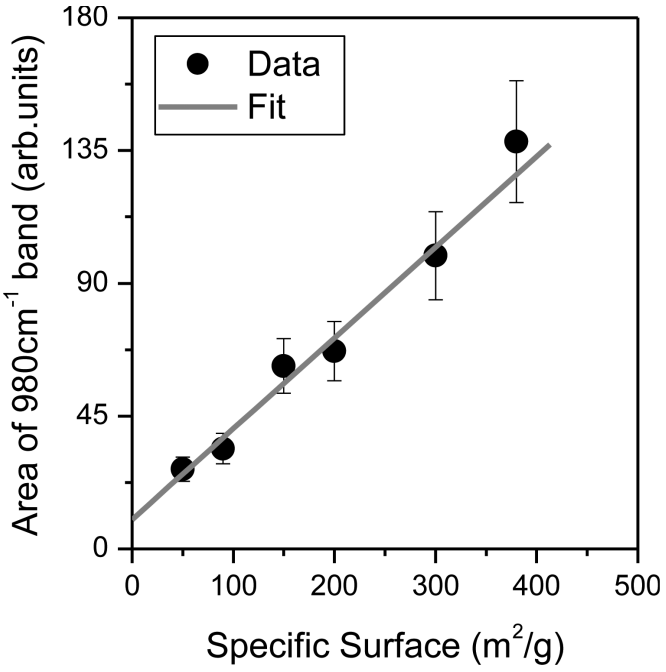

Figure 1.22: Dependence of the area of the Raman band at 980 cm^{-1} on specific surface in silica nanoparticles. Adapted from Ref. [124].

OH surface coverage makes silica nanoparticles hydrophilic so in ambient atmosphere there are one or more layers of water deposited on their surface. The water content is related to the specific surface and can be as high as 7% in a sample with specific surface of 900 m^2/g [119, 125].

1.6.1 Effects of thermal treatments of silica nanoparticles

Thermal treatments change Raman spectra of silica nanoparticles, their OH content, water coverage of their surface and nanoparticles morphology [115, 126, 22, 127, 128, 119]. Thermal treatments first remove the water surface coverage and then let two OH groups react to form a ring and a water molecule. The reaction of vicinal silanol groups to form 4-membered or larger rings starts at about 170°C whereas that in which 3-membered rings are formed require temperature higher than 300°C due to the higher value of formation energy of smaller rings. Reactions giving two membered rings are possible if the temperature is higher than 500°C and the sample is kept under vacuum [119]. Since thermal treatments change the ring distribution, their effects can be studied by Raman spectroscopy. An experimental investigation in the temperature

range from 100°C to 1000°C on fumed silica whose average particles diameter ranged from 7 to 40 nm reveals that the D2 line amplitude as well as the position of the R-line are affected by thermal treatments [22, 23]. Effects of isochronal (2 h) thermal treatments in ambient atmosphere are shown in Figs. 1.23 and 1.24

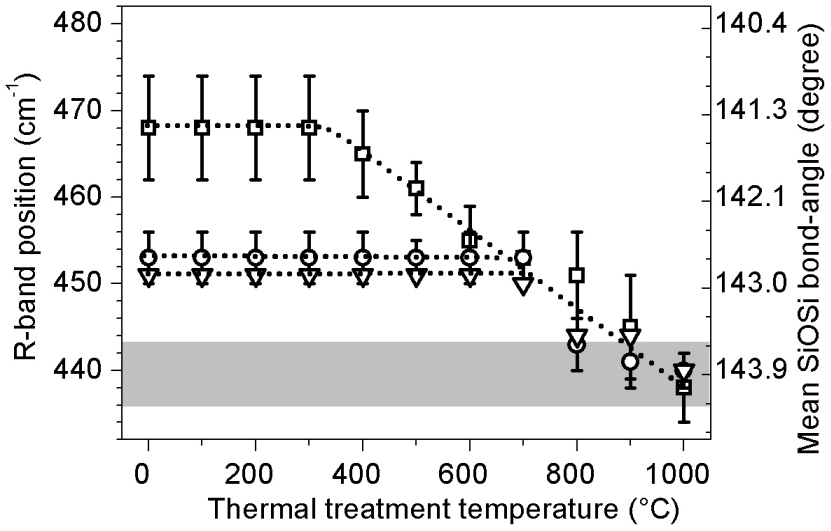

Figure 1.23: Dependence of the position of Raman R-line and mean Si-O-Si bond angle on treatment temperature in silica nanoparticles of average radius 3.5 nm (squares), 7 nm (circles) and 20 nm (triangles). Each treatment was done for 2h. Adapted from Ref. [22].

The position of the R-line is not modified at low temperature whereas it is shifted towards lower wavenumbers if the temperature is high enough. The shift is higher for higher temperature and starts at lower temperature in smaller nanoparticles. The position of the R-line is the same as in the bulk silica if the temperature is higher than 900°C independently on the particles size. The amplitude of the Raman D2 line, first increases on increasing the treatment temperature then decreases. This behavior can be explained in the frame of the core-shell model. In particular, the shift of the R-line was related to the relaxation of strains in the core region whereas the increase of the D2 amplitude was related to the formation of 3-membered rings due to dehydration of the surface. The successive decrease of the D2 amplitude was connected to the sintering process between nanoparticles that destroys small rings to form greater ones extending on two adjacent particles [22, 127].

1.6.2 O_2 in silica nanoparticles

Properties of O_2 molecules in silica nanoparticles were investigated in Ref. [15]. In particular, Raman spectra of fumed silica nanoparticles of diameter 40 nm and 7 nm

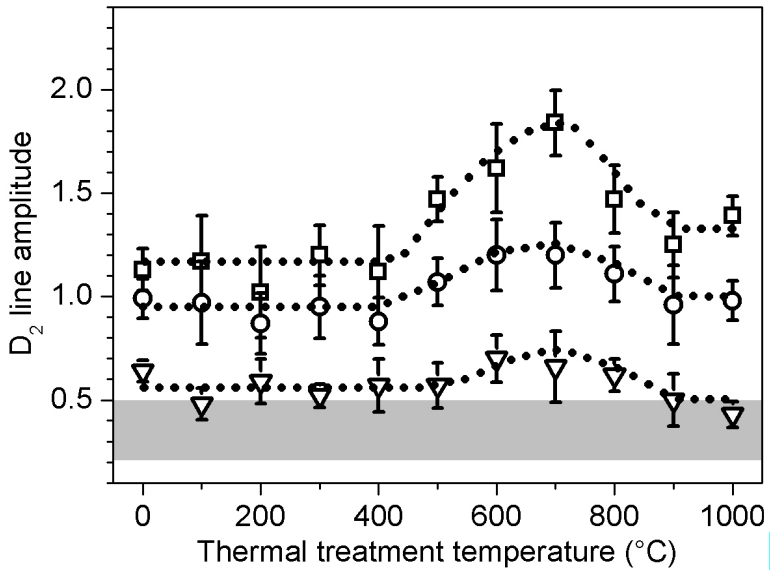

Figure 1.24: Dependence of the amplitude of the D2 Raman line on treatment temperature in silica nanoparticles of radius 3.5 nm (squares), 7 nm (circles) and 20 nm (triangles). Each treatment was done for 2h. Adapted from Ref. [22].

were taken before and after a thermal annealing in different atmospheres at 200°C. Fig. 1.25 shows Raman spectra of the two as-grown samples and those after thermal annealing. The spectra were recorded by means of a Raman spectrometer having a laser source at 1064 nm, so the luminescence band of interstitial O_2 can be revealed in addition to Raman bands of silica, as already explained. The luminescence band of interstitial O_2 is present in the as-grown material and increases after the annealing in O_2 atmosphere in both samples whereas decreases in the 40 nm diameter sample and does not change in the 7 nm one if the annealing is performed in air or He atmosphere. The rise of the O_2 PL was related to the increase of interstitial O_2 content due to diffusion of molecules from the atmosphere into nanoparticles during the thermal annealing. In Fig. 1.25 it can also be seen that the PL amplitude of interstitial O_2 in the 40 nm diameter sample is higher than in the 7 nm one either in the as-grown samples or in the annealed ones.

Furthermore, the optical properties of O_2 trapped in silica nanoparticles were investigated by means of time resolved emission spectroscopy on the two samples annealed in O_2 atmosphere. In particular, the lifetime of the $^1\Delta_g \rightarrow ^3\Sigma_g$ transition under excitation at 765 nm ($^3\Sigma_g \rightarrow ^1\Sigma_g$) was measured at room temperature. Values of (0.46 ± 0.01) s and ~ 0.3 s were found for 40 nm and 7 nm diameter samples, respectively. The measured lifetimes are shorter than in bulk silica and the authors related this difference to the higher content of OH groups in silica nanoparticles with respect to bulk silica.

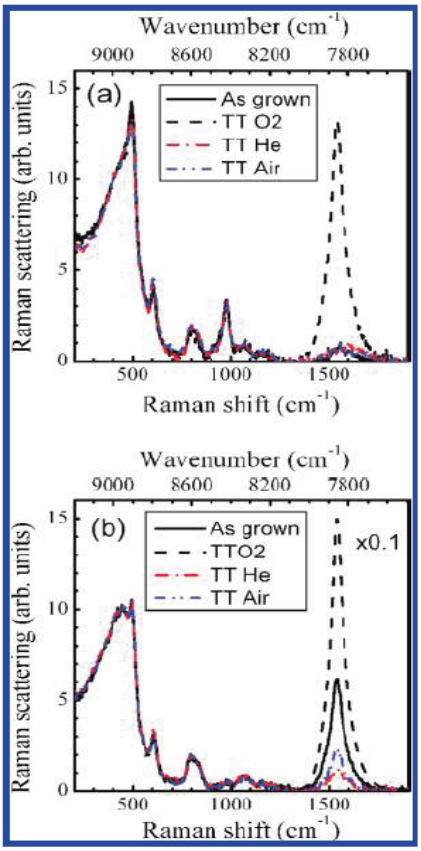

Figure 1.25: Raman spectra of as-grown silica nanoparticles and after thermal annealing in O_2 (50 bar), in air, or in He (50 bar) atmosphere at 200°C. Spectra were taken by a Nd:YAG laser source at 1064 nm. Spectra in the panel (a) are relative to the 7 nm diameter sample, whereas those of 20 nm diameter sample are in the panel (b). Adapted from Ref. [15].

Furthermore, the authors used the factor found in Ref. [129] in bulk silica to obtain the O_2 concentration from the amplitude of the luminescence band in Raman spectra by taking into account the different O_2 lifetimes in nanoparticles. In particular, they found that O_2 concentrations in the spectra shown in Fig. 1.25 after thermal annealing in O_2 are $(1.8 \pm 0.2)^{18}$ cm^{-3} and $(1.5 \pm 0.2)^{19}$ cm^{-3} for the 7 and 40 nm diameter samples, respectively.

Chapter 2

Materials and methods

2.1 Materials

Diffusion process of O_2 in silica nanoparticles was investigated in this work on materials differing in synthesis methods, size, morphology and surface chemistry. In particular, experiments were carried out on silica nanoparticles either produced by pyrogenic techniques and by microemulsion methods. Apart form other features, detailed in the following paragraphs, these materials differ because they are of commercial and experimental origin, respectively.

2.1.1 Commercial nanoparticles

Pyrogenic nanoparticles were fumed silica produced mainly by Evonik industries AG. Fumed silica is a powder of spherical nanoparticles obtained by oxidation of silicon tetrachloride ($SiCl_4$) in O_2/H_2 flame at temperature of about 1000°C [130, 131]. In particular, $SiCl_4$ reacts with H_2O molecules, produced in the oxyhydrogen flame, to obtain SiO_2 and HCl as described in eq. 2.1 [130, 131]

$$SiCl_4 + 2H_2O \rightarrow SiO_2 + 4HCl \tag{2.1}$$

The obtained powder contains primary particles, agglomerates and aggregates of primary particles. Agglomerates are formed by two or more primary particles linked by the interaction between silanol surface groups whereas an aggregate is a group of primary particles partially fused due to their impact in the combustion chamber [130, 131]. Features of obtained particles such as average size of primary particles and its distribution, surface morphology and specific surface depend on the concentrations of co-reactants and on permanence time of particles in the combustion chamber so materials having very different characteristics can be obtained by changing these production parameters. In addition, some properties of as-grown particles can be changed by means of after-synthesis treatments. For instance, the hydrophilicity of fumed silica, related to the

presence of silanol groups on the nanoparticles surface, can be suppressed by chemical substitution of surface silanol groups with hydrophobic ones.

Evonik fumed silica have a purity larger than 99.8% by weight and the physicochemical properties of the investigated types are summarized in Table 2.1. Average diameter was determined by TEM (Transmission Electrons Microscopy) measurements whereas specific surface value was measured by BET (Brunauer−Emmett−Teller) method. Typical size distributions are reported in Fig.2.1. Aerosil380 and Aerosil300 have the same average diameter but different specific surface due to different surface morphology. AerosilR816 is obtained by making hydrophobic Aerosil200.

Table 2.1: Physicochemical properties of investigated fumed silica types [130, 131].

Commercial name	Nickname	Average diameter (nm)	Specific surface m^2/g	
Aerosil380	AE380	7	380	hydrophilic
Aerosil300	AE300	7	300	hydrophilic
Aerosil200	AE200	12	200	hydrophilic
Aerosil150	AE150	14	150	hydrophilic
Aerosil90	AE90	20	90	hydrophilic
AerosilOX50	AE50	40	50	hydrophilic
AerosilR816	R816	12	200	hydrophobic

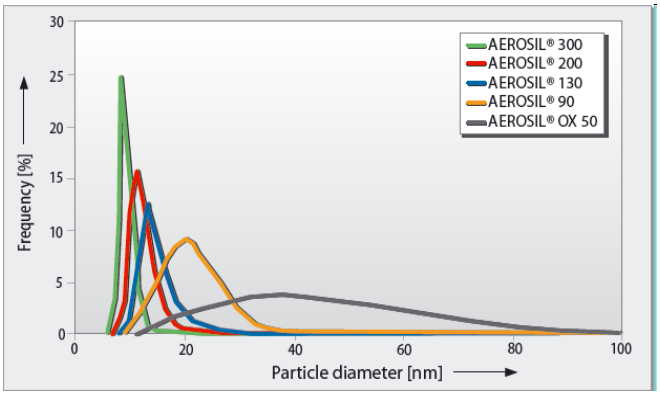

Figure 2.1: Size distribution of fumed silica nanoparticles. [130, 131]

In addition to the above samples, silica nanoparticles distributed by Sigma Aldrich were investigated (see appendix A). Physicochemical properties of these samples are summarized in Table 2.2.

Table 2.2: Physicochemical properties of the Sigma Aldrich samples [132].

Sigma Aldrich code	Nickname	Average diameter (nm)	Specific surface m^2/g
S5130	Sig395	7	395
718483	Sig200-12	12	200
S5505	Sig200		200

2.1.2 Laboratory nanoparticles

Microemulsion samples were produced and characterized from a morphological point of view at IIT (Istituto Italiano di Tecnologia) Center for Bio-Molecular Nanotechnologies@Unile. Microemulsion method is a technique to obtain silica by ammonium-catalyzed hydrolysis-condensation reactions of tetraethylorthosilicate (TEOS) [133]. A microemulsion is an isotropic and thermodynamically stable solution of two immiscible liquids and a surfactant that stabilizes the solution [134]. In particular, the microemulsion is formed by domains (droplets) of one of the two liquids, covered by a monolayer of surfactant, dispersed in the continuous phase of the other liquid [135, 136]. In the microemulsion method, the synthesis of materials takes place inside the droplets of one liquid and the relative concentrations of reactants and surfactants as well as their nature affects the morphological features of the obtained material [137].

The investigated nanoparticles (whose physicochemical features are summarized in Table 2.3) were obtained either by a ternary microemulsion (a mixture of TEOS, water and surfactant (Triton X-100)) or by a quaternary microemulsion (in which a co-surfactant was added to further stabilize the microemulsion) [138]. In particular, nanoparticles having size 25 nm were obtained by ternary microemulsion whereas bigger ones were sinthesized by using a quaternary microemulsion. Independently on the microemulsion composition, reactions were catalyzed by ammonium hydroxide (NH_4OH). The surface of particles so produced are decorated by silanol groups. Amine modified nanoparticles having NH_2 groups on their surface were obtained by post-synthesis reaction of surface silanol groups with aminopropyltriethoxysilane (APTES). Details of these procedures are reported in Ref. [138].

2.2 Luminescence spectroscopy

A molecule in its electronic excited state can decay toward a lower energy state through radiative and non-radiadive processes [87]. In a radiative process, the molecule decays by emitting a photon of energy equal to the difference between the energy of initial and final levels whereas in non-radiative processes it transfers its energy to other bodies such as other molecules or to the host matrix in which it is located, by exciting phonon modes [87]. Typical non radiative decay times are of the order of 10^{-12} s

Table 2.3: Physicochemical properties of the investigated microemulsion nanoparticles [138].

Nickname	Average diameter (nm)	Surface group
25nm	25	OH
25nmNH_2	25	NH_2
60nm	60	OH
60nmNH_2	60	NH_2
120nm	120	OH
120nmNH_2	120	NH_2

whereas in the case of radiative processes the decay times are of the order of 10^{-9} s if the electronic transition is allowed (photoluminescence) but could be several orders of magnitude greater if it is forbidden (phosphorescence). In general, both types of processes, radiative and non-radiative, may contribute to the de-excitation of a molecule as shown in Fig. 2.2. The molecule, initially in its ground state, goes to an excited electronic state after absorbing a photon. Next, if temperature is supposed to be 0 K, the molecule goes to the lowest energy vibrational state of the excited electronic state by non-radiative processes, then it goes to a vibrational excited state of the electronic ground state emitting a photon and finally reaches the ground state by non-radiative relaxation. The probability per unit time that one of the spontaneous radiative decay processes shown in Fig. 2.2 occurs within the electric dipole approximation is given by [88]

$$P(m', n' = 0; m, n) = \frac{16\pi^3\nu^3}{3c^3h\varepsilon_0}|\langle\psi_{m',0}|\mu|\psi_{m,n}\rangle|^2 \tag{2.2}$$

where $P(m', n' = 0; m, n)$ is the probability per unit time of the transition from the vibrational ground state of the excited electronic level to the n^{th} vibrational level of the electronic ground state, ν is the frequency of the photon whose energy is resonant with the transition, h is the Planck constant, ε_0 the vacuum permittivity, $|\psi_{m',0}\rangle$ and $|\psi_{m,n}\rangle$ the wave functions of the states involved in the transition and μ the electric dipole operator. Selection rules indicate if the probability to have a transition between two molecular states is different from zero. In order to have a non-zero probability, the matrix element of dipole electric operator between initial and final states have to be different from zero. For what concerns the spin quantum number, the transition is allowed if and only if the two states involved in the transition have the same spin multiplicity whereas, for what concerns the orbital selection rules, they involve an integral on spatial coordinates so the symmetry of the molecule has to be taken into account. The intensity of the radiation emitted at frequency ν_{em} under excitation at

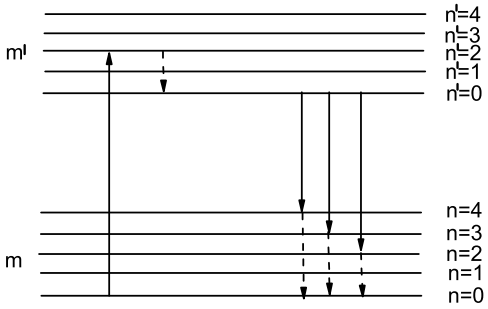

Figure 2.2: Radiative and non-radiative decays of a molecule from an excited electronic state. Upward solid arrow represents the absorption of a photon whereas downward solid and dashed arrows represent radiative and non radiative decays, respectively. m and m' are the sets of quantum numbers describing the electronics state whereas n and n' are the vibrational quantum numbers.

frequency ν_{exc} is given by the following relationship [139]

$$I(\nu_{em}, \nu_{exc}) = \Phi I_0 (1 - e^{-C\alpha(\nu_{exc})l}) \tag{2.3}$$

where l is the optical path of the exciting radiation inside the medium, C the molecules concentration, $\alpha(\nu_{exc})$ the molar extinction coefficient that is related to the probability that the absorption transition occurs and Φ is the quantum yield defined as the ratio between the number of absorbed and emitted photons [140]. If $C\alpha(\nu_{exc})l \ll 1$, that is under low absorption condition, eq. 2.3 can be written as

$$I(\nu_{em}, \nu_{exc}) = k_r \tau I_0 C \alpha(\nu_{exc}) l \tag{2.4}$$

where the expression $\Phi = k_r \tau$ has been used for the quantum yield (k_r is the radiative decay constant and $\tau = \frac{1}{k_r + k_{nr}}$ is the lifetime of the transition, k_{nr} being the non-radiative decay constant).

2.3 Raman spectroscopy

Raman scattering is a process of interaction between light and matter in which photons are inelastically scattered by matter. The phenomenon of Raman scattering can be illustrated by the following classical model [141] in which the simple case of a system consisting of a diatomic molecule is considered by supposing that its vibration (variation of the internuclear distance) can be assumed harmonic at frequency ν. In this approximation, the deviation of the internuclear distance (q) from its equilibrium value changes according to eq. 2.5

$$q(t) = q_0 \cos 2\pi\nu t \tag{2.5}$$

where q_0 is the amplitude around equilibrium internuclear distance and t the time. Suppose that an electromagnetic plane wave, whose electric field at the molecule position follows the eq. 2.6, where E_0 and ν_r are the amplitude and the frequency, respectively, impinges on the molecule:

$$E(t) = E_0 \cos 2\pi\nu_r t. \tag{2.6}$$

The electric field induces in the molecule the dipole moment

$$P(t) = p(q)E(t) \tag{2.7}$$

where $p(q)$ is the polarizability of the molecule. In the case of small changes in the polarizability, this latter can be expanded in a power series stopping to first order, as shown in eq. 2.8

$$p(q) = p_0 + \frac{\partial p}{\partial q}_0 q \tag{2.8}$$

where p_0 and $\frac{\partial p}{\partial q}_0$ are the polarizability and its first derivative with respect to the departure from equilibrium internuclear distance calculated at the equilibrium internuclear distance (q=0). By combining eqs. from 2.5 to 2.8, the following expression for the dipole moment as a function of time is obtained

$$P(t) = p_0 E_0 \cos 2\pi\nu_r t + \frac{1}{2}\frac{\partial p}{\partial q}_0 q_0 E_0[\cos 2\pi(\nu_r - \nu)t + \cos 2\pi(\nu_r + \nu)t] \tag{2.9}$$

According to eq. 2.9, the time dependence of the induced dipole moment can be written as the sum of three oscillating contributions that, from a classical point of view, are related to radiation emission at frequencies ν_r (Rayleigh scattering, elastic), $\nu_r - \nu$ and $\nu_r + \nu$ (Raman scattering, inelastic).

From a quantum mechanical point of view, Raman scattering is a second order process in which the system composed by the molecule and the electromagnetic field goes from the initial state to the final one via an intermediate state whose energy is different from the initial one and therefore is a virtual state [142] (see Fig. 2.3). In the case in which the radiation is scattered at frequency $\nu_r - \nu$, said Stokes scattering, a photon of energy $h\nu_r$ is absorbed and one having energy $h\nu_r - h\nu$ is emitted whereas the molecule goes from the vibrational state having energy $nh\nu$ to that of energy $(n+1)h\nu$ (n is an integer and h the Planck constant). On the contrary, in the anti-Stokes scattering, a photon of energy $h\nu_r$ is absorbed and one having energy $h\nu_r + h\nu$ is emitted whereas the molecule goes from the vibrational state having energy $nh\nu$ to that of energy $(n-1)h\nu$. Since in thermal equilibrium conditions the populations

of the lower energy levels are higher, Stokes lines are more intense than anti-Stokes ones [141]. In the harmonic approximation, only the transitions in which n changes of one unit are allowed by quantum selection rules in the case of diatomic molecules, whereas for polyatomic molecules a coordinates transformation has to be done to reduce the many-body problem to many one-dimensional harmonic oscillators problems and the symmetry of each normal mode must be taken into account in order to determine if the transition is allowed [89].

Due to the used laser source in this work (Nd:YAG), both silica Raman bands and the luminescence band of interstitial O_2 are present in the Raman spectra (see sec. 1.4) so in the following they will be referred to Raman/PL spectra. All reported Raman/PL spectra were taken at 500 mW laser power using 5 or 15 cm^{-1} spectral resolution if structural changes in the network had to be investigated or if only the mass of interstitial O_2 had to be determined, respectively.

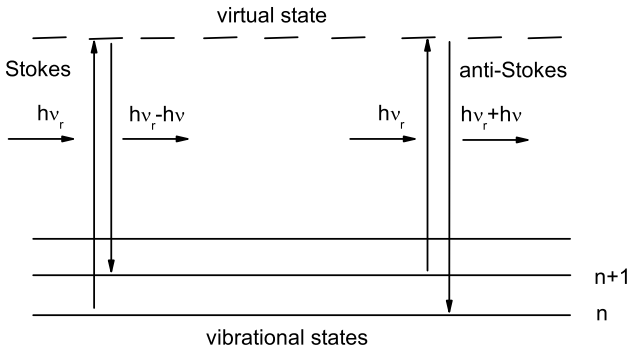

Figure 2.3: Schematic representation of Stokes and anti-Stokes Raman scattering processes among electron-vibrational states of a molecule.

Raman spectra were taken by a FT-Raman spectrometer RAMII Bruker whose schematic representation is depicted in Fig. 2.4. L is the laser source, a Nd:YAG laser ($\lambda = 1064$ nm) of maximum power 500 mW. The laser radiation sent to the mirror M_1 is reflected on the A lens that focuses the beam on the sample S by means of the mirror M_2. The radiation scattered by the sample is collected by the lens B. The distance between the sample and the lens B can be changed by steps of 50 μm for a total range of 1 cm in order to maximize the intensity of the collected scattered radiation. After being collected by the lens B, the radiation is reflected by the mirror M_3 on the lens C that focuses it on the filter F, a notch filter, whose function is to remove the scattered radiation having wavelength about equal to the source one (Rayleigh scattering). Then the radiation reaches the Michelson interferometer I whose schematic picture is shown in Fig. 2.5. The radiation incoming in the interferometer is separated in two beams by the beam splitter E. One of the beams moves toward the mirror M_4 placed at fixed

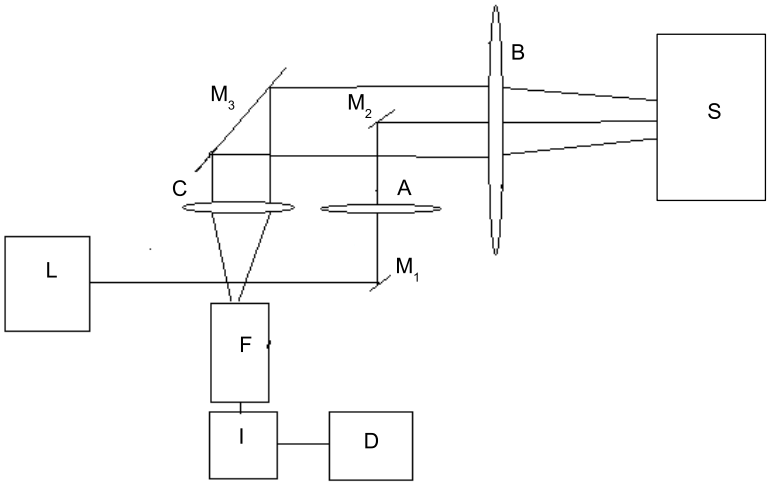

Figure 2.4: Schematic representation of the FT-Raman spectrometer RAMII Bruker. (L) is the laser source, (A), (B) and (C) are lenses, (M_1), (M_2) and (M_3) are mirrors, (S) is the sample, (F) the notch filter, (I) the Michelson interferometer and (D) the detector.

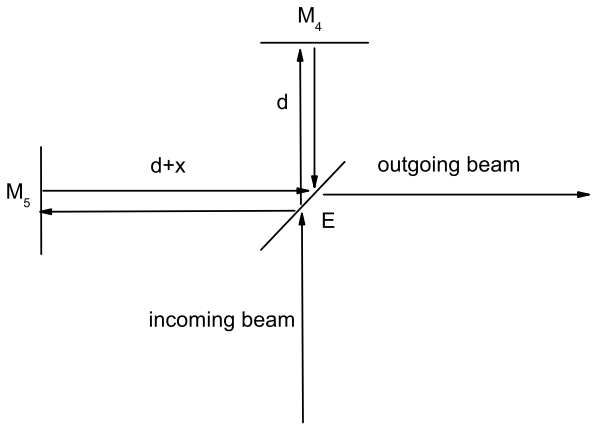

Figure 2.5: Schematic representation of the Michelson interferometer (part I in the scheme of Fig. 2.4). E is the beam splitter, M_4 and M_5 are the fixed and movable mirrors, respectively.

distance d from the beam splitter, whereas the other one moves toward the movable mirror M_5 whose distance from the beam splitter is $d + x$. After being reflected by mirrors, the two beams are superimposed and reach the detector D (see Fig. 2.4). Since the variation of x changes the phase difference between the two beams, the intensity of the outgoing beam is a function of x. The detector samples the beam intensity as a function of x and the spectral distribution of scattered radiation is determined by making the fourier transform of the revealed signal. Indeed, if there is no phase relation among the spectral components of the detected signal, its intensity as a function of x is given by eq. 2.10

$$I(x) = \int_0^\infty \frac{1}{2}\overline{I}(\overline{\nu}')[1 + \cos(2\pi\overline{\nu}'x)]d\overline{\nu}' \tag{2.10}$$

where $I(x)$ is the signal revealed when the mirror (M_5) is $d + x$ away from the beam splitter and $\overline{I}(\overline{\nu}')$ is the spectral density of the signal $\overline{\nu}'$ being its wavenumber, the reciprocal of wavelength. Eq. 2.10 can be put in the form given by eq. 2.11 where $I(0) = \int_0^\infty \overline{I}(\overline{\nu}')d\overline{\nu}'$.

$$2I(x) - I(0) = \int_0^\infty \overline{I}(\overline{\nu}')\cos(2\pi\overline{\nu}'x)d\overline{\nu}' \tag{2.11}$$

By making the Fourier transform of both sides of eq.2.11, eq. 2.12 is obtained

$$\int_{-\infty}^{+\infty}[2I(x) - I(0)]e^{-i2\pi\overline{\nu}x}dx = \int_{-\infty}^{+\infty}[\int_0^\infty \overline{I}(\overline{\nu}')\cos(2\pi\overline{\nu}'x)d\overline{\nu}']e^{-i2\pi\overline{\nu}x}dx \tag{2.12}$$

By chancing the order of the integrals in the right hand side of eq. 2.12 and integrating over x variable, eq. 2.13 is obtained

$$\int_{-\infty}^{+\infty}[2I(x) - I(0)]e^{-i2\pi\overline{\nu}x}dx = \int_0^\infty \frac{1}{2}\overline{I}(\overline{\nu}')[\delta(\overline{\nu}' - \overline{\nu}) - \delta(\overline{\nu}' + \overline{\nu})]d\overline{\nu}' \tag{2.13}$$

Finally, integrating the right side of eq. 2.13, the relation between the spectral density of the scattered radiation and the intensity of the revealed signal as a function of x is obtained

$$\overline{I}(\overline{\nu}) = 2\int_{-\infty}^{+\infty}[2I(x) - I(0)]e^{-i2\pi\overline{\nu}x}dx \tag{2.14}$$

According to eq. 2.14, the spectral density of the scattered radiation is the Fourier transform of $2[2I(x) - I(0)]$.

Raman spectra shown in the following are relative to the Stokes part of the spectrum and the spectral density is reported as a function of the Raman shift, that is the difference between the wavenumber of the laser source and the one of the scattered light.

2.4 Thermal treatments

O_2 diffusion in silica nanoparticles was investigated by thermally treating samples either in air or in O_2. Experiments were carried out on tablets of volume 4x4x2 mm^3, obtained by pressing the starting powder in an uniaxial press at pressure of about 0.3 GPa. This procedure allows us to have handleable samples without losing nanometer features of the material. Indeed, only points of contact among nanoparticles are established as a consequence of the applied pressure [127]. It is worth noting that the tablets are porous and the dimension of pores is about equal to that of constituent nanoparticles so the diffusion of O_2 inside the tablet, that is through the interstices among nanoparticles, does not limit the diffusion process into the nanoparticles that is the process to be investigated.

In order to determine diffusion coefficient, either sorption or desorption experiments were carried out. Sorption experiments were performed in O_2 atmosphere whereas the desorption ones were performed in air. Both types of experiments were made by using the experimental set-up sketched in Fig. 2.6. It is constituted by a O_2 bomb, A, two pressure gauges, B and C, a vacuum pump, E, a stainless steel blind pipe, F, and a furnace, G.

In desorption experiments, the sample is put in the stainless steel pipe F held at the treatment temperature within 1°C by the furnace G. At the end of treatment, the pipe is immersed in water at room temperature to cool quickly the sample ($\sim$1 min) and a Raman/PL spectrum of the sample is taken to determine the content of interstitial O_2 as will be described in the next two sections.

In sorption experiments, the tablet is preliminary thermally treated in air for 5 min at 300°C in a furnace (not drawn in figure) in order to desorb O_2 present in the as-received material. Successively the sample is inserted in the pre-heated stainless steel blind pipe F, the air is removed by the vacuum pump E in about 2 min. This time interval is sufficient for the sample to reach the thermal treatment temperature and for the pressure to be lowered to about 10^{-4} mbar. Then the valve D is closed and the system is filled with O_2 gas. At the end of the treatment, the pipe is cooled in water, then O_2 is removed trough the valve D.

The above described thermal treatments were performed on different tablets by increasing the duration until the diffusive equilibrium state is reached, that is when no variation in O_2 content is revealed after increasing the treatment time. It is worth noting that a different tablet was used for each thermal treatment time in order to minimize the effects of the heating times in which desorption of O_2 would take place.

Diffusion experiments on Evonik and Sigma Aldrich materials were carried out by the experimental set-up of Fig. 2.6 whereas microemulsion materials were thermally treated in a Parr reactor, schematically shown in Fig. 2.7. The reason is that the synthesized quantity of material is insufficient to obtain a standard tablet so the powder

was manually pressed in the hollow, about 2 mm diameter and 1 mm deep, of a stainless steel cylinder and this form is not suitable to be treated in the above described experimental set-up. The reactor (see Fig. 2.7) consists of a stainless steel cylindrical vessel A having an internal volume of 240 ml in which samples are accommodated during the treatment in controlled atmosphere. The vessel is closed by a stainless steel cover B in which two valves are placed (I and O) for the loading and unloading of used gas before and after the thermal treatment. The cover is attached to the vessel by means of two steel half-rings H with bolts that are tightened with a torque depending on the work pressure of the reactor. A graphite seal F is placed between the cover and the vessel in order to increase the sealing of the system. Finally, to balance the radial thrust, the vessel locked by the half rings is secured by a circular steel ring G. Temperature is measured by a thermocouple inserted inside the well C to be in thermal contact with the bottom of the well. Pressure is measured by a analogical pressure gauge and a digital pressure transducer, D and E, respectively.

To carry out thermal treatments the vessel is placed in a heater equipped with a temperature control system that stabilizes the temperature within 1°C. Samples are put inside the vessel and the heater is switched on after the vessel was filled with the desired gas. At the end of thermal treatment, the heater is switched off and the samples are cooled in the treatment atmosphere. Heating and cooling times are about 2 and 7 hours, respectively. No diffusion kinetics were performed on the microemulsion samples due to the large thermal inertia of the Parr reactor that prevents fast heating and cooling of samples. Indeed, heating and cooling times are longer than the ones in which diffusion typically occurs (see next chapter).

In addition to thermal treatments to cause O_2 diffusion, high temperature thermal treatments were performed to induce structural variation in the network structure of nanoparticles as well as changes of the morphology. These treatments were performed either in a furnace in air or in the Parr reactor if controlled atmosphere was needed.

2.5 Determination of diffusion coefficient

The diffusion coefficient in this work has been determined by the analysis of the experimental data starting from the hypothesis of the Fick's theory reported in previous paragraphs. The solution of Fick's diffusion equation in a sphere (eq. 1.33) relative to a uniform initial concentration of diffusing substance, supposing that the concentration at the surface reaches its equilibrium value instantaneously, [35] can be integrated over the volume of the sphere and the following equation is obtained:

$$\frac{M(t) - M_i}{M_f - M_i} = 1 - \frac{6}{\pi^2} \sum_{n=1}^{\infty} \frac{1}{n^2} e^{-\frac{\pi^2 n^2 Dt}{a^2}} \tag{2.15}$$

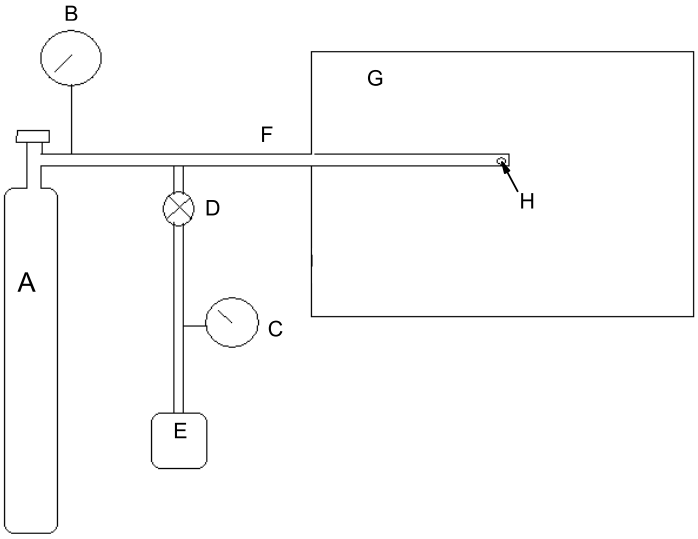

Figure 2.6: Experimental system used in sorption and desorption experiments. It is constituted by a O_2 bomb A, two pressure gauges (B and C), a vacuum pump E, a stainless steel blind pipe F and a furnace G. D is a valve and H is the sample.

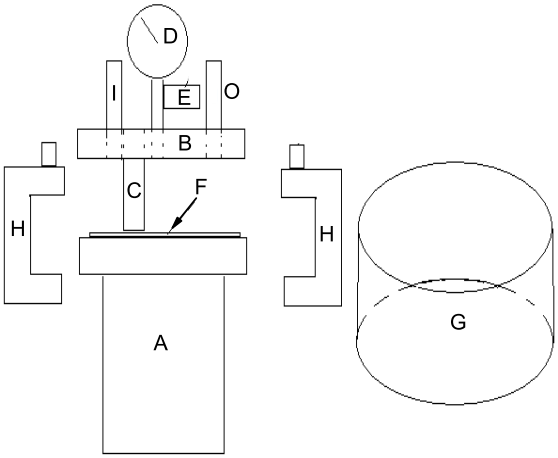

Figure 2.7: Schematic representation of Parr reactor. A is the vessel, B is the cover of the vessel, C is the well in which a thermocouple is placed, D and E are an analogical pressure gauge and a digital pressure transducer, respectively, F is a gasket, G and H a steel ring and two steel half-rings, respectively, for the closure of the system and I and O are the input and output valves for the gas, respectively.

where M_i, M_f and $M(t)$ are the mass of diffusing substance inside the sphere at initial, final and at time t, respectively. Obviously, if there are N identical spheres, eq. 2.15 is still valid and the diffusion coefficient can be determined by fitting the time evolution of the measured relative variation of interstitial O_2 mass with eq. 2.15 by supposing the silica sample to be constituted by identical spherical nanoparticles having diameter equal to the average one.

In a Raman/PL measurement of the samples used in this work, Raman scattering of silica and O_2 PL signals from several nanoparticles are collected. The amplitude of the O_2 PL band in these measurements is proportional to the mass of interstitial O_2 in the illuminated part of the sample, so the left hand side of eq. 2.15 is equal to the relative variation of the measured O_2 PL band.

In general, since the luminescence amplitude is proportional to the source power and to the mass of illuminated sample, errors could arise due to differences in the source power and/or in the illuminated silica mass in two different measurements. In order to prevent errors related to these effects, O_2 PL amplitude in opportunely normalized Raman/PL spectra has to be used to determine the relative variation of interstitial O_2 mass (left side of eq. 2.15). Indeed, since both O_2 PL amplitude and Raman scattering of silica are proportional to the source power, the power effect is removed by the normalization. Moreover, the Raman scattering of silica is a quantity proportional to the mass of illuminated silica, so the normalization prevents error related to different silica mass in different measurements. Basing on the above considerations the Raman/PL spectra were normalized to the silica Raman scattering value at 440 cm^{-1} Raman shift and the diffusion coefficient was found by fitting the relative variation of the O_2 PL band in the so normalized Raman/PL spectra with eq. 2.15.

It is worth noting that the above described method is the only one by which diffusion can be studied in a nanometer solid since measurements are performed on a macroscopic region of the sample. Indeed, other methods such as the time-lag or the steady state ones (described in sec. 1.2.4) cannot be used due to the nanometer size of the system. Likewise, the diffusion coefficient cannot be found by fitting the spatial distribution of diffusing O_2 with the expected mathematical law due to the impossibility to make measurements on a size resolution smaller than the nanoparticles size by our instrumentation.

2.6 Determination of interstitial O_2 concentration

Whereas only relative variation of interstitial O_2 is necessary in order to determine the diffusion coefficient, the absolute value of O_2 concentration has to be known to estimate the solubility of the molecules in the studied materials. Skuja et al. [113] found the way to quantify interstitial O_2 content in bulk silica by Raman spectra. They

found the proportionality factor between interstitial O_2 Raman scattering amplitude and the amplitude of the Raman bands of silica at 1065 cm^{-1} and 1200 cm^{-1} and estimated the O_2 concentration by comparing the Raman spectra of O_2 in air and that of an O_2 rich silica sample using an Ar ion laser source (514.53 nm). Moreover, they found the proportionality factor between interstitial O_2 PL amplitude at 1272 nm (1538 cm^{-1} Raman shift) and the Raman bands of silica at 1065 cm^{-1} and 1200 cm^{-1} by taking the Raman spectrum of the same silica sample by using a Nd:YAG laser source (1064.1 nm). Indeed, as described in sec. 1.4 this laser source is resonant with the transition of O_2 from the ground state to the first excited electronic one that decays giving a luminescence band at 1538 cm^{-1} Raman shift. A more accurate value of the conversion factor between interstitial O_2 concentration and its PL amplitude (band at 1538 cm^{-1} Raman shift) was found by Kajihara et al. [129] by comparing the change of the O_2 PL amplitude in an O_2 rich bulk silica sample annealed in vacuum and the number of desorbed molecules during the annealing, measured by the TDS technique (Thermal-Desorption Spectroscopy).

Agnello et al. [143] determined the conversion factor between the amplitude of O_2 PL band in the Raman/PL spectra of fumed silica and the concentration of interstitial O_2 by means of an experimental procedure similar to that used by Skuja et al. [113] in bulk silica. Experiments were performed on tablets of fumed silica obtained as described in sec. 2.4. In particular, fumed silica with average diameter of primary nanoparticles ranging from 7 to 40 nm were investigated. Tablets were loaded with O_2 by a thermal treatment in O_2 atmosphere at 200 °C and 50 bar in the Parr reactor described in sec. 2.4. Raman/PL spectra of so loaded samples are shown in Fig. 2.8 . Spectra were taken by the Raman spectrometer described in sec. 2.3 at 5 cm^{-1} spectral resolution. Spectra were normalized in order to have same amplitude of Raman band peaked at 800 cm^{-1}. In addition to Raman bands of silica and that of silanol groups (peaked at 980 cm^{-1}), the O_2 PL band peaked at 1538 cm^{-1} is present in the spectra. The amplitude of this band decreases on increasing the specific surface, that is decreasing the nanoparticles size.

Raman spectra of the same samples were taken also by micro-Raman measurements using a LabRAM ARAMIS Horibe-Scientific spectrometer equipped with a laser emitting at 633 nm. These Raman spectra, taken at the spectral resolution of 2 cm^{-1}, are shown in Fig. 2.9 in the spectral region between 1540 and 1565 cm^{-1}. As in the previous figure, spectra were normalized to have equal amplitude of silica Raman band at 800 cm^{-1} and the Raman spectrum of air is also shown for comparison. Unlike the case of Raman PL spectra, no luminescence band of interstitial O_2 is present in this spectra so the Raman band of O_2 can be observed. In particular, two Raman bands can be observed in Fig. 2.9. The band peaked at 1550 cm^{-1} is attributed to interstitial O_2 [113] whereas the band at 1556 cm^{-1} is due to O_2 present in the air contained in the

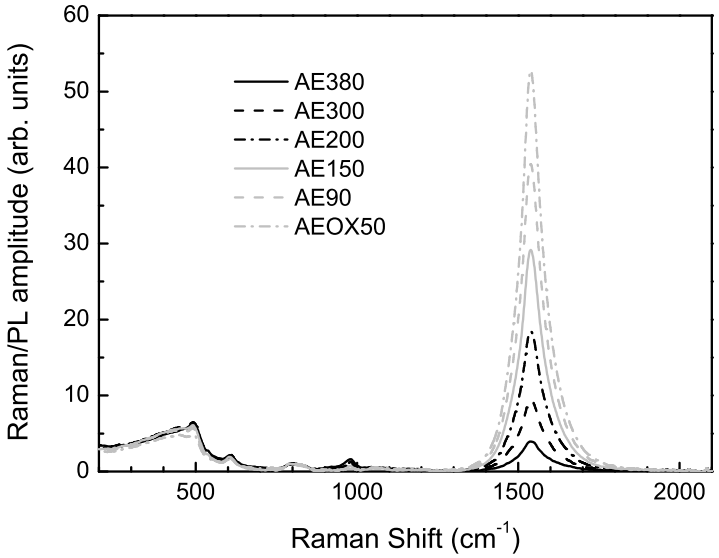

Figure 2.8: Raman/PL spectra of fumed silica loaded with interstitial O_2 at 200 °C and 50 bar. Spectra were normalized to have same amplitude of Raman band at 800 cm^{-1}. Adapted from Ref. [143].

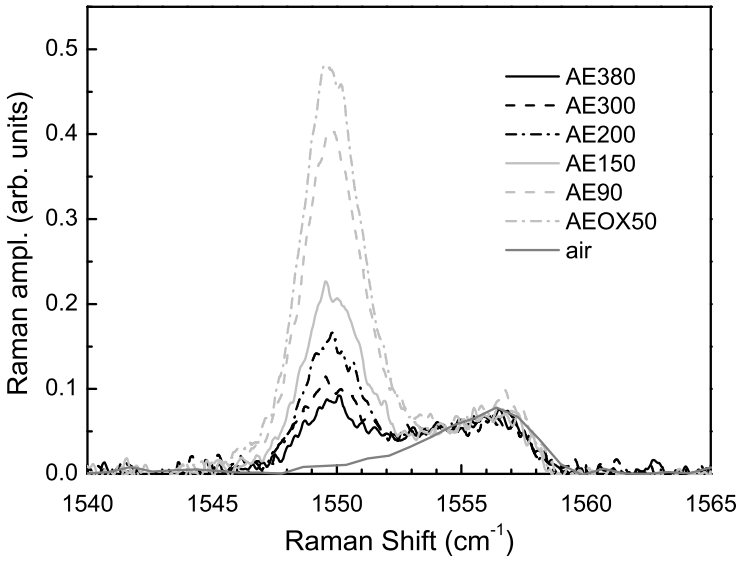

Figure 2.9: Raman bands of interstitial O_2 (peaked at 1550 cm^{-1}) and interparticles O_2 (1556 cm^{-1}) in Raman spectra of loaded fumed silica normalized to have same amplitude of Raman band at 800 cm^{-1}. Adapted from Ref. [143].

interstices between the nanoparticles. As in the case of O_2 PL band of Fig. 2.8, also the Raman band of O_2 inside the nanoparticles decreases on decreasing the nanoparticles size. Since the O_2 concentration in air is known, the concentration of O_2 inside the nanoparticles was found by comparing these two Raman bands by taking into account the polarizability of silica and the porosity of the tablets (50 %).

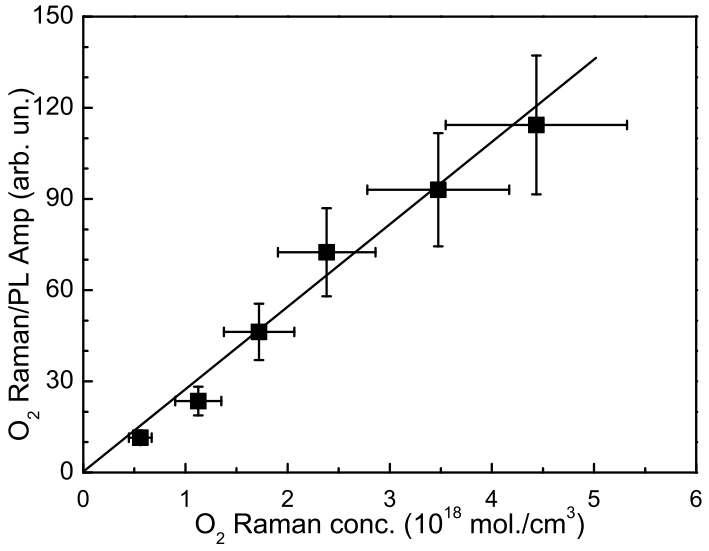

Figure 2.10: Amplitude of interstitial O_2 PL band in Raman/PL spectra corrected by the quantum yield as a function of O_2 concentation. The line is the best fit line. Adapted from Ref. [143].

Since the luminescence amplitude is proportional to the quantum yield that is different in nanoparticles with different size, a linear relation between the O_2 PL band corrected for the quantum yield and the O_2 concentration is expected. This relation is shown in Fig. 2.10 for the investigated nanoparticles types. The corrected PL amplitude of interstitial O_2 increases linearly with concentration and the reciprocal of the slope of the best fit line shown in the figure is $(4.0\pm0.8)\cdot10^{16}$ molecules/cm^{-3} that is in good agreement with the conversion factor found for bulk silica. The concentrations of interstitial O_2 in silica nanoparticles reported in this thesis work are determined by the amplitude of O_2 PL band at 1538 cm^{-1} in Raman/PL spectra by taking into account the different quantum yield of O_2 in silica nanoparticles of different size.

Chapter 3

Study of diffusion in AEOX50

In this chapter, experimental results on the diffusion process in the AEOX50 sample, fumed silica consisting of 40 nm average diameter particles, are shown and discussed. The diffusion process was studied by desorption of O_2 present in the as-received sample and by sorption experiments by putting the sample in O_2 atmosphere. Kinetics aspects of the diffusion process were studied in the temperature range from 98 °C to 177 °C in ambient atmosphere or in O_2 atmosphere at 6 bar and 66 bar whereas the O_2 equilibrium concentration was investigated in the temperature range from 127 °C to 244 °C changing the external pressure from 0.2 bar (partial O_2 pressure in ambient atmosphere) to 76 bar. In addition, a sorption-desorption experiment was carried out to better investigate the role played by the value of O_2 concentration in the diffusion process. The dependence of the concentration of interstitial O_2 at the diffusive equilibrium on external pressure and temperature was also investigated to highlight features of solubility related to the nanometric nature of the studied system.

3.1 Results

3.1.1 Desorption kinetics

In the here reported experiments the nanoparticles have been treated for increasing time at different temperatures in ambient atmosphere. Fig. 3.1 shows the time evolution of the Raman/PL spectrum of the sample AEOX50 thermally treated in air at 127 °C for increasing time, as reported in the legend of the figure. As already stated, it is worth to remember that a new sample has been used for each treatment. Raman bands of silica are not affected by the thermal treatments proving that the silica network is not modified by them whereas there is a variation of the amplitude of the luminescence band of interstitial O_2 at 1538 cm^{-1} Raman shift. Interstitial O_2 is present in the as-received sample (spectrum labeled 0 min)(see appendix B for further explanations), as can be seen from the starting amplitude of the interstitial O_2 band, and the O_2 content decreases on increasing the thermal treatment time up to reach a time independent value. A similar behavior was observed during thermal treatments in air at 98 °C, 143

°C, 157 °C and 177 °C.

Desorption kinetics relative to all the investigated temperatures are shown in Fig. 3.2. The relative variation of interstitial O_2 mass is reported as a function of $\frac{t}{a^2}$ where a is the average radius of nanoparticles (20 nm). Since kinetics are relative to the same sample, the x-axis scale can be read as a time scale. Relative variation of mass increases on increasing the thermal treatment time due to desorption of interstitial O_2. Desorption rate decreases with time until the mass of interstitial O_2 reaches the constant value relative to diffusive equilibrium. Desorption rate is temperature dependent showing the process to be faster at higher temperatures.

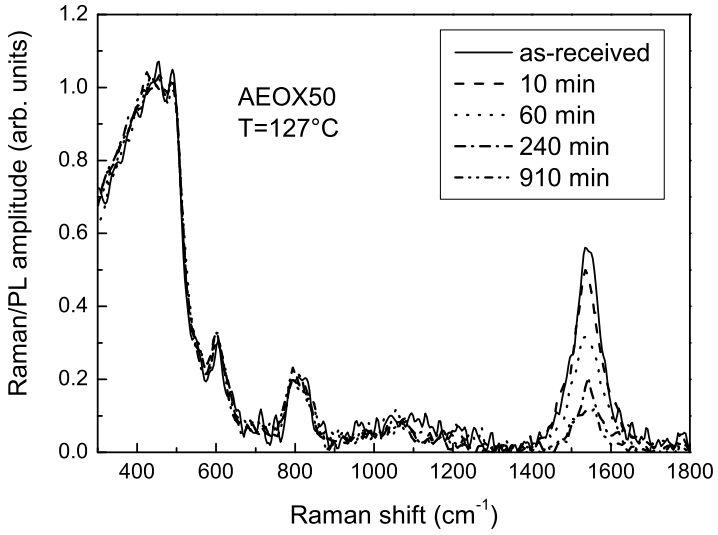

Figure 3.1: Raman/PL spectra of the AEOX50 as-received (0 min) and after thermal treatments in air of increasing duration, as reported in the legend. Raman/PL spectra are normalized to the Raman signal value at 440 cm^{-1}.

3.1.2 Sorption and sorption-desorption kinetics

In this paragraph the effects of thermal treatments in controlled O_2 atmosphere are illustrated. Samples were preliminarily annealed in air at 300 °C (Raman/PL spectrum labeled 0 min in Fig. 3.3) in order to desorb the O_2 present in the as-received powder, successively they were annealed in O_2. Fig. 3.3 shows the Raman/PL spectra of the sample after thermal treatments of increasing duration at 127 °C in O_2 atmosphere at 6 bar pressure. As in the case of desorption experiments, Raman bands of silica do not change during the thermal treatments whereas the amplitude of the interstitial O_2 luminescence band is a function of the treatment time. In particular, the amplitude increases on increasing the treatment time until a time independent value is reached. The increase of the luminescence band is due to the diffusion of O_2 molecules from the

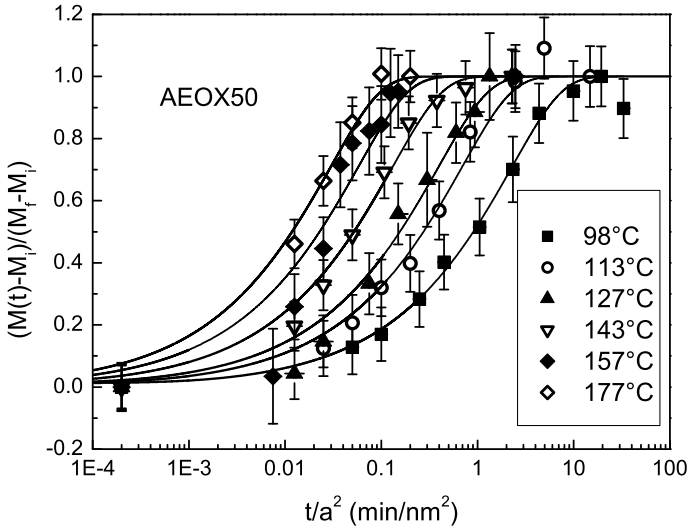

Figure 3.2: Desorption kinetics of the AEOX50 sample at various temperatures as reported in the legend. Thermal treatments were carried out in air. M_i, M_f and M(t) are the initial, final and at time t masses of interstitial O_2, respectively, and a is the average radius of primary nanoparticles (20 nm). First points are relative to t=0. Lines are the best fit curves obtained by fitting the experimental data with eq. 2.15.

treatment atmosphere into silica nanoparticles. If the external O_2 pressure is increased, the equilibrium O_2 concentration increases as can be seen in Fig. 3.4 where the time evolution of the average concentration of interstitial O_2 is reported in the sorption experiments carried out either at 6 or 66 bar external O_2 pressure and 127 °C. In addition, for comparison, the time dependence of O_2 average concentration in the desorption experiment at the same temperature (labeled "in air") is shown.

A similar behavior was observed in sorption experiments carried out at 143 °C, 157 °C and 177 °C. Sorption kinetics at the investigated temperatures and pressures are shown in Fig. 3.5 and, for comparison, desorption kinetics are also reported. As observed for desorption kinetics, the sorption ones are faster at higher temperature, for a fixed pressure, furthermore they are faster at higher pressure at fixed temperature. Desorption kinetics are slower than sorption ones in all the investigated cases.

In order to better investigate the properties of the diffusion process, a desorption after sorption experiment was carried out. Data relative to this experiment are shown in Fig. 3.6. The sample was first loaded with O_2 in a sorption experiment at 143 °C and 66 bar then desorption was carried out in air at the same temperature. In addition to this two kinetics, the desorption kinetics of O_2 present in the as-received sample performed at the same temperature is also shown. Experimental data show that sorption kinetic is faster than the desorption one and that the two desorption kinetics

are equal within experimental errors.

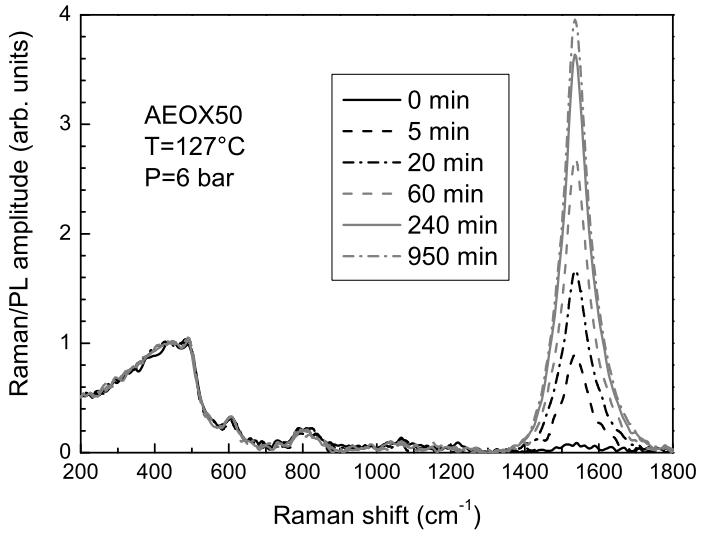

Figure 3.3: Raman/PL spectra of the AEOX50 after annealing at 300 °C for 5 min (labeled 0 min) then thermally treated in O_2 atmosphere at 127 °C and 6 bar for increasing times as reported in the legend. Raman/PL spectra are normalized to Raman signal value at 440 cm^{-1}.

3.1.3 Equilibrium concentration

Fig. 3.7 shows the dependence of the equilibrium concentration of interstitial O_2 on the external pressure below 13 bar for different temperatures as reported in the legend of the figure. At every temperature the O_2 concentration increases linearly with pressure whereas it decreases on increasing temperature at each pressure value. At higher pressure a departure from linear behavior is found, as can be seen in Fig. 3.8 where the equilibrium concentration value as a function of the external pressure in a wider pressure range is shown. Experimental data display a saturation tendency for pressure above 60 bar and a saturation value of concentration independent on temperature.

3.2 Discussion

3.2.1 Diffusion kinetics

The dependence of the diffusion kinetics on temperature and pressure was investigated in this work in the widest range accessible by the experimental conditions. One of these conditions is that times necessary for the sample to reach the thermal treatment temperature and to cool to room temperature have to be much shorter than the evolution time of the diffusion process. Indeed, if this conditions are not fulfilled, the measured

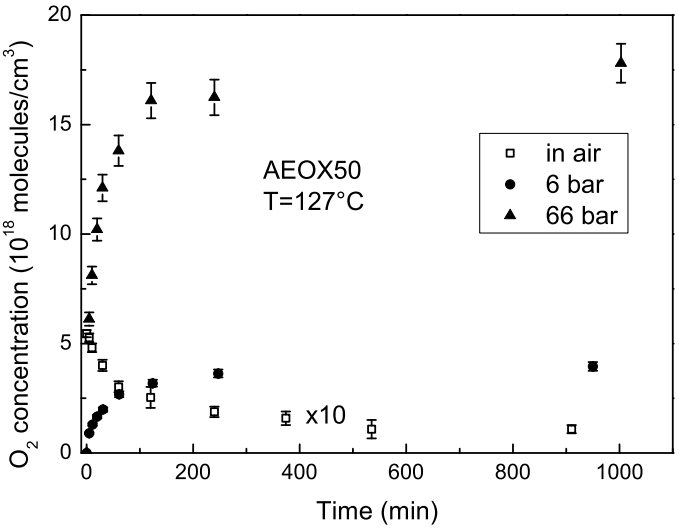

Figure 3.4: Time evolution of interstitial average O_2 concentration in the AEOX50 sample at 127 °C and 6 bar or 66 bar in O_2 atmosphere. Data relative to desorption (labeled "in air") at the same temperature are also shown for comparison. Desorption data are multiplied by a factor 10 for clarity.

diffusion kinetics are affected by warming and cooling times. Obviously, this feature imposes an upper limit to the temperature at which the diffusion process can be studied. Diffusion kinetics in Fig. 3.5 shows that after 5 minutes thermal treatments in O_2 at 66 bar and 177 °C the relative variation of interstitial O_2 is about 70%. Since warming and cooling times are about 2 min and 1 min, respectively, 177 °C was chosen as the upper limit for the investigation of diffusion kinetics. On the other hand, if temperature is too low, diffusion kinetics become too long to be investigated in laboratory time, so 98 °C was chosen as the lower limit of the investigated temperature range since a kinetics at this temperature takes about 15 h as evidenced in Fig. 3.2 by desorption experiments. Lower temperature limit was also imposed by O_2 losses of the experimental system that limited the duration of sorption experiments. The upper limit of investigated pressure range was determined by mechanical properties of the experimental set-up.

As described in the previous chapter, diffusion coefficients were determined by fitting the experimental data with eq. 2.15. The obtained values are collected in Table 3.1 and the best fit curves are shown in Figs. 3.2 and 3.5. As reported in the figures, a good agreement is found between the solution of Fick's equation and the experimental data in almost all the investigated cases. Even if the best fit curves finely describe the experimental data, the applicability of Fick's theory has to be discussed due to the low concentration of diffusing matter and the small size of the medium in which the

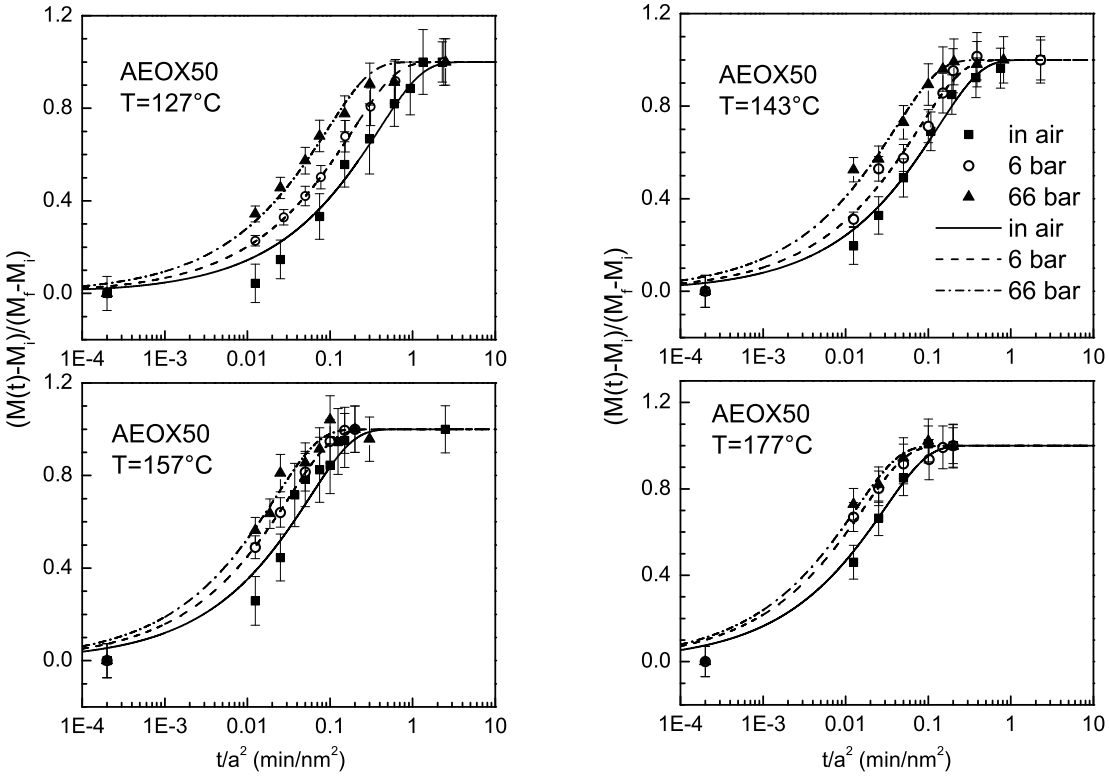

Figure 3.5: Diffusion kinetics in the AEOX50 sample at various temperatures and external pressures as reported in the legends. Sorption kinetics were carried out in O_2 atmosphere at 6 or 66 bar at different temperatures. Desorption kinetics (labeled as "in air") are also shown for comparison. M_i, M_f and M(t) are the initial, final and at time t masses of interstitial O_2, respectively, and a is the average radius of primary nanoparticles (20 nm). First points are relative to t=0. Lines are the best fit curves obtained by fitting experimental data with eq. 2.15.

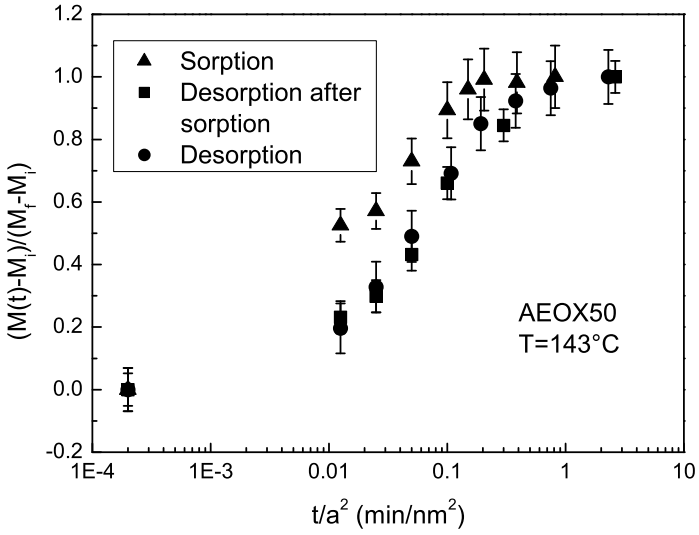

Figure 3.6: Sorption and desorption after sorption in the AEOX50 sample at 143 °C. Sorption was carried out at 66 bar whereas desorption after sorption was performed in air. Kinetics relative to desorption of O_2 present in the as-received sample is shown for comparison. M_i, M_f and M(t) are the initial, final and at time t masses of interstitial O_2, respectively, and a is the average radius of primary nanoparticles (20 nm). First points are relative to t=0.

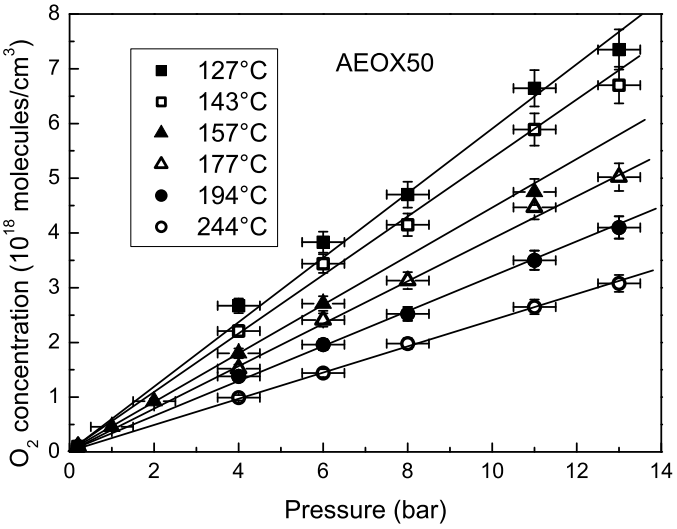

Figure 3.7: Pressure dependence of the O_2 equilibrium concentration at low pressure in the AEOX50 sample at various temperatures. Lines are the linear best fit.

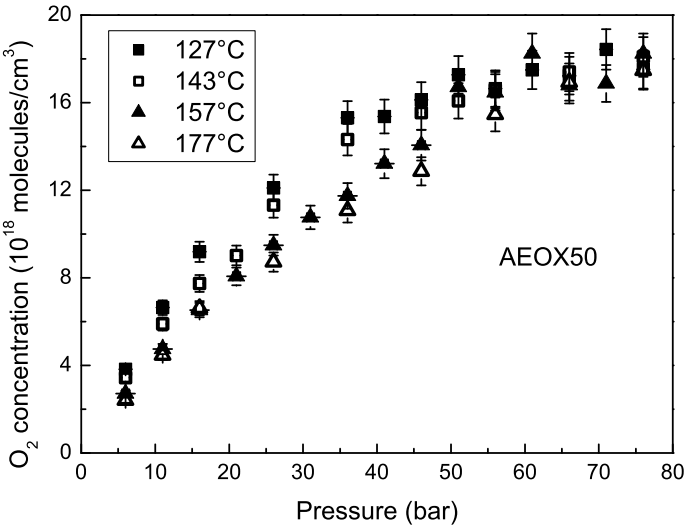

Figure 3.8: Dependence of O_2 equilibrium concentration on pressure in AEOX50 sample at various temperatures.

diffusion process takes place.

Table 3.1: Diffusion coefficients in nm^2/min at investigated temperatures and pressures determined by fitting the experimental diffusion kinetics with Eq. 2.15. Experimental data and best fit curves are shown in Figs. 3.2 and 3.5. "in air" refers to desorption of O_2 present in the as-received sample. Values in "6 bar" and "66 bar" columns are relative to sorption kinetics at 6 bar and 66 bar O_2 pressure, respectively.

Temperature (°C)	in air	6 bar	66 bar
98	0.04 ± 0.02		
113	0.11 ±0.04		
127	0.18 ± 0.06	0.4 ± 0.1	0.8 ± 0.2
143	0.6 ± 0.2	1.0 ± 0.2	1.9 ± 0.4
157	1.3 ± 0.4	2.4 ± 0.5	3.5 ± 1.1
177	2.6 ± 0.7	4.7 ± 1.2	6 ± 2

On the basis of the concentration values shown in Fig. 3.4, the average number of O_2 molecules per particle is less than 20 in desorption kinetics and less than 130 and 600 in sorption kinetics at 6 bar and 66 bar, respectively. Application of Fick's diffusion theory requires that the medium can be divided in parts small with respect to the size of the body in which diffusion takes place, but large enough to contain a statistically significant number of diffusing molecules [35]. Due to the estimated small number of molecules inside the nanoparticles, the Fick's diffusion theory is not directly applicable to a single nanoparticle. However, the measurements of the mass of interstitial O_2

are made over a macroscopic volume of sample so a great number of nanoparticles is involved and this aspect makes Fick's diffusion theory applicable as explained in what follows.

Suppose to have a great number N of identical spheres with low concentration of diffusing molecules and suppose to have an imaginary sphere of the same size of the real ones filled with imaginary molecules having the same positions as the real molecules inside the N real spheres. Since the real molecules move according to a random walk, even the motion of the imaginary molecules is random and, if N is large enough, the conditions under which the Fick's diffusion theory is applicable in the imaginary sphere are fulfilled. Then, eq. 2.15 gives the correct time dependence of the fractional variation of the interstitial O_2 in the imaginary sphere. The fractional variation of the total O_2 mass inside the N spheres, the experimental measured quantity, is equal to that of the imaginary sphere because when a molecule comes in or goes out from the imaginary sphere a molecule enters or exits a real sphere so eq. 2.15 can be used to describe experimental data.

Even if the low concentration of interstitial O_2 and the reduced size of nanoparticles do not limit the applicability of Fick's theory, found values of diffusion coefficient do not agree with the assumptions under which eq. 2.15 was determined. Indeed, the law used to fit the data is relative to a physical system in which the diffusion coefficient does not depend on the concentration of diffusing substance, whereas different values of the diffusion coefficient were found in the investigated system by varying the external O_2 pressure and as a consequence the concentration of O_2 inside the nanoparticles. Assuming that the variability found of the diffusion coefficient is due to a dependence on concentration, the obtained values are, as a first approximation, the averages over the concentration range explored in the relative kinetics [41].

On the other side, simulative and experimental data showed that silica nanoparticles are constituted by a core region, whose characteristics are similar to that of bulk silica and a surface shell having a thickness of about 1 nm in which bonds are stressed and density is about 2.4 g/cm^3 [19, 20, 116], so diffusion could be different in these two regions of the nanoparticle. Then, nanoparticles should be treated as composite spheres and not as homogeneous ones for which eq. 2.15 is valid, but the case of composite medium cannot be treated analytically so nanoparticles were considered homogeneous as a first approximation. In order to estimate the error related to this approximation, a comparison can be made between the simulative data on O_2 diffusion through a thin silica film grown on silicon during the oxidation process of silicon [144]. Simulations give the value of diffusion coefficient at 1300 K as a function of the silica film thickness considering the presence of a densified layer (2.4 g/cm^3) near the silica-silicon interface about 1 nm thick. Simulative data showed the average diffusion coefficient is higher than in bulk silica if the oxide layer is thinner than 1.5 nm, lower than the bulk silica one

if its thickness is between 1.5 nm and 8 nm whereas it is equal to the diffusion coefficient in bulk silica for larger thickness. The enhancement of the diffusion coefficient when the oxide layer is thick less than 1.5 nm is due to percolative motions of O_2 molecules and is in good agreement with experimental data on the silicon oxidation rate at the beginning of the process when the oxide layer is very narrow. Since values of density and thickness of the densified layer in this system are very similar to that of the surface shell in fumed silica [116], it can be assumed that simulative data can be applied to nanoparticles. By comparing the average nanoparticles radius (20 nm) and the overall layer thickness above which the diffusion coefficient is the same as in bulk silica (8 nm), it can be assumed that the approximation of homogeneous sphere does not affect the data analysis.

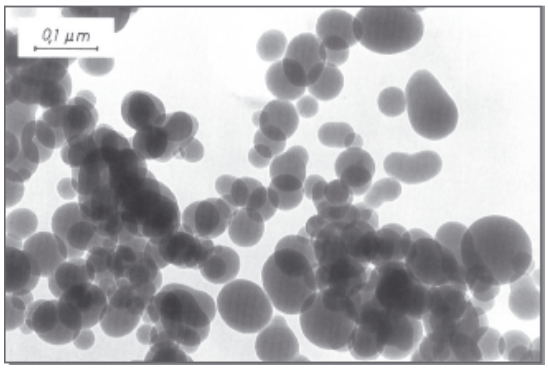

Figure 3.9: TEM image of AEOX50 powder. Adapted from Ref. [130]

In addition to the approximations of homogeneous medium and of concentration independent diffusion coefficient, other approximations regarding morphological features of the nanoparticles were done. Departures from spherical shape as well as the presence of a size distribution should be taken into account as evidenced by the TEM image reported in Fig. 3.9. The effect of shape distortions is difficult to be considered quantitatively but the qualitative effect should be an overestimation of the diffusion coefficient. Indeed, the surface to volume ratio is minimum for a sphere so if the experimental diffusion kinetics of a non spherical body having volume equal to a sphere, is fitted with the spherical solution, the found diffusion coefficient will be greater than the true one. The effect of size distribution can be taken into account by averaging eq. 2.15. This equation can be put in the form:

$$M^j(t) = (M_f^j - M_i^j)(1 - \frac{6}{\pi^2}\sum_{n=1}^{\infty}\frac{1}{n^2}e^{-\frac{\pi^2 n^2 Dt}{a_j^2}}) + M_i^j \tag{3.1}$$

where M_i^j, M_f^j and $M^j(t)$ are initial, final and at time t mass, respectively, of the

diffusing substance into a sphere having radius a_j. Since the measurement is made on a macroscopic part of the sample composed of many nanoparticles, the measured quantity is

$$M(t) = \sum_j (M_f^j - M_i^j)(1 - \frac{6}{\pi^2} \sum_{n=1}^{\infty} \frac{1}{n^2} e^{-\frac{\pi^2 n^2 Dt}{a_j^2}}) + M_i \tag{3.2}$$

where $M_i = \sum_j M_i^j$ and $M(t) = \sum_j M^j(t)$ are initial and at time t mass of interstitial O_2, respectively, inside the sample volume in which the measurement is performed. Moving the term M_i to the left side of eq. 3.2, and dividing both sides by $M_f - M_i = \sum_k (M_f^k - M_i^k) = \sum_k (C_f - C_i)\frac{4\pi a_k^3}{3}$, where $M_f = \sum_k M_f^k$ is the final mass of the interstitial O_2 inside the sample, and C_i and C_f its initial and final concentrations, eq. 3.3 is obtained

$$\frac{M(t) - M_i}{M_f - M_i} = \sum_j \frac{a_j^3}{\sum_k a_k^3} (1 - \frac{6}{\pi^2} \sum_{n=1}^{\infty} \frac{1}{n^2} e^{-\frac{\pi^2 n^2 Dt}{a_j^2}}) \tag{3.3}$$

Since the measurement involves about 10^{13} nanoparticles, replacing the summation with $\int \rho(a)da$ (where $\rho(a)da$ is the number of particles having radius between a and $a + da$) is reasonable, so eq. 3.3 becomes

$$\frac{M(t) - M_i}{M_f - M_i} = \frac{1}{\int \rho(a)a^3 da} \int \rho(a)a^3 (1 - \frac{6}{\pi^2} \sum_{n=1}^{\infty} \frac{1}{n^2} e^{-\frac{\pi^2 n^2 Dt}{a^2}}) da \tag{3.4}$$

where the integration is carried out over the whole range of particles radii. According to eq. 3.4, eq. 2.15 has to be averaged by using the distribution function $a^3\rho(a)$ in order to take into account the particles size distribution. Due to a^3 factor, bigger nanoparticles have a greater weight in the average and the approximation of homogeneous sphere becomes stronger.

The effect of size distribution on the diffusion kinetics is shown in Fig. 3.10 where distribution of primary particles from Ref. [130] was used. Curve A is the best fit curve obtained by fitting the experimental data, relative to sorption at 143 °C and 6 bar, with the function reported in eq. 2.15 in which the size distribution effect is not accounted. Curve B is the plot of eq. 3.4 by using the value D = 1.0 nm^2/min that is the best fit parameter of eq. 2.15. Whereas the agreement between experimental data and eq. 2.15 is good if D = 1.0 nm^2/min, experimental data are not well described by eq. 3.4 by using D = 1.0 nm^2/min. The value D = 1.7±0.3 nm^2/min is obtained if the experimental data are best fitted by the function of eq. 3.4 (curve c in Fig. 3.10). Curves shown in Fig. 3.10 suggest that neglecting the size distribution gives an underestimation of the diffusion coefficient however, although the value of the two diffusion coefficients are different, the effect of size distribution is not dramatic. Moreover, it is worth noting

that the value 1.7±0.3 nm^2/min could be overestimated because it does not account for the geometrical departure from spherical shape and that this effect should bring to an overestimation of diffusion coefficient so a compensation between these two effects should take place.

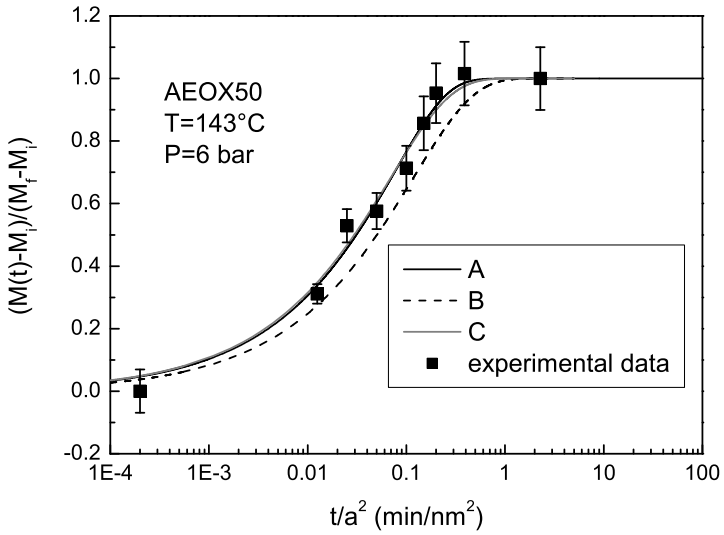

Figure 3.10: Sorption kinetics in the AEOX50 sample at 143 °C and 6 bar. Curve A is the best fit obtained by fitting experimental data with the function reported in eq. 2.15 (D = 1.0±0.2 nm^2/min). Curve B is the diffusion kinetics obtained by eq. 3.4 by using the diffusion coefficient relative to A curve. C is the best fit curve obtained by fitting experimental data with eq. 3.4 (best fit diffusion coefficient D = 1.7±0.3 nm^2/min).

Although size distribution could affect the absolute value of the found diffusion coefficient relative to a given diffusion kinetics, neither differences between sorption and desorption nor those among sorption kinetics at different external pressures can be due to the size distribution effects. Indeed, if there is no dependence of the diffusion kinetics in single size nanoparticles on the process type (sorption or desorption) or on pressure, no such effects can arise by averaging over the size distribution. Such effects could be related to a dependence of the diffusion coefficient on the concentration and/or to an improper boundary condition [35]. In order to better investigate these hypotheses, sorption and desorption experiments at the same temperature were performed. Experimental data relative to these experiments are reported in Fig. 3.6 and show that sorption kinetics depend on external pressure whereas desorption kinetics do not. In general, if the diffusion coefficient depends on concentration, there are differences between sorption and desorption kinetics. In the sorption kinetics at 6 bar the value of interstitial O_2 concentration ranges from about $0.1 \cdot 10^{18}$ cm^{-3} up to $3.4 \cdot 10^{18}$ cm^{-3}, in sorption at 66 bar from $0.1 \cdot 10^{18}$ cm^{-3} up to $17 \cdot 10^{18}$ cm^{-3} , in desorption in air

of the sample loaded at 66 bar from $17 \cdot 10^{18}$ cm^{-3} down to $0.1 \cdot 10^{18}$ cm^{-3} and in desorption of the as-received sample from $0.6 \cdot 10^{18}$ cm^{-3} down to $0.1 \cdot 10^{18}$ cm^{-3} . The values of the diffusion coefficients should be, as a first approximation, the average on the concentrations explored in the diffusion kinetics [35] but whereas sorption kinetics at 6 bar and 66 bar are different, no difference is observed between desorption in air for the as-received sample and for the sample loaded at 66 bar, notwithstanding the different O_2 concentration ranges. This suggests a different dependence on concentration between sorption and desorption or an important role played by the external pressure since the two desorption kinetics were performed at the same external pressure value.

The only way for a diffusion kinetics to depend on the external pressure is through boundary conditions. The boundary condition used to fit experimental data is that surface instantaneously reaches the equilibrium value, that is surface dissolution rate was supposed to be infinite. In this frame no dependence on the external pressure can arise so a finite rate of surface dissolution should be considered and in addition it should depend on the external pressure in order to explain the observed behavior.

Kajihara et al. [145] investigated the effect of the surface dissolution kinetics on bulk silica (a sheet 0.5 cm thick) at 900 °C in ambient atmosphere by fitting the experimental sorption kinetics with the solution of Fick's diffusion equation supposing an exponential surface dissolution law. They found that the ratio $K = \frac{L^2}{4D\tau}$ between the diffusion time ($\frac{L^2}{4D}$ where D is the diffusion coefficient and L the sample thickness) and the dissolution time τ (the exponential characteristic time) is about 300. Moreover, they found by numerical simulations that diffusion kinetics is affected by surface dissolution if $K < 100$. K value depends on the size of the medium in which diffusion occurs, so the approximation of infinite surface dissolution rate worsens if the size is reduced. At the conditions under which Kajihara et al. worked, $K = 10$ if the sample is 1 mm thick and $K = 1$ if the thickness is 350 μm, so it is guessed that the dissolution kinetics could affect the diffusion kinetics reported in this chapter.

In the surface dissolution model used by Kajihara et al., there is no dependence on the external concentration since they supposed that the number of molecules dissolving in the unit time is proportional to the constant external concentration whereas the number of molecules leaving the surface is proportional to dissolved molecules. This model gives an exponential dissolution kinetics with a decay time equal to $1/k_{out}$ where k_{out} is the exit rate of dissolved molecules. Moreover, this model predicts a linear increase of the internal concentration with the external one and is not applicable to silica nanoparticles in the wide investigated pressure range due to saturation of concentration at high pressure. Obviously in this frame, the pressure effect on diffusion kinetics observed in silica nanoparticles cannot be explained.

A model that could take into account the saturation of dissolved molecules at high pressure is the Langmuir model [28]. As shown in sec. 1.1, the equilibrium value

predicted by the Langmuir model is the stationary solution of eq. 1.6. This equation can be rearranged in the form given in eq. 3.5

$$\frac{d}{dt}C = -(k_{out} + \frac{k_{in}}{C_{max}}P)C + k_{in}P \tag{3.5}$$

where C_{max} and C are the maximum and the actual concentration of dissolved molecules, k_{in} is the dissolution rate constant, k_{out} is the desorption rate constant and P is the external pressure. This equation predicts an exponential dissolution kinetics with a decay time $\tau = (k_{out} + \frac{k_{in}}{C_{max}}P)^{-1}$ that decreases on increasing the external pressure. This behavior is qualitatively in agreement with the experimental data because a decrease of the dissolution time makes kinetics faster. As it will be seen in the next section, Langmuir model is not rigorously applicable to equilibrium concentration in the investigated system. However, from a qualitatively point of view, it can be stated that the behavior of the system agrees with the Langmuir model and a dependence on pressure could be expected within it.

It is worth noting that it is very difficult to take into account the effect of dissolution kinetics on the diffusion one by fitting the experimental data with a solution in which a finite dissolution time is supposed. Difficulties are due to the lack of knowledge about the time dependence of the dissolution kinetics and on relatively high errors affecting the experimental data. Indeed, experimental kinetics are well fitted, within the experimental errors, by the solution relative to infinite dissolution rate so the addition of a new parameter in the fitting law will make the fitting procedure undetermined. Due to the approximations used to determine the diffusion coefficients, from here on, they will be referred to as effective diffusion coefficients.

Until now, only the dependence of diffusion kinetics and effective diffusion coefficient at fixed temperature were discussed. The effective diffusion coefficient has been found to depend on temperature, as qualitatively shown in Figs. 3.2 and 3.5, and reported in Table 3.1. These latter data are collected in Fig. 3.11. The linear trend of values in the Arrhenius plot of Fig. 3.11 indicates that the effective diffusion coefficient, for each pressure, increases on increasing temperature according to an Arrhenius law. Best fit Arrhenius curves are the lines in Fig. 3.11 and the best fitted parameters are collected in Table 3.2. For each of the Arrhenius laws both the pre-exponential factor and activation energy, are lower than those from literature relative to temperature from 800 °C to 1200 °C and reported in Table 1.1 [56]. A similar behavior was observed for helium diffusion in bulk silica and was related to structural disorder of the matrix [47]. In that case, the pre-exponential factor decreased of about an order of magnitude from 900 °C to 100 °C whereas the activation energy was reduced of about 20% in the same temperature range. In the present case, the pre-exponential factor is about up to 80 times lower than that relative to the interval from 800 °C to 1200 °C, whereas the

activation energy is about up to 20% lower.

A variability of the Arrhenius parameters under the here investigated thermodynamical conditions is found, the pre-exponential factor increases when pressure is changed from 0.2 bar to 6 bar and decreases when it is risen to 66 bar. The activation energy has the same value at 0.2 bar and 6 bar whereas it is lower at 66 bar. Since the effective diffusion coefficients are affected by size distribution, non-spherical shape and dissolution kinetics, the dependence of the Arrhenius parameters could be related to the investigated system and to the approximations. Indeed, the dissolution time depends both on pressure and temperature. At a given pressure, the effect on the effective diffusion coefficient due to dissolution kinetics could be temperature dependent because it depends on the ratio between the diffusion and dissolution times that should have different temperature dependence. Even if the effective diffusion coefficient could be affected by the above cited approximations, its value should not be too different from that expected for the true diffusion coefficient. Indeed, the effective diffusion coefficient values are compatible with values extrapolated from bulk silica samples as can be seen in Fig. 3.11, where dashed lines are the extremals Arrhenius laws drawn by using the parameters from literature relative to experiments performed at temperatures above 800 °C and pressure lower than 3 bar [56]. The found values are within the variability interval of expected values of diffusion coefficient.

Table 3.2: Best fit parameters of the Arrhenius law in Fig. 3.11. "in air" refers to desorption of O_2 present in as-received sample whereas "6 bar" and "66 bar" are for sorption kinetics at 6 bar and 66 bar O_2 pressure, respectively.

Pressure	D_0 (nm^2/min)	E_a(eV)
in air	$10^{9.2\pm1.0}$	0.79 ± 0.08
6 bar	$10^{9.3\pm0.7}$	0.78 ± 0.06
66 bar	$10^{7.8\pm0.7}$	0.63 ± 0.06

3.2.2 Equilibrium concentration

The linear dependence of the equilibrium O_2 concentration shows that below 13 bar the system follows Henry's law at investigated temperatures [26]. In this pressure range, the slope of each straight line is the O_2 solubility. Slopes of best fit straight lines drawn in Fig. 3.7 are reported in Table 3.3. Solubility increases on decreasing temperature. In order to analyze quantitatively this temperature dependence, the found values of solubility are plotted in the Arrhenius graph in Fig. 3.12. The solid line in the figure is the best fit line obtained by fitting the experimental data with the Arrhenius law of the solubility (eq. 1.43) whereas the dashed lines are the extremals Arrhenius laws drawn by using Arrhenius parameters from literature relative to experiments performed at temperatures above 500 °C and pressure lower than 3 bar in bulk silica [56]. Parameters

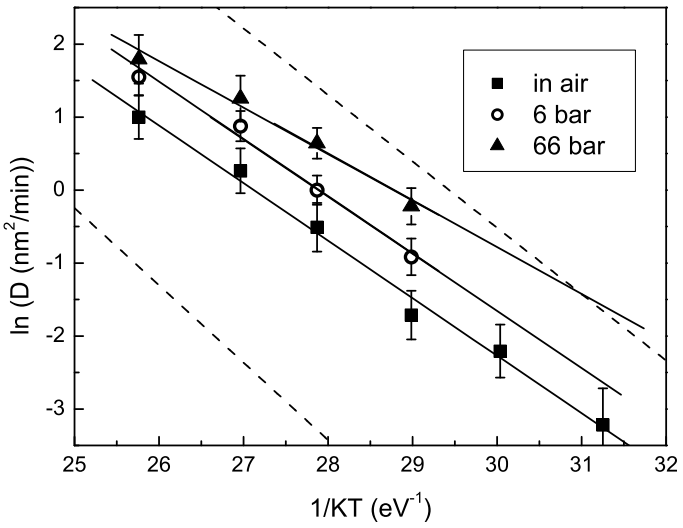

Figure 3.11: Arrhenius plot of diffusion coefficients of Table 3.1. "in air" refers to desorption of O_2 present in as-received sample whereas "6 bar" and "66 bar" are for sorption kinetics at 6 bar and 66 bar O_2 pressure, respectively. Solid straight lines are the best fit curves obtained by fitting the values with the Arrhenius law (eq. 1.34). Dashed lines are the extremals Arrhenius laws drawn by using the parameters from literature relative to experiments performed at temperatures above 500 °C and pressure lower than 3 bar [56].

of the best fit Arrhenius law are $S_0 = 10^{15.9\pm0.3}$ molecules cm^{-3}/bar and $\widetilde{E}_a = -0.13 \pm 0.03$ eV. The negative value of $\widetilde{E}_a$ means that, in average, the system constituted by silica and O_2 lowers its energy during the dissolution process. The relative position between experimental data and dashed lines, as well as the comparison between best fit parameters and values of Arrhenius parameters reported in Table 1.1, suggest that O_2 solubility in 20 nm radius silica particles follows the same law as that describing solubility in bulk silica at higher temperature.

Equilibrium values of interstitial O_2 concentration at the investigated temperature in a wider pressure range show a departure from the linear behavior predicted by Henry's law and saturation above about 60 bar. From a qualitative point of view, this behavior is theoretically expected on the basis of the Langmuir model and was experimentally observed for dissolution of He in bulk silica [27]. The departure of helium equilibrium concentration from Henry's law was observed at pressure much higher than that explored in this work and no saturation was observed up to 1300 atm (upper limit of investigated pressure range) [27]. Moreover, in that work, experimental data were found to be in agreement with the Langmuir model. The equilibrium concentration at a given pressure predicted by the Langmuir model is given by eq. 1.7 and depends only on two parameters, the solubility S and the saturation concentration C_{max}. Solubility values determined at low pressure and the maximum concentration in our experiments were used to draw the solid lines in Fig. 3.13, representing the equilibrium concentration as predicted by the Langmuir model. Comparison between curves and experimental data shows that the model does not agree with the observed behavior. Dashed lines in Fig. 3.13 are the Langmuir isotherms in which solubility was put equal to that experimentally observed and the value of C_{max} was fixed at $5.5 \cdot 10^{21}$ molecules cm^{-3} [144]. This value, that is about three orders of magnitude greater than that experimentally observed in this work, is the concentration of interstices in which O_2 can be trapped, as theoretically predicted for bulk silica [144]. Moreover, this concentration value is near to $1.9 \cdot 10^{21}$ molecules cm^{-3} [27], that was determined by fitting experimental data for He in bulk silica, since this system is described by the Langmuir model. Dashed lines are straight lines with good approximation in the range from 0 bar to 76 bar predicting the validity of Henry's law in the experimentally investigated pressure range. Comparison between the experimental data and dashed lines reveals that the observed concentration is lower than the expected one.

The differences between the values predicted by the dashed lines and the experimental data for each temperature, reported in Fig. 3.14, show that the accuracy of the model increases with temperature. There could be reasons justifying why the Langmuir model is not fully applicable to O_2 in silica. One of the basis hypothesis under which Langmuir isotherm is obtained is that all sites are equivalent but this could not be true for O_2 in silica due to its amorphous nature [146]. Other basic assumption is that

there is no interaction between sites. In this respect, by means of simulative studies, a positive and site dependent formation energy of an interstitial O_2 in silica was found in Ref. [144]. This energy value is referred to the unperturbed silica network and the isolated O_2 molecule, it is related to interaction between guest molecule and host matrix and it depends on the volume of hosting interstices. This study showed that for about 50% of sites the formation energy is lower than 0.5 eV but no interaction between occupied sites was accounted for determining these energy values. The absence of negative formation energy does not agree with experimental results that give a negative, even if small, value of $\widetilde{E}_a$ for the solubility, but the value of O_2 concentration found from the authors of Ref. [144] is in agreement with that measured. Probably, the presence of a small negative formation energy and the interaction between occupied sites were not relevant for the determination of the found equilibrium concentration because the authors were interested to its value at high temperature (1078 °C) and low concentration ($1.94 \cdot 10^{17}$ molecules cm^{-3}). By contrast, in the present work, temperatures are about one order of magnitude lower, concentration is about two orders of magnitude higher and departure from Langmuir model is observed at concentrations about two orders of magnitude higher than that of Ref. [144]. Under these experimental conditions, the interaction between occupied sites could be relevant, that is, the formation energy of an interstitial molecule could depend on the presence of other interstitial molecules nearby. In particular, the formation energy of two near interstitial O_2 could be higher than the sum of their separated formation energies. This aspect could qualitatively explain why the value of O_2 concentration is lower than that predicted by the Langmuir model and could also explain why the discrepancy diminishes on increasing the temperature. Indeed, if temperature is risen, higher energy configurations become probable.

Table 3.3: O_2 solubility in AEOX50 sample at various temperatures. Solubility values are the slopes of best fit straight lines in Fig. 3.7.

Temperature (°C)	Solubility (10^{18} molecules cm^{-3}/bar))
127	0.63±0.03
143	0.52±0.03
157	0.45±0.02
177	0.41±0.02
194	0.34±0.02
244	0.26±0.01

3.3 Conclusion

In this chapter, diffusion kinetics and equilibrium concentration of interstitial O_2 were studied as a function of temperature and pressure in AEOX50, fumed silica with average radius of primary particles equal to 20 nm. Diffusion kinetics were investigated

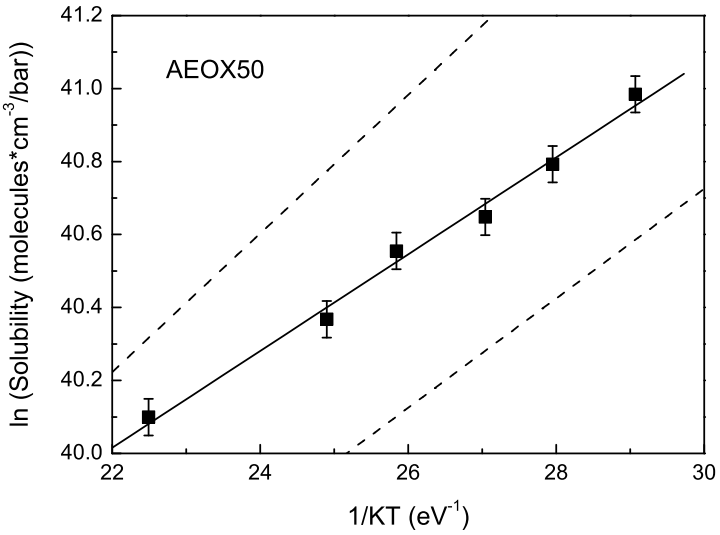

Figure 3.12: Arrhenius plot of O_2 solubility values reported in Table 3.3. Straight line is the best fit curve obtained by fitting experimental values with the Arrhenius law (eq. 1.43). Dashed lines are the extremals Arrhenius laws drawn by using the parameters from literature relative to experiments performed at temperatures above 500 °C and pressure lower than 3 bar in bulk silica [56].

by sorption and desorption experiments in the temperature range from 98 °C to 177 °C and O_2 external pressures 0.2 (air atmosphere), 6 and 66 bar. Desorption kinetics are slower than sorption ones. Sorption kinetics depend on external pressure being faster at higher pressure. Diffusion kinetics were found to be well described by the solution of Fick's diffusion equation in a sphere. By fitting experimental data with this equation an effective diffusion coefficient is obtained, that is based on some approximations concerning the boundary condition, size distribution and departure from spherical shape. In particular, particles were considered spheres having radius equal to the average radius of primary particles, and dissolution kinetics was considered to have an infinite rate. It was estimated that neglecting the size distribution leads to an underestimation of the diffusion coefficient less than a factor two, and that the effect related to departure from spherical shape, from a qualitative point of view, has the opposite effect.

Effective diffusion coefficients were found to depend on the external pressure and for each pressure value they follow Arrhenius laws with pressure dependent parameters in the investigated temperature range. The dependence on external pressure could be due to dependence of dissolution kinetics on external O_2 concentration or to a dependence of diffusion coefficient on concentration of diffusing O_2. Despite approximations, effective diffusion coefficients are within the range of values extrapolated from Arrhenius laws

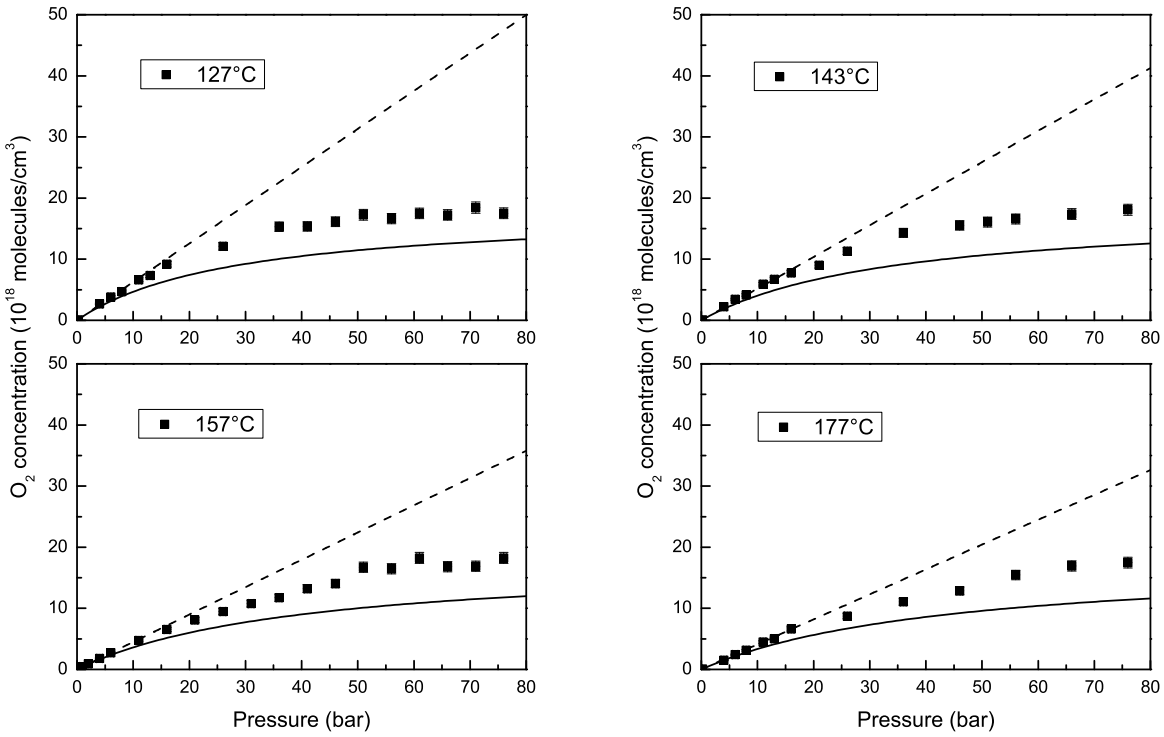

Figure 3.13: Comparison between O_2 equilibrium concentration values shown in Fig. 3.8 and Langmuir model (eq. 1.7). Solid lines are the Langmuir isotherms with solubility values reported in Table 3.3 and saturation concentration $1.8 \cdot 10^{19}$ molecules cm^{-3} (see Fig. 3.8) whereas dashed lines are the Langmuir isotherms with the same solubility values as the solid lines but saturation concentration $5.5 \cdot 10^{21}$ molecules cm^{-3}.

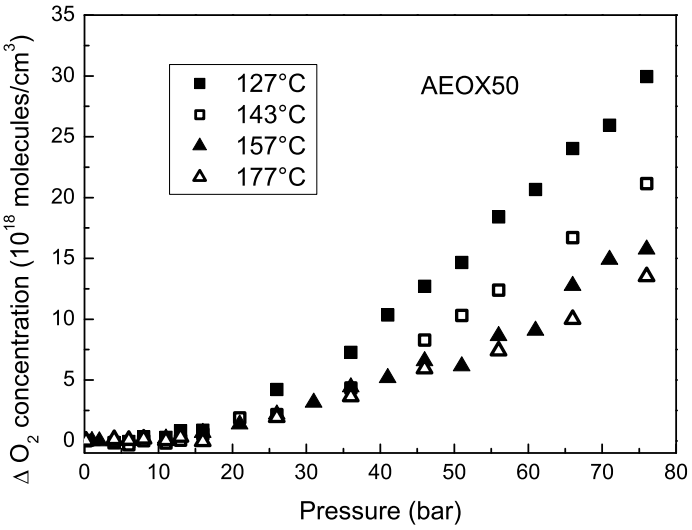

Figure 3.14: Differences between expected O_2 equilibrium concentration values predicted by Langmuir model (dashed lines) and experimental data shown in Fig. 3.13.

valid at higher temperature and lower pressure in the case of bulk silica.

Equilibrium O_2 concentration values were found to increase with pressure and decrease on increasing temperature below about 60 bar, whereas they are temperature and pressure independent at higher pressure in the investigated temperature range (127-177 °C). In particular, O_2 concentration increases linearly with pressure below 13 bar according to Henry's law in the temperature range from 127 °C to 244 °C. The found values of solubility in this temperature range change with temperature according to Arrhenius law and are in agrement with values extrapolated from Arrhenius laws valid in bulk silica at higher temperatures and lower pressures.

Departure from Henry's law and saturation of equilibrium concentration with pressure cannot be explained by the Langmuir model. O_2 concentration is less than predicted by this law and the difference decreases on increasing temperature. This behavior suggests that occupation states of near interstices could not be independent and the energy of the configuration in which two or more near interstices are occupied could be greater than the sum of energies of isolated occupied interstices.

In order to clarify the dependence of the diffusion kinetics and equilibrium concentration of O_2 on external pressure, experiments have to be performed on fumed silica with different particles size. Results of these experiments are shown and discussed in the next chapter.

Chapter 4

Size dependence of diffusion process in fumed silica

In the previous chapter, diffusion process of O_2 in and through AEOX50 was discussed. This sample is made up by nanoparticles whose average radius is 20 nm so results shown and discussed in chapter 3 only concern this particles size and do not contain information about the size dependence of diffusion process. In this chapter, experimental results concerning the diffusion process in fumed silica having primary nanoparticles with average radius smaller than 20 nm are shown, discussed and compared whit those of AEOX50. In particular, the investigation was performed on powders with nanoparticles of average radius down to 3.5 nm to investigate the features of diffusion when the volume of the host matrix becomes almost equal or smaller than the average volume occupied by a guest molecule. The study was also performed on powders whose size distributions are equal but having different surface morphologies in order to investigate the role played by this latter feature in diffusion process. Moreover, since particles having different size have different structural features, that can be changed by thermal treatments without affecting their size, diffusion experiments were performed on AE300 sample after treatment at 600 °C in air in order to separate the influence of size and structure on the diffusion process. The experimental study was done by desorption and sorption kinetics in the temperature range from 98 °C to 157 °C and pressures of 0.2 bar (desorption kinetics in air), 6 and 66 bar (sorption kinetics) in order to investigate the dynamics aspects. The dependence of the equilibrium concentration on temperature, pressure and particles size was also investigated by sorption experiments in the same temperature and pressure ranges.

4.1 Results

4.1.1 Desorption kinetics

Fig. 4.1 shows the Raman/PL spectra of as-received fumed silica samples whose average radius of primary nanoparticles ranges from 3.5 nm (AE380 and AE300 samples) to

20 nm (AEOX50). Both, Raman bands of silica matrix and the luminesce band of interstitial O_2 feature a size dependence. In particular, Raman band peaked at 440 cm^{-1} Raman shift moves toward higher energies and the intensity of D1 line increases when particles size is reduced [23, 22, 116]. The photoluminescence of interstitial O_2 decreases on increasing specific surface or reducing particles size.

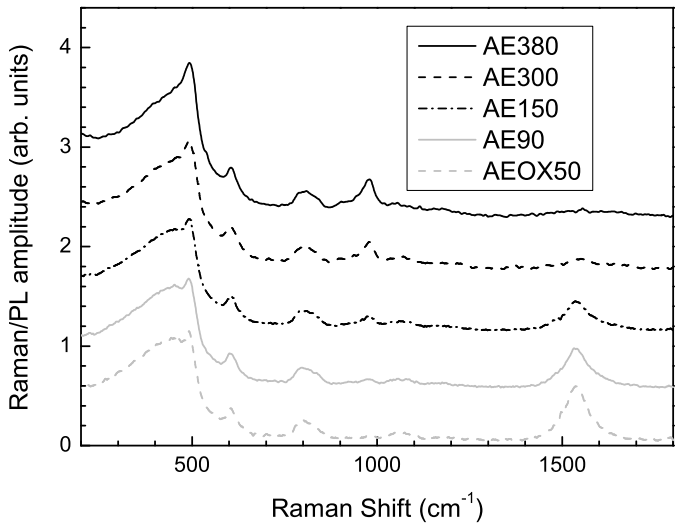

Figure 4.1: Raman/PL spectra of as-received fumed silica. Average radius of primary nanoparticles ranges from 3.5 nm (AE380 and AE300) up to 20 nm (AEOX50). Raman/PL spectra were normalized to have the same Raman scattering signal at 800 cm^{-1} and were arbitrarily vertically shifted for representation convenience.

Desorption kinetics of O_2 present in as-received samples AEOX50, AE90 and AE150 (average radius of primary nanoparticles 20, 10 and 7 nm, respectively) are shown in Fig. 4.2. These desorption kinetics were done in the temperature range from 98 °C to 157 °C. In general, desorption kinetics are faster at higher temperatures. Kinetics at 98 °C are reported either as a function of time or as a function of t/a^2 (a is the average radius of primary nanoparticles) in order to evaluate the effect of size on kinetics. Desorption kinetics relative to AE90 and AE150 samples are almost equal when plotted as a function of time and are different from the AEOX50 one. After the x-axis scale transformation, kinetics become similar. At the other temperatures, kinetics plotted as a function of t/a^2 tends to be faster in samples with smaller primary nanoparticles.

4.1.2 Sorption kinetics

Sorption kinetics in AE150 and AEOX50 samples (average radius of primary nanoparticles 7 and 20 nm, respectively) at 127 °C and 6 and 66 bar O_2 external pressure are shown in Fig. 4.3. Kinetics are shown both as a function of time or t/a^2 (a is the

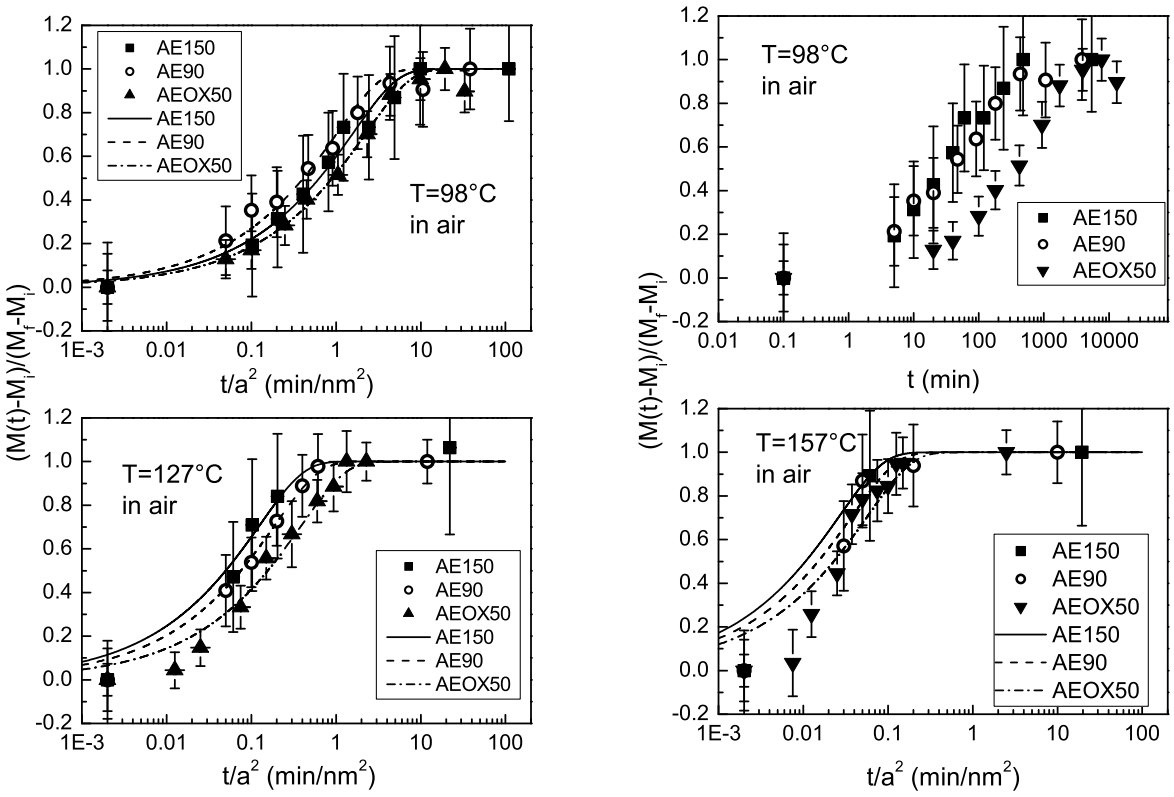

Figure 4.2: Desorption kinetics in AE150, AE90 and AEOX50 samples at various temperatures, as reported in graphs. Thermal treatments were carried out in air. M_i, M_f and M(t) are initial, final and at time t masses of interstitial O_2, respectively, and a is the average radius of primary nanoparticles (7, 10 and 20 nm for AE150, AE90 and AEOX50, respectively). Desorption kinetics at 98 °C are reported both as a function of t/a^2 and as a function of t. First points are relative to t=0. Lines are best fit curves obtained by fitting experimental data with eq. 2.15.

average radius of primary nanoparticles). As in the case of desorption kinetics, kinetics are very different when plotted as a function of t and become similar when the x-axis quantity is t/a^2. By contrast, the opposite behavior is observed for AE300 and AE150 samples (average radius of primary nanoparticles 3.5 and 7 nm, respectively) as can be seen in Fig. 4.4 where sorption kinetics at 98 °C and 6 and 66 bar are shown. Kinetics are equal within experimental errors if plotted in time domain whereas they are different if the x-axis scale is changed to t/a^2.

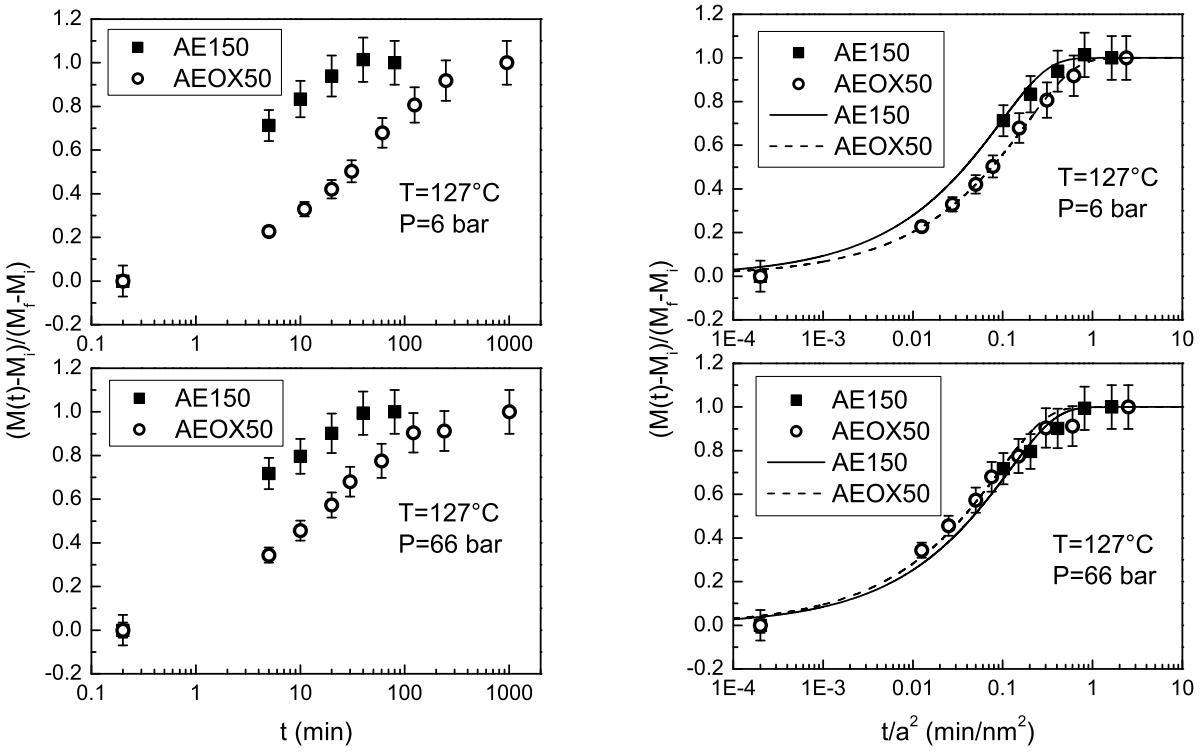

Figure 4.3: Sorption kinetics in AE150 and AEOX50 samples at 127 °C and two different pressures (6 bar and 66 bar), as reported in graphs. M_i, M_f and M(t) are initial, final and at time t masses of interstitial O_2, respectively, and a is the average radius of primary nanoparticles (7 and 20 nm for AE150 and AEOX50, respectively). Sorption kinetics are reported both as a function of t/a^2 and as a function of t. First points are relative to t=0. Lines are best fit curves obtained by fitting experimental data with eq. 2.15.

Sorption kinetics at 98 °C and 6 bar and 66 bar in AE380 and AE300 samples are plotted in Fig. 4.5 as a function of time. These samples have equal average radius but different surface morphology since the AE380 surface is rough. Diffusion kinetics reported in Fig. 4.5 are equal within experimental errors.

The dependence of the diffusion kinetics in AE150 sample on external pressure at investigated temperatures is shown in Fig. 4.6. As in the case of desorption kinetics,

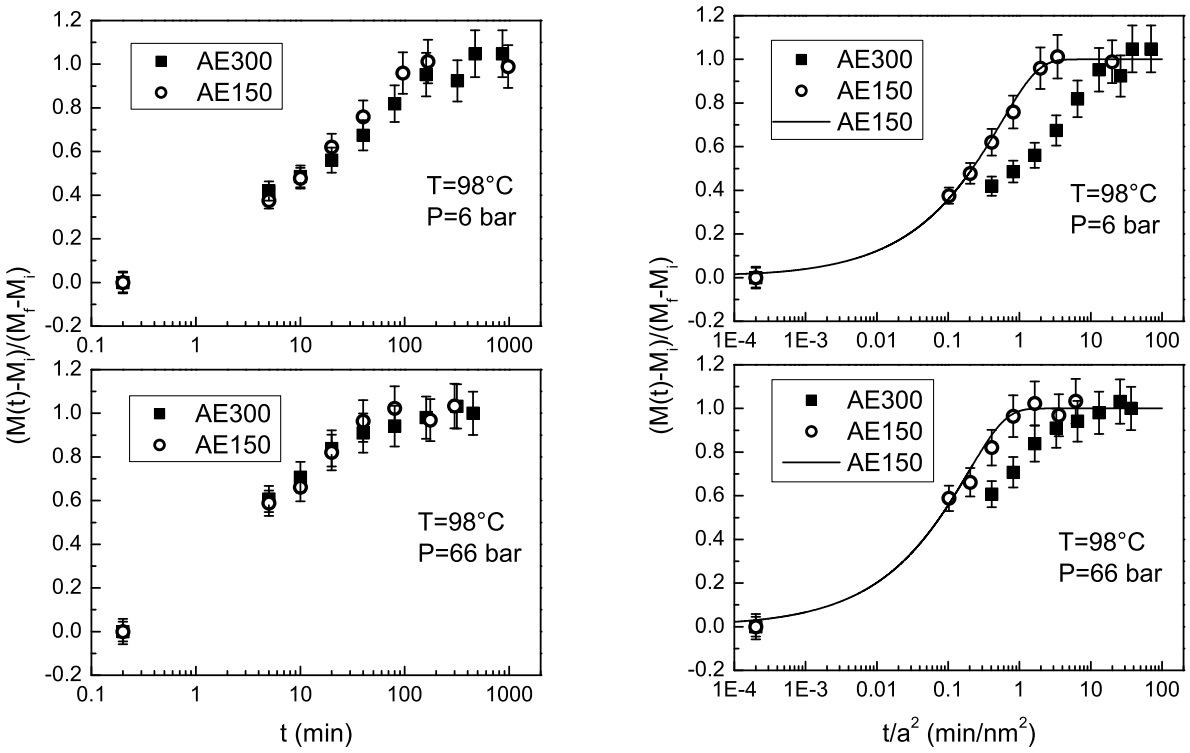

Figure 4.4: Sorption kinetics in AE300 and AE150 samples at 98 °C and two different pressures (6 bar and 66 bar) as reported in graphs. M_i, M_f and M(t) are initial, final and at time t masses of interstitial O_2, respectively, and a is the average radius of primary nanoparticles (3.5 and 7 nm for AE300 and AE150, respectively). Sorption kinetics are reported both as a function of t/a^2 and as a function of t. First points are relative to t=0. Lines are best fit curves obtained by fitting experimental data with eq. 2.15.

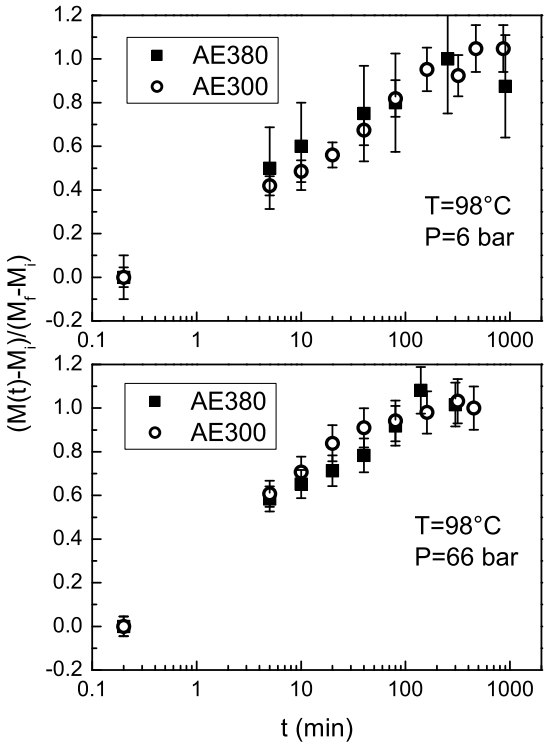

Figure 4.5: Sorption kinetics in AE380 and AE300 samples at 98 °C and two different pressures (6 bar and 66 bar) as reported in graphs. M_i, M_f and M(t) are initial, final and at time t masses of interstitial O_2, respectively. First points are relative to t=0.

sorption kinetics are faster at higher temperatures. Moreover, as shown and discussed in previous chapter for AEOX50 sample, diffusion kinetics depend on external pressure being faster at higher pressure and this dependence decreases on increasing temperature.

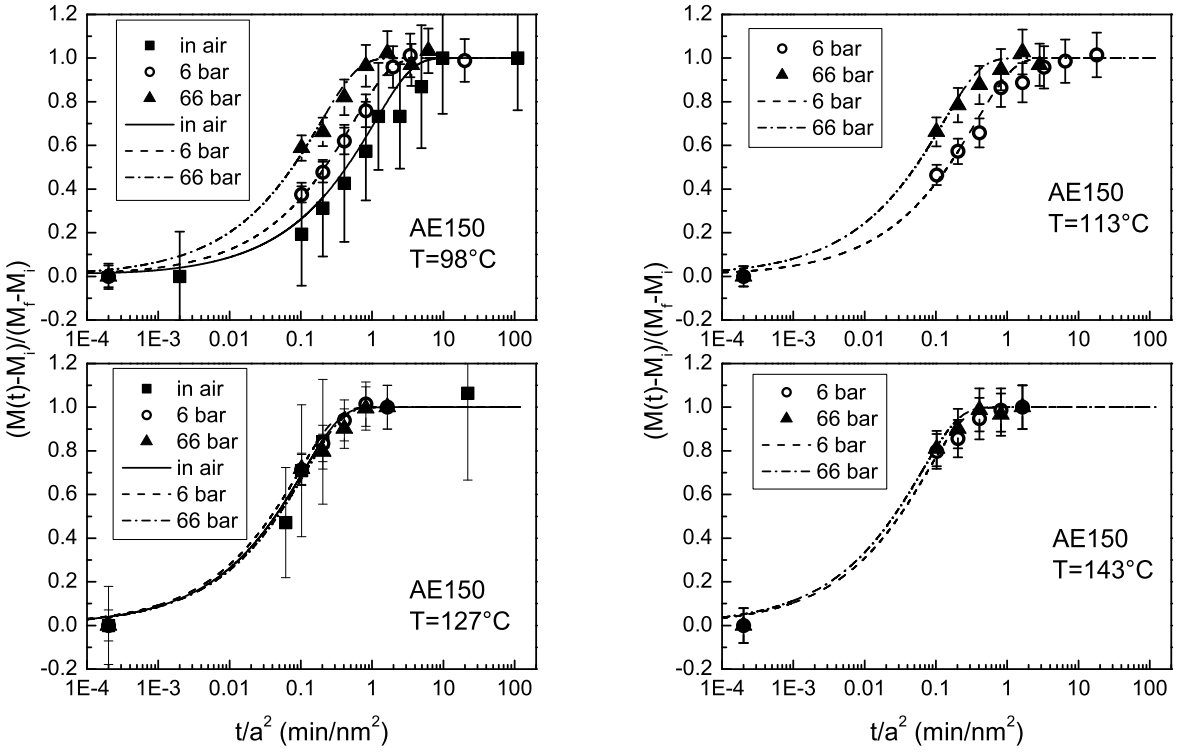

Figure 4.6: Diffusion kinetics in AE150 sample at investigated temperatures and pressures, as reported in graphs. "in air" refers to desorption kinetics of O_2 present in the as-received sample. M_i, M_f and M(t) are initial, final and at time t masses of interstitial O_2, respectively and a is the average radius of primary nanoparticles (7 nm). First points are relative to t=0. Lines are best fit curves obtained by fitting experimental data with eq. 2.15.

4.1.3 Equilibrium concentration

Equilibrium concentration values of interstitial O_2 in AE300 at two different temperatures, 98 and 127 °C in the pressure range from 6 to 76 bar are shown in Fig. 4.7. As in the case of AEOX50 sample, equilibrium concentration increases with external pressure at a given temperature and decreases on increasing temperature at a fixed pressure. Moreover, similarly to the AEOX50 case, equilibrium concentration does not increase linearly with pressure by following Henry's law in the whole investigated pressure range.

Equilibrium concentration depends not only on pressure and temperature but also on particles size as can be seen in Fig. 4.8 in which the pressure dependence of equilib-

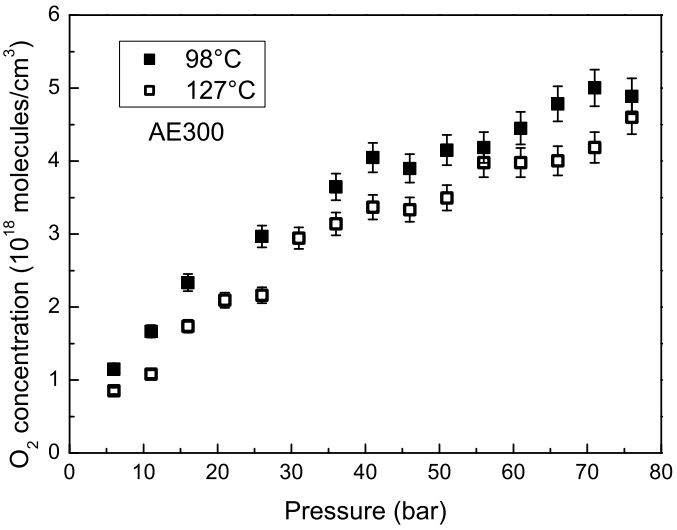

Figure 4.7: Equilibrium concentration of interstitial O_2 as a function of pressure in AE300 sample at 98 and 127 °C.

rium concentration in various samples is shown. In particular, data of figure are relative to AE300, AE150 and AEOX50 samples (average radius of primary nanoparticles 3.5, 7 and 20 nm, respectively) at 127 °C. Concentration of interstitial O_2 decreases on decreasing average radius of primary nanoparticles qualitatively in agreement with the finding relative to the O_2 concentration in as-received powders (see Fig. 4.1).

4.1.4 Effect of amorphous structure of nanoparticles on the diffusion process

As shown in the previous section, equilibrium concentration for given pressure and temperature depends on particles size. Since powders made up by particles with different size have different Raman spectra attributable to the core-shell structure, experiments have to be performed in order to understand if different O_2 content is related directly to particles size or to the network structure, which in turn depends on size. Since it is possible to change Raman spectra and matrix structure without affecting particles size by high temperature thermal treatments [127], the diffusion process was studied in the AE300 sample after thermal treatments in air at 600 °C for 2 h. Fig. 4.9 shows Raman spectra, normalized to Raman scattering signal at 800 cm^{-1}, of AE300 sample as-received and after 2 h thermal treatment in air. Spectra were normalized in this way due to the stability of 800 cm^{-1} bands under network modifications [147, 77]. After the treatment, the Raman band peaked at 440 cm^{-1} shifts toward lower energy and its intensity, as well as that of D1 band (peaked at 490 cm^{-1}), decreases. Moreover, the intensity of the band at about 980 cm^{-1}, related to silanol groups, decreases whereas

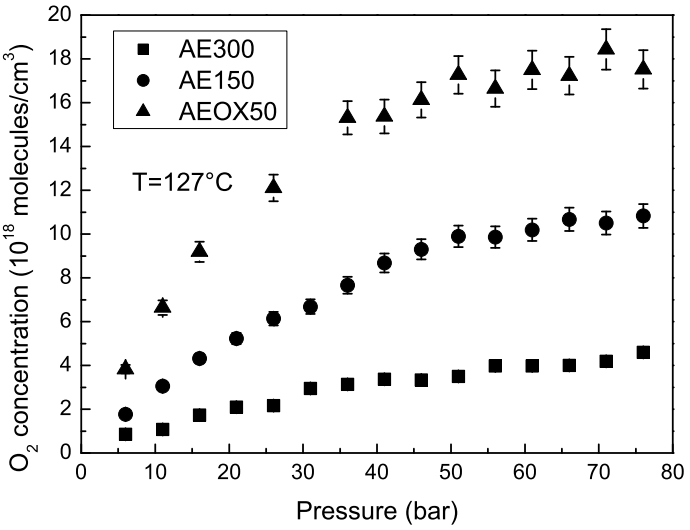

Figure 4.8: Equilibrium concentration of interstitial O_2 as a function of pressure in AEOX50, AE150 and AE300 samples at 127 °C.

that of D2 line increases. By comparing Raman spectra of thermal treated AE300 and that of as-received AEOX50 sample (see Fig. 4.9), it can be seen that they are similar in the region below 550 cm^{-1}. After the high temperature thermal treatment, the AE300 sample was put in O_2 atmosphere at 98 °C and 66 bar to perform a sorption kinetics. Experimental data relative to this sorption kinetics and that of untreated AE300 sample under the same thermodynamical conditions are shown in Fig. 4.10. Kinetics are equal within experimental errors. As for the diffusion kinetics, equilibrium concentration is independent on thermal treatments at 600 °C as can be seen by comparing O_2 PL bands in Fig. 4.11 relative to treated and as-received AE300 sample after a thermal treatment in O_2 at 98 °C and 75 bar.

4.2 Discussion

4.2.1 Equilibrium concentration

Equilibrium concentration values of interstitial O_2 in AE300 sample as a function of external pressure at two different temperatures, 98 and 127 °C are shown in Fig. 4.7. As for the case of the AEOX50 sample, the equilibrium concentration increases with pressure at a given temperature but not linearly. Furthermore, it decreases on increasing temperature at a fixed pressure according to finding of previous chapter in which a negative value of the activation energy in the Arrhenius law for solubility was found. Even if the qualitative behavior of the equilibrium concentration is equal in AE300 sample and AEOX50 sample, and the considerations done in the previous chapter can

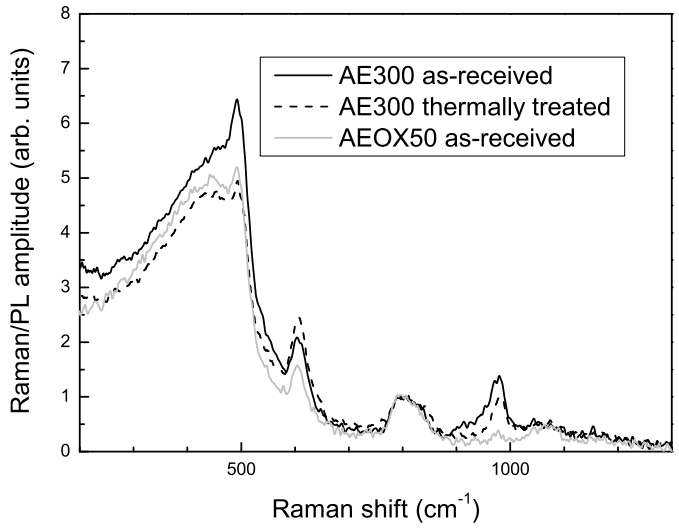

Figure 4.9: Raman/PL spectra of as-received and thermally treated AE300 samples. Thermal treatment was performed at 600 °C for 2 h in air. Raman/PL spectrum of as-received AEOX50 sample is also shown for comparison. Raman/PL spectra were normalized to have the same Raman scattering signal at 800 cm^{-1}.

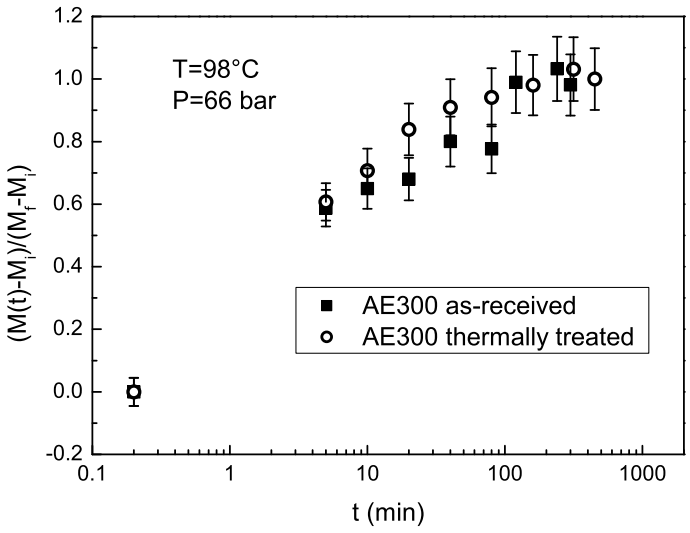

Figure 4.10: Sorption kinetics in as-received and thermally treated AE300 samples at 98 °C and 66 bar. Thermally treated AE300 sample was treated in air at 600 °C for 2 h before sorption experiment.

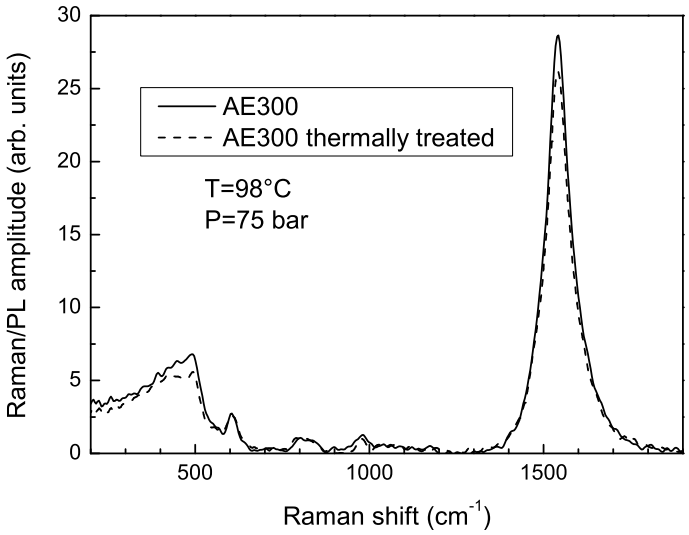

Figure 4.11: Raman/PL spectra of as-received AE300 sample treated in O_2 at 98 °C and 75 bar for 5 h and of AE300 sample thermally treated for 2 h at 600 °C in air then treated in O_2 at 98 °C and 75 bar for 5 h. Raman/PL spectra were normalized to have the same Raman scattering signal at 800 cm^{-1}.

be confirmed and extended, its value, under given thermodynamical conditions, is size dependent as can be seen in Fig. 4.8 in which the equilibrium concentration values at 127 °C as a function of external pressure are shown for AE300, AE150, AEOX50 (average radius of primary particles 3.5, 7 and 20 nm, respectively). Values relative to 66 bar for these three samples and that relative to the AE380 sample are reported in Fig. 4.12 as a function of the specific surface. This pressure has been chosen since it is representative of the maximum concentration in all the samples. Experimental data are a little bit scattered but can be linearly fitted as shown by the best fit line in the figure.

In order to explain this dependence, consider the grid drawn in Fig. 4.13 in which the squares represent silica interstices in a bulk solid. The dashed line schematizes the surface of a silica nanoparticle. As can be seen, the particle surface destroys a part of interstices near to the surface so the number of related cages per unit volume inside the nanoparticle is lower than in the case of bulk solid. This effect is size dependent, being negligible if the particle volume is much larger than the volume of a cage, but becomes relevant when the size of the particle is similar to the cage one.

In order to clarify the dependence of the O_2 concentration on the specific surface, in the following the effect sketched in Fig. 4.13 is modeled by supposing that there is a shell on the particles surface in which O_2 cannot be trapped [124]. If C_0 is the O_2 concentration in the inner part of the particle (particle without surface shell) whose

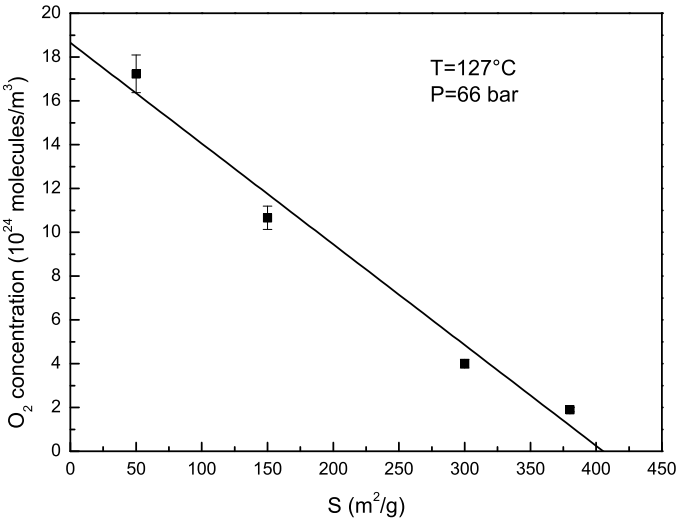

Figure 4.12: O_2 concentration at diffusive equilibrium at 127 °C and 66 bar as a function of specific surface. The line is the best fit straight line.

volume is V_0, the number N of molecules dissolved in it is

$$N = C_0 V_0 \tag{4.1}$$

By dividing both sides of eq. 4.1 by the total volume V of the particle, eq. 4.2 is obtained

$$C = C_0(1 - \frac{V_s}{V}) \tag{4.2}$$

where C is the concentration obtained by considering the total volume of the particle and $V_s = V - V_0$ in the volume of the surface shell in which O_2 cannot be trapped. By supposing, as a first approximation, $V_s = \delta\overline{S}$, where δ is the surface thickness and $\overline{S}$ is the surface of particle, eq. 4.2 can be put in the form of eq. 4.3

$$C = C_0(1 - \rho\delta S) \tag{4.3}$$

where $\rho = m/V$ is the density of the particle (m is its mass) and $S = \overline{S}/m$ is its specific surface. Eq. 4.3 predicts that the O_2 concentration decreases linearly with the specific surface. By supposing the investigated material to be made by identical particles and that the surface thickness is independent on the sample type, the intercept of the straight line in Fig. 4.12 is the O_2 concentration in bulk silica ($S = 0$) and the

slope is $-C_0\rho\delta$. Since the best fit straight line intercept and slope in Fig. 4.12 are about $18.7 \cdot 10^{24}$ molecules/m^3 and $-4.6 \cdot 10^{22}$ molecules g/m^5, the predicted thickness of the shell is about 1 nm, employing the density of bulk silica $2.2 \cdot 10^6$ g/m^3. This value is similar to that predicted on the basis of experimentally determined number of cages for unit volume, about $1.9 \cdot 10^{27}$ m^{-3} [27], since the average volume associated to each interstice is about 0.5 nm^3. Furthermore, the value of concentration in bulk system, the intercept of the straight line, is near to the one measured in the AEOX50 sample (see Figs. 4.12 and 4.8) so O_2 solubility and its Arrhenius parameters for these nanoparticles can be considered valid for bulk silica at low temperature.

Even if the above analysis suggests that a part of the dependence of O_2 equilibrium concentration on the size is due to surface effects, other effects related to the small size of the host system could also be present. Indeed, the above reasoning was made by considering a single particle and could not be valid when the average number of O_2 per particle is less than one, that is when the average volume of the particles is lower than the average volume occupied by a molecule in the bulk material, as occurs in the case of AE300 and AE380 samples. This aspect needs to be further explored, for example considering materials of fixed small size.

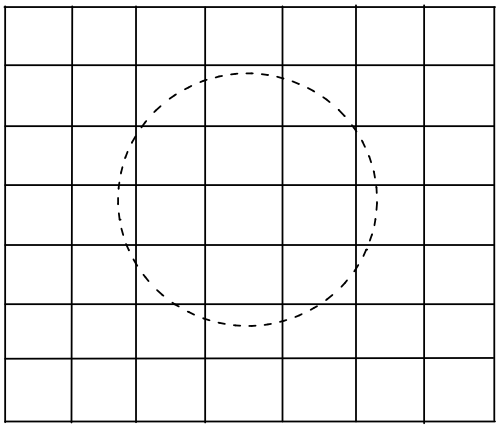

Figure 4.13: Grid schematically representing the silica network in a bulk solid. The lines are the walls of interstices in which O_2 molecules are trapped. Dashed line schematically represents the surface of a spherical silica nanoparticle.

4.2.2 Diffusion kinetics

Raman/PL spectra of fumed silica samples having different specific surface, and different average size of primary nanoparticles, are shown in Fig. 4.1. As discussed in sec. 1.6, the difference in the Raman bands can be related to the different structure of the nanoparticles and in particular, can be related to the core-shell model according

to which the core region has a structure equal to that of bulk silica whereas the shell surface is characterized by a ring statistics shifted toward smaller rings [116, 22, 20, 19]. Differences among Raman spectra in Fig. 4.1 are attributed to different ratios between the volumes of core region and surface shell since the latter is assumed of constant thickness independently on the nanoparticle size. In particular, the shell contribution with respect to the core one in Raman spectra is higher in smaller nanoparticles. In addition to the size dependence of the Raman bands, even the amplitude of the interstitial O_2 PL band depends on the particles size as reported in the previous paragraph. The amplitude of this band and hence the value of O_2 concentration in as-received samples decreases on decreasing the particles size or on increasing the specific surface. The decrease of O_2 PL amplitude restricts the set of samples available for studying desorption kinetics of O_2 in as-received samples so this study was confined to AE150, AE90 and AEOX50 having average radius 7, 10 and 20 nm, respectively.

Desorption kinetics at 98 °C of these samples are shown in Fig. 4.2 as a function of time. Kinetics is faster for smaller nanoparticles. Obviously, diffusion kinetics depends on shape and size of the medium in which diffusion occurs and these factors have to be taken into account to determine diffusion coefficients values. Since the solution of Fick's diffusion equation in a sphere (eq. 2.15) depends on t/a^2 (a is the radius of the sphere), the size effect can be removed by plotting the diffusion kinetics as a function of t/a^2. In the case of the investigated samples, in which particles are not perfect spheres and have different size, the spherical shape assumption was made and the size effect was removed as a first approximation by plotting the diffusion kinetics as a function of t/a^2 where a is the average radius of the primary nanoparticles. By comparing the two upper panels of Fig. 4.2, it can be seen that the diffusion kinetics of AEOX50 approaches the AE150 and AE90 ones after the x-axis quantity is changed from t to t/a^2 implying that the difference between these kinetics are mainly due to different size of the particles in which diffusion occurs. The size effect is lower in kinetics of AE90 and AE150 as can be seen by comparing kinetics in these samples before and after the x-axis is changed.

Small differences between the desorption in AEOX50, AE90 and AE150 samples, which can be seen by comparing kinetics shown in Figs. 4.2 or the effective diffusion coefficients collected in Table 4.1 and plotted in the Arrhenius graph of Fig. 4.15, could be due to several effects such as different degree of departure from spherical shape, different size distribution of primary nanoparticles and aggregates, different internal structure of nanoparticles or effect of dissolution kinetics. In particular, as shown in Fig. 4.15, effective diffusion coefficient in desorption kinetics tends to be higher in smaller nanoparticles when the average radius is reduced down to 7 nm (AE150).

In order to better understand the origin of these differences and in particular its possible relation with the size distribution of primary nanoparticles, desorption kinetics

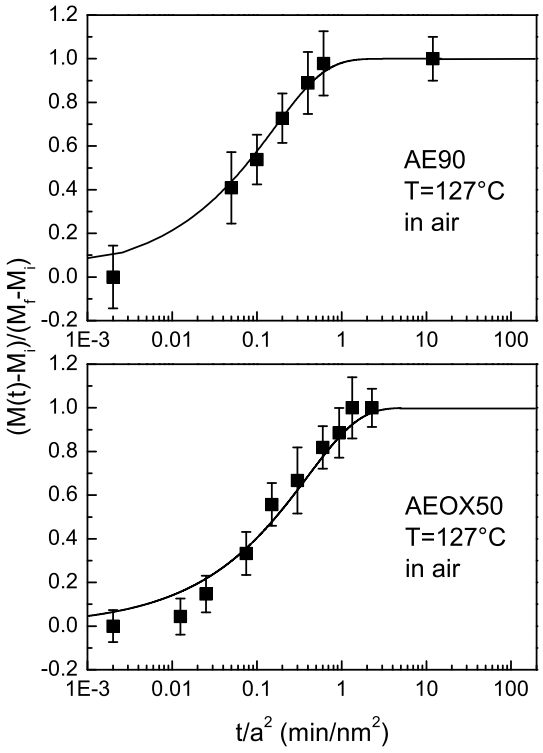

Figure 4.14: Desorption kinetics in AE90 and AEOX50 samples (average radius of primary nanoparticles 10 and 20 nm, respectively) at 127 °C. Solid lines are best fit curves obtained by fitting the experimental data with eq. 3.4 to take into account the size distribution of primary nanoparticles.

in AE90 and AEOX50 samples (average radius of primary nanoparticles 10 and 20 nm, respectively) were fitted by the function reported in eq. 3.4 that takes into account the size distribution of primary nanoparticles [130]. The best fit curves are reported in Fig. 4.14. The values of effective diffusion coefficients are 0.6 ± 0.3 and 0.3 ± 0.1 nm^2/min for AE90 and AEOX50, respectively. By comparing these values with those estimated by neglecting the size distribution effect, 0.4 ± 0.2 and 0.18 ± 0.06 nm^2/min for AE90 and AEOX50, respectively, it can be seen that the effective diffusion coefficients are about doubled for both samples when the effect of size distribution is taken into account and the differences are still present between the two samples. On these basis the differences between diffusion kinetics are not only due to size distribution of primary nanoparticles. Moreover, eq. 3.4 does not take into account the dependence of the concentration of interstitial O_2 on particles size since it was determined by supposing the concentration to be size independent (see section 3.2.1).

Since O_2 average concentration increases on increasing particles size, as can be seen in Fig. 4.8, the weight of bigger particles with respect to smaller ones in eq. 3.4 should be greater than it is actually. This feature should lead to an underestimation of the effective diffusion coefficient and this underestimation should be greater in samples with smaller value of average radius and it would increase the difference between the values found by eq. 3.4 relative to different samples. This consideration strengthens the impossibility to explain the difference between diffusion kinetics by means of size distribution effect.

As said, another source of the difference between diffusion kinetics could be the different internal structure of nanoparticles that depends on particles size, as can be seen by the Raman spectra shown in Fig. 4.1. In order to investigate the role played by this factor, sorption diffusion kinetics were performed in as-received AE300 sample and after the sample was treated in air at 600 °C for 2 h. The Raman spectrum of the sample after this thermal treatment is shown in Fig. 4.9 and, for comparison, also the Raman spectra of the as-received AE300 sample and the AEOX50 are reported. After thermal treatment, the Raman band peaked at about 440 cm^{-1} moves toward lower energy and the intensity of D1 band (peaked at 490 cm^{-1}) decreases [116, 22]. After the thermal treatment, the Raman spectrum of AE300 sample approaches that of AEOX50 one as can be seen by comparing their spectra in Fig. 4.9 below about 550 cm^{-1}, whereas the difference in the spectral region of D2 line is due to formation of three-membered rings on nanoparticles surface as a result of the condensation of vicinal silanol groups [119]. Indeed, the increase of the D2 band is accompanied by the decrease of the Raman band at 980 cm^{-1} due to silanol group mainly placed on nanoparticles surface [124]. Moreover, AFM measurements (not reported) showed that nanoparticles size is not affected by such a thermal treatment so this latter enables to change the internal nanoparticles structure without changing the morphological features [124]. Sorption

kinetics in the as-received AE300 sample and in the thermally treated one are shown in the Fig. 4.10. They are similar within experimental errors so it can be stated that the different internal structure does not affect the diffusion kinetics in AE300 sample. Basing on this finding, the differences between the diffusion kinetics in the different samples are not related to internal particles structure.

A further phenomenon affecting the diffusion kinetics is the surface dissolution when they have the same time scale. Since the diffusion time in a sphere is proportional to its square radius, the dissolution process affects mainly the diffusion kinetics in smaller nanoparticles by producing an underestimation of the effective diffusion coefficient. Indeed this latter is greater in smaller nanoparticles, if it is found by neglecting the dissolution effect. For this reason the difference between estimated effective diffusion coefficients in nanoparticles of different radii cannot be explained by dissolution effect.

Small differences between desorption kinetics have not been explained by the above considered effects however, other effects not treated here because of their difficulties, could affect diffusion kinetics. These effects could be related to distortions from the spherical shape and to the presence of aggregates and their distribution size that has not been taken into account due to lack of information about them. Finally, the presence of preferential pathways in smaller particles, such as predicted in thin oxide layer on silicon film, cannot be excluded [144].

For what concerns sorption kinetics in smaller nanoparticles, the applicability of Fick's theory to experimental data has to be discussed. In section 3.2.1, the applicability of Fick equation was justified even at low concentration since measurements are made on a great number of nanoparticles, however, that demonstration fails when the number of dissolved molecules per particle is too low. That reasoning assumed the following pictorial behavior of molecules: molecules dissolved in particles, then diffused inwards and, successively, other molecules enter the particle and so on until equilibrium is reached. By measuring the time evolution of the mass of interstitial O_2, entangled information about dissolution process and diffusion one can be gained.

In order to understand the limits of the reasoning made in sec. 3.2.1, consider the limit case in which only a molecule per nanoparticles is dissolved at the equilibrium state. In this case, since the measured quantity is the mass of dissolved molecules, the measurement gives information only about the dissolution kinetics and no information about diffusion through nanoparticles, because the equilibrium value of interstitial O_2 is reached just when the molecule enters the particle. The above argumentation suggests that this effect is not present only in the considered limit case but affects every sorption kinetics because the measurement is characterized by a lack of information about the last part of the diffusion kinetics, concerning the diffusion through the particles of the last molecules entering in it. In this context, the utilized measurement procedure reduces the experimental measured diffusion time and this reduction is greater in systems

with high specific surface, or equivalently small size, due to the higher ratio between the number of molecules dissolved near the surface and the total one. In particular, in the case of the AE150, assuming the radius equal to the average one (7 nm), the number of molecules per particles at equilibrium varies between 3 and 18 when the pressure is in the range between 6 and 66 bar. In the case of the higher number of molecules, the average distance between them is about 4 nm meaning that all molecules are in a surface layer, so for AE150 sample the sorption kinetics is essentially a dissolution kinetics. In this picture, the effective diffusion coefficient found from AE150 sorption kinetics is meaningless and the ratio D/a^2, where a is the average radius of primary particles, should be considered as a measure of dissolution rate. Moreover, sorption kinetics in AE300 and AE150 samples (average radius of primary nanoparticles 3.5 and 7 nm, respectively) are equal if plotted in time domain whereas are different when the x-axis is changed to take into account the size effect (see Fig. 4.4). This independency of sorption kinetics on particle size suggests that the investigated process is probably the dissolution one. Under this assumption, the equality between diffusion kinetics in AE300 and AE380 (see Fig. 4.5) indicates that the dissolution process does not depend on surface morphology since AE300 and AE380 have the same particles size but different specific surface, due to the roughness of AE380 surface.

Table 4.1: Effective diffusion coefficients in nm^2/min determined by fitting the experimental desorption kinetics shown in Fig. 4.2 with eq. 2.15. The best fit curves are the lines drawn in Fig. 4.2.

Sample	98°C	127°C	157°C
AE150	0.07 ± 0.05	0.7 ± 0.5	3 ± 2
AE90	0.08 ± 0.04	0.4 ± 0.2	2 ± 1
AEOX50	0.04 ± 0.02	0.18 ± 0.06	1.3 ± 0.4

Due to equality of diffusion kinetics in powders with primary particles having average radius less than 7 nm, AE150 sample will be considered as representative of all these samples so only the behavior of its kinetics at different temperatures and pressures will be discussed. Values of effective diffusion coefficient for this sample at the investigated temperatures and pressures are reported in Table 4.2 and plotted in the Arrhenius form in Fig. 4.16. It is worth noting that the values reported in Table 4.2 are not true diffusion coefficient values of O_2 in silica but parameters related to the rate of dissolution in silica. As in the case of the AEOX50, discussed in the previous chapter, diffusion kinetics are faster at higher temperatures but by contrast, the dependence on external pressure, that is qualitatively equal to that of AEOX50, disappears at temperature above about 127 °C whereas in the AEOX50 case tends to disappear above 177 °C. This behavior could clarify if the pressure effect is related to the dependence of the diffusion coefficient on concentration or that of the dissolution rate

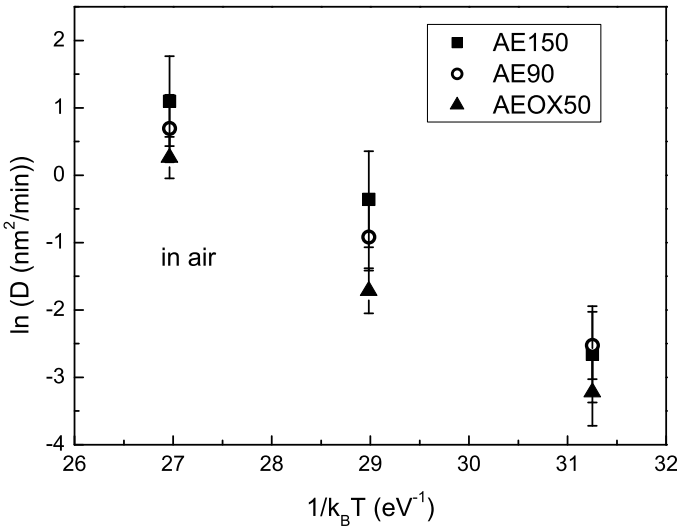

Figure 4.15: Arrhenius plot of effective diffusion coefficients collected in Table 4.1. The values are relative to desorption kinetics in AE150, AE90 and AEOX50 samples (average radius of primary nanoparticles 7, 10 and 20 nm, respectively) in the temperature range from 98 °C to 157 °C.

on external pressure. By supposing the kinetics in AE150 as dissolution kinetics, part of the dependence of diffusion kinetics in AEOX50 on the external pressure should be related also to dissolution. On the other hand, since the overall process timescale in AE150 is about one order of magnitude lower than in AEOX50 (see Fig. 4.3), and in the former the dissolution process could be dominant, probably diffusion kinetics in the latter are weakly affected by dissolution kinetics so the pressure dependence of the AEOX50 kinetics suggests a dependence of the diffusion coefficient on concentration of diffusing substance. This hypothesis is supported by the different temperature behavior of the effective diffusion coefficient in AE150 and AEOX50. Indeed, the pressure effect disappears at lower temperature in AE150 sample suggesting that the dependence is mainly related to different physical quantities in these two samples, dissolution rate in AE150 and diffusion coefficient in AEOX50.

4.3 Conclusion

In this chapter, features of the diffusion process in fumed silica made up by primary particles having average radius down to 3.5 nm were investigated. The dependence of equilibrium value of interstitial O_2 on temperature and pressure are qualitatively equal to that observed in AEOX50 sample but absolute values are different. In particular, they depend on specific surface, being smaller in samples with higher specific surface.

Table 4.2: Diffusion coefficients in nm^2/min determined by fitting experimental sorption kinetics in AE150 sample (average radius of primary nanoparticles equal to 7 nm) with Eq. 2.15. Experimental data, that are relative to external pressures 6 and 66 bar in the temperature range from 98 °C to 143 °C, are reported in Fig. 4.6 together with best fit curves.

Temperature (°C)	6 bar	66 bar
98	0.14 ± 0.03	0.4 ± 0.1
113	0.21 ± 0.05	0.60 ± 0.15
127	0.8 ± 0.3	0.65 ± 0.15
143	1.0 ± 0.4	1.2 ± 0.4

A part of this dependence was related to the presence of "broken" interstices not able to trap O_2 molecules near the particles surface, but effects related to small size of particles could also be present. Indeed, particles volume is comparable to or less than the average volume occupied by a molecule in bulk silica.

Desorption of interstitial O_2 present in as-received samples was investigated in AE150, AE90 and AEOX50 (average radius of primary particles 7, 10 and 20 nm, respectively). Kinetics are faster in smaller particles. The greatest part of this difference is related to longer distance that molecules have to travel in bigger particles and can be taken into account, as a first approximation, considering powders made up by identical spherical particles having radius equal to the average one of primary particles. After these corrections, residual small differences among kinetics in different samples are present. These small differences cannot be related to size distribution of primary particles but could be due to the presence of aggregates and to the departure from spherical shape that are hard to estimate due to lack of information about them. An additional source of observed differences could be the presence of preferential pathways related to small size of medium in which diffusion occurs.

Sorption experiments were performed on the sample with average radius of primary particles equal to 3.5 nm in addition to fumed silica investigated in desorption experiments. Sorption kinetics were found to be equal independently on the size in samples with average radius less than 7 nm. This effect is related to the small size of particles and to the procedure of measurement that make sorption kinetics equal to dissolution one. Sorption kinetics showed that dissolution kinetics depends on external pressure, being faster at higher pressure as in the case of sorption kinetics in AEOX50 discussed in the previous chapter. This finding suggests that a part of the pressure dependence observed in diffusion kinetics in AEOX50 could be related to diffusion kinetics. However, since the dissolution time scale is about one order of magnitude minor than the diffusion time scale in AEOX50, a contribution to pressure dependence could be also related to a concentration dependent diffusion coefficient. This hypothesis is also supported by the different temperature behavior of the dependence of the effec-

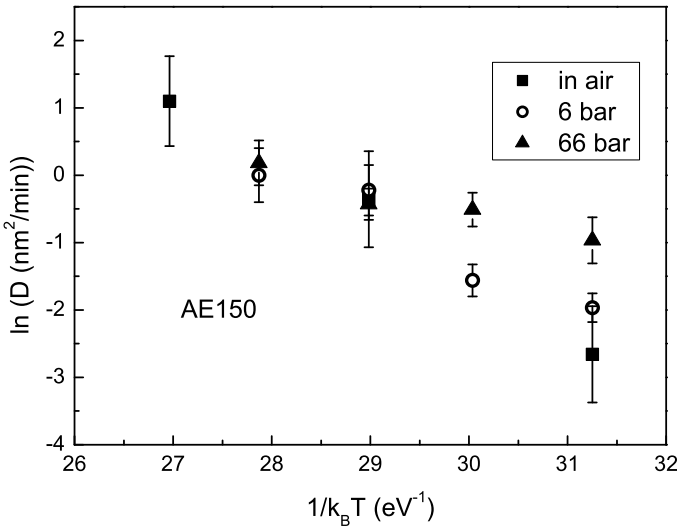

Figure 4.16: Arrhenius plot of the effective diffusion coefficients relative to diffusion kinetics in the AE150 sample (average radius of primary nanoparticles equal to 7 nm) obtained by fitting experimental data reported in Fig. 4.6 with eq. 2.15. "in air" refers to desorption kinetics. Relative best fit curves are the lines drawn in Fig. 4.6.

tive diffusion coefficient on pressure in AEOX50 with respect to that of the rate of dissolution measured in smaller particles.

Chapter 5

Dependence of diffusion process on surface chemistry in fumed silica

In the previous chapter, size dependence of diffusion process on morphological aspects such as particles size and surface morphology was discussed. In this chapter, the features of diffusion process in fumed silica with modified chemistry surface will be discussed and compared in fumed silica particles having same size but different surface chemistry.

5.1 Results

Fig. 5.1 shows Raman/PL spectra of as-received R816 and AE200 samples having average radius of primary particles equal to 6 nm (see Table 2.1). Raman bands of silica and that of silanol group (peaked at 980 cm^{-1}) are present in the spectrum of AE200 whereas additional Raman bands peaked at 1086, 1300, 1440 and 2900 cm^{-1} can be observed in the spectrum of R816 (bands marked by arrows). The amplitude of Raman band related to silanol groups is higher in AE200 sample. PL band of interstitial O_2 is present in both samples and is slightly higher in R816 sample.

Fig. 5.2 shows the changes of R816 Raman/PL spectrum under thermal treatments in air at 200 or 300 °C for 5 min. By comparing post-treatments Raman/PL spectra with the as-received one (also shown in Fig. 5.2) it can be seen that Raman bands related to silica and that of silanol groups are unaffected by thermal treatments whereas the other Raman bands are modified by thermal treatment at 300 °C but not by the treatment at 200 °C. PL band of interstitial O_2 is reduced in both thermal treatments. Raman bands at 1086, 1300, 1440 and 2900 cm^{-1} are also stable under treatment at 127 °C in O_2 atmosphere at 6 bar following the treatment in air at 200 °C for 5 min, as can be seen by comparing Raman/PL spectra, shown in Fig. 5.3, of as-received and thermally treated R816 sample. The only difference between these spectra is

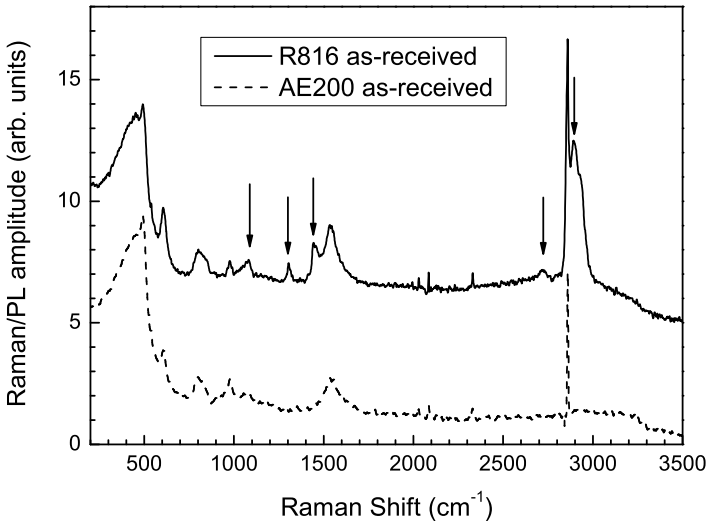

Figure 5.1: Raman/PL spectra of as-received R816 and AE200 samples (average radius of primary particles equal to 6 nm). Arrows highlight Raman bands due to hydrophobic surface groups. Spectra were normalized to have equal Raman scattering signal at 800 cm^{-1}.

the amplitude of interstitial O_2 PL band that is higher in the sample treated in O_2 atmosphere.

Sorption kinetics at 127 °C and 6 bar after treatment of R816 sample is shown in Fig. 5.4. This kinetics was made after a thermal annealing of 5 min in air at 200 °C in order to outgas O_2 present in the as-received sample. Sorption kinetics of AE200, having same average radius of primary particles than R816, and AE150 (average radius of primary particles 7 nm) are also shown for comparison. Sorption kinetics of AE200 sample was performed after annealing in air for 5 min at 200 °C as in the case of R816 sample whereas sorption kinetics in AE150 was performed after standard thermal annealing in air of 5 min at 300 °C. No significant differences between the samples is found.

Equilibrium concentration of interstitial O_2 as a function of pressure at 127 °C is shown in Fig. 5.5 for R816, AE200 and AE150 samples. Equilibrium values in R816 are higher than in AE200 but lower than in AE150. In addition to absolute values, even the pressure dependence is different as can be seen by comparing data relative to reported samples in the region between 35 and 55 bar. It is worth noting that concentration in R816 was worked out by using the decay time of AE200 since that of R816 is unknown.

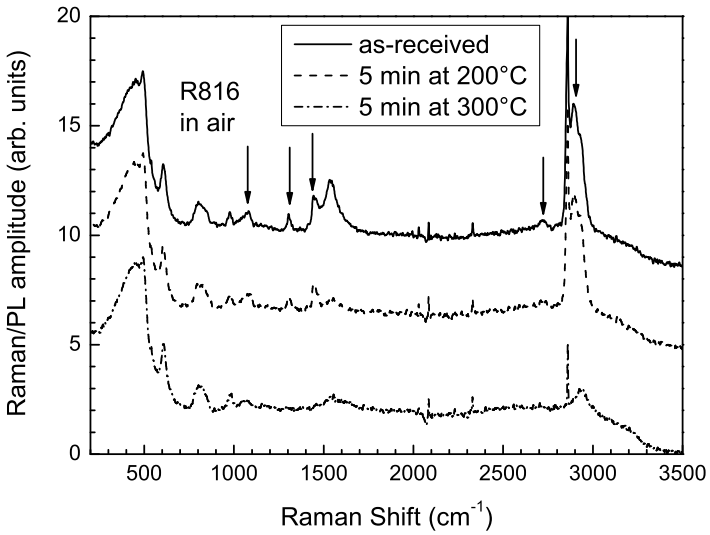

Figure 5.2: Raman/PL spectra of as-received and thermally treated R816 (average radius of primary particles equal to 6 nm). Thermal treatments were performed in air at 200 or 300 °C for 5 min. Arrows highlight Raman bands due to hydrophobic surface groups. Spectra were normalized to have equal Raman scattering signal at 800 cm^{-1}.

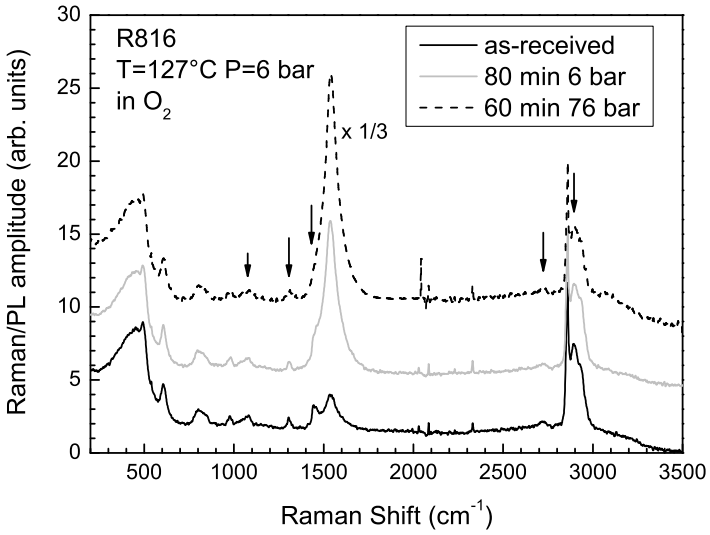

Figure 5.3: Raman/PL spectra of as-received and thermally treated R816 sample (average radius of primary particles equal to 6 nm). Thermal treatments were performed in O_2 atmosphere at 127 °C and 6 bar for 80 min or 76 bar for 60 min. The region between 1380 and 1810 cm^{-1} of the spectrum relative to thermal treatment at 76 bar was multiplied by a factor 1/3 for clarity. Arrows mark Raman bands due to hydrophobic surface groups. Spectra were normalized to have equal Raman scattering signal at 800 cm^{-1}.

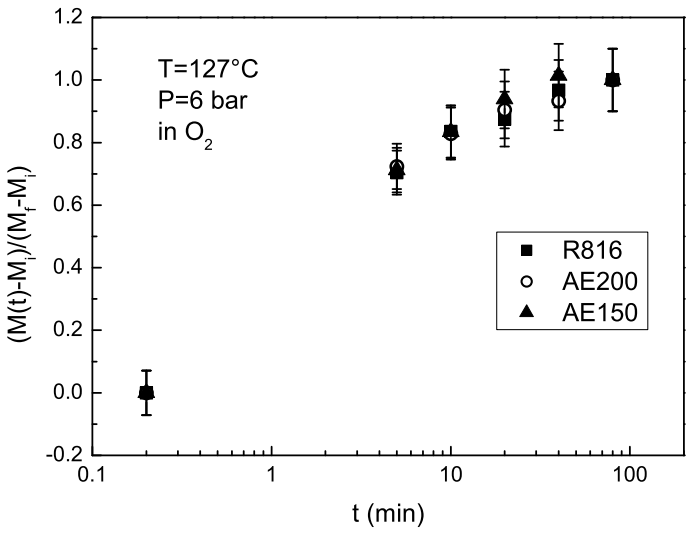

Figure 5.4: Sorption diffusion kinetics in R816, AE200 and AE150 samples (average radius of primary particles equal to 6, 6 and 7 nm, respectively) at 127 °C and 6 bar.

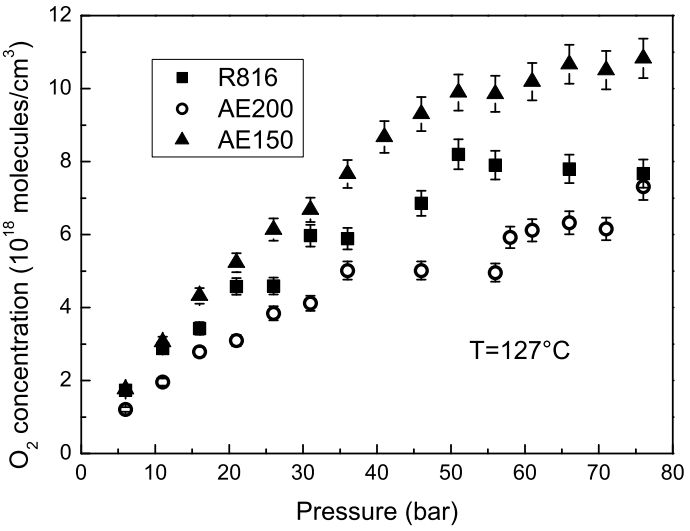

Figure 5.5: Equilibrium concentration of interstitial O_2 as a function of pressure in R816, AE200 and AE150 samples (average radius of primary particles equal to 6, 6 and 7 nm, respectively) at 127 °C.

5.2 Discussion

R816 sample is produced by Evonik industries using as start material AE200 powder. In particular, R816 is obtained by substitution of silanol surface groups with hydrophobic ones. From a morphological point of view, AE200 and R816 are equal. Both samples have 200 m^2/g specific surface and average radius of primary particles equal to 6 nm so the only difference is the surface chemistry (see Table 2.1). The comparison between Raman/PL spectra of these two samples, reported in Fig. 5.1, reveals differences. R816 spectrum features Raman bands, at 1086, 1300, 1440 and 2900 cm^{-1}, that are not present in the AE200 one. These bands are due to Raman active vibrational modes of organic compounds on R816 surface substituting hydrophilic silanol groups. Silanol groups are not completely removed, as indicated by the presence of silanol Raman band at 980 cm^{-1} in the Raman/PL spectrum of R816. However, this band has a minor amplitude in R816 than in AE200 due to partial substitution of surface silanol groups in R816. In addition to these differences, the amplitude of interstitial O_2 PL band is different in the two samples. In particular, the ratio between PL amplitude of interstitial O_2 and that of Raman band peaked at 800 cm^{-1} is greater in R816 (Raman spectra were normalized to have same Raman scattering amplitude at 800 cm^{-1}). Since Raman band at 800 cm^{-1} is proportional to mass of sample investigated by Raman/PL measurements, it can be asserted that O_2 luminescence per unit mass in as-received samples is higher in R816 sample. This does not mean that O_2 concentration is higher in R816 because luminescence quantum yield could be different in the two samples.

In previous chapters, kinetics study of hydrophilic fumed silica was performed on samples annealed for 5 min at 300 °C in air before sorption kinetics in order to outgas interstitial O_2 present in as-received materials. This procedure is not applicable to hydrophobic fumed silica such as R816 due to instability of organic groups under thermal treatments at 300 °C as can be seen in Fig. 5.2. Indeed, by comparing Raman/PL spectra of R816 as-received and after thermal treatment at 300 °C, it can be seen that the amplitude of Raman bands peaked at 1086, 1300, 1440 and 2900 cm^{-1} is lower in the treated sample. The decrease is related to destruction of hydrophobic surface groups so this procedure has not to be followed since diffusion kinetics in hydrophobic sample must be investigated. On the other hand, the annealing in air at 200 °C does not affect the hydrophobicity of sample whereas induces O_2 desorption, as can be seen in Fig. 5.2. For these reasons, diffusion study on R816 was performed after 5 min annealing in air at 200 °C. Even diffusion study on AE200 was done after the same annealing since it was performed in order to compare diffusion features in AE200 and in R816, and compare particles having same morphological properties but different surface chemistry. Moreover, hydrophobicity of samples has not to be affected by the presence of O_2 in the atmosphere in which sorption kinetics is performed.

Raman/PL spectra shown in Fig. 5.3 are relative to treatments in O_2 atmosphere

at 127 °C and 6 and 76 bar for 80 and 60 min, respectively, after the annealing in air at 200 °C for 5 min. Treatment times are sufficient to diffusive equilibrium be reached so they are the longest treatment times. Moreover, 76 bar is the highest investigated pressure. By comparing Raman/PL spectra in Fig. 5.3 of treated and as-received samples, it can be seen that there is no difference in Raman bands of hydrophobic groups after treatment at 6 bar and only a decrease of about 30% of the amplitude of Raman band at 2900 cm^{-1} after the treatment at 76 bar, that is under the worst conditions. This finding ensures diffusion study was performed without affecting the sample hydrophobicity significantly.

Sorption kinetics at 127 °C and 6 bar external O_2 pressure in R816 is shown in Fig. 5.4 and for comparison those relative to AE150 and AE200 are also shown. As discussed in the previous chapter, sorption kinetics in samples with particles smaller than AE150 ones are mainly dissolution kinetics and are independent on particles size. Comparison between sorption kinetics relative to AE150 and AE200 samples confirms this finding. Moreover, diffusion kinetics in AE150 was performed after annealing in air at 300 °C whereas AE200 was annealed at 200 °C. The equality between the kinetics shows that these two different experimental procedures do not affect diffusion kinetics, as expected, since the annealing in air does not change particles features at these low temperatures. Sorption kinetics of R816 is equal to AE200 one (see Fig. 5.4) meaning that dissolution kinetics is independent on surface chemistry at least under the investigated degree of substitution of silanol groups.

The pressure dependence of equilibrium concentration of R816 at 127 °C is shown in Fig. 5.5 together with equilibrium values relative to AE200 and AE150 samples. As observed for the content of interstitial O_2 present in as-received samples, equilibrium values in R816 are higher than in AE200. It is worth noting that values relative to R816 could be affected by a systematic error because lifetime of observed O_2 PL transition is unknown. In the previous chapter, equilibrium concentration was found to depend on particles size and to be independent on particles structure and on density of surface silanol groups, at least for the variation induced on AE300 sample treated in air at 600 °C for 2 h. This finding indicates that O_2 concentration and its PL lifetime are independent on content of surface silanol in the explored range of silanol concentration. Since the decrease of silanol Raman band (peaked at 980 cm^{-1}) in AE300 thermally treated at high temperature is higher than the difference between the amplitude of silanol bands in R816 and AE200 samples, the difference in O_2 PL band cannot be related to different silanol concentrations. Furthermore, if the difference were related to different lifetimes, pressure dependence should be equal within a constant factor whereas data sets shown in Fig. 5.5 have different shape. Then, the difference between luminescence bands could be related to different O_2 sample concentration. In particular, the difference could be related to the presence of hydrophobic groups on surface. Indeed,

in a sample with high specific surface, the Helmholtz free energy related to surface could not be negligible and it could be important in order to determine equilibrium conditions. The interaction between O_2 in gas phase and hydrophobic groups on particles surface could affect equilibrium concentration value. Another contribution could be related to structural effects of surface groups on the surface morphology. For example, the presence of this groups could diminish the number of broken cages near the surface that cannot trap O_2.

5.3 Conclusion

Diffusion process was investigated on fumed silica samples having same morphological features but different surface chemistry in order to study the role of surface chemistry. In particular, investigated samples, R816 and AE200, have average radius of primary particles equal to 6 nm, 200 m^2/g specific surface, but silanol groups on R816 surface have been partially substituted with organic groups giving it a hydrophobic behavior. Investigation was performed at 127 °C in the pressure range from 6 up to 76 bar. Diffusion kinetics into particles are equal whereas equilibrium concentration values are higher in R816. Moreover, values have a different dependence on pressure. This effect cannot be related to a minor surface coverage of silanol groups since it was not observed in a sample, discussed in the previous chapter, in which a greater difference in silanol coverage was induced. On the other hand, the difference can be related to a contribution due to interaction between organic groups and O_2 in gas phase that could be relevant to determine the chemical potential, due to the high specific surface, and hence the equilibrium value of interstitial O_2. A further contribution could be related to possible increase of the number of interstices near to the surface able to trap O_2 due to possible morphological changes of surface after silanol groups substitution.

Chapter 6

Diffusion process in silica particles produced by microemulsion method

In previous chapters, properties of the diffusion process in fumed silica were discussed. Fumed silica, produced by pyrogenic technique, is not the only type of nanosized silica. A different way to produce silica nanoparticles is the microemulsion method. This procedure, described in sec. 2.1, gives particles with morphological features different with respect to fumed silica ones. For example, microemulsion particles usually have sharp size distributions and this characteristics makes them suitable for specific applications. On the other hand, this aspect is very interesting in order to study the diffusion process in a "homogeneous" system, that is made up by almost identical components, in which the size distribution effect becomes almost negligible. As explained in sec. 2.4, diffusion process in microemulsion samples was not performed from a kinetic point of view but only equilibrium values were investigated. Experiments were carried out at 200 °C and 50 bar or 400 °C and 90 bar on samples with average particles diameter equal to 25, 60 and 120 nm with two different surface chemistries, hydrophilic and hydrophobic.

6.1 Results

Fig. 6.1 shows Raman/PL spectra of microemulsion samples with average nanoparticles diameter equal to 25 nm and two different surface chemistries, hydrophilic (named 25nm, panel a) and hydrophobic (named 25NH_2, panel b). Raman/PL spectra of the samples are relative to as-grown materials and to materials thermally treated in O_2 atmosphere at 200 °C and 50 bar for different times as reported in the legend of the figure. For comparison, the Raman/PL spectra of as-received and thermally treated fumed silica sample AE90 (average diameter of primary particles 20 nm) is also reported (panel c of the figure). The presence of Raman bands unrelated to silica can be seen by comparing Raman/PL spectra of as-grown microemulsion samples and that

of the AE90 one. In particular, Raman/PL spectra of microemulsion samples feature bands in the spectral regions below 1700 cm^{-1} and from 2700 to 3000 cm^{-1} that are not present in the spectrum of AE90. A further difference between spectra of microemulsion samples and fumed silica one is the presence of PL band of interstitial O_2, peaked at 1538 cm^{-1}. It can be seen in AE90 whereas it is absent in microemulsion samples. After thermal treatments in O_2 atmosphere, Raman/PL spectra of microemulsion samples evolve towards that of pure silica. The amplitude of Raman bands unrelated to vibrational mode of pure silica decreases but differences with respect to pure silica spectra can be observed by comparing Raman/PL spectra of microemulsion samples after thermal treatments and the AE90 one. Raman/PL spectra of 25nm and 25nmNH_2 are characterized by the absence of D2 band (at 605 cm^{-1}) and for the residual presence of impurities Raman bands at 980 cm^{-1}, related to silanol groups, and in the spectral region 2700-3000 cm^{-1}. Moreover, the PL band of interstitial O_2 is absent in the spectra of microemulsion samples thermally treated in O_2 atmosphere. By contrast, Raman/PL spectra of AE90 sample are not modified by thermal treatments except for the increase of interstitial O_2 PL band.

Raman/PL spectra of as-grown 25nm sample and after thermal treatments in He and O_2 are shown in Fig. 6.2. The sample was first thermally treated at 400 °C and 90 bar in He, then at 200 °C and 50 bar in O_2 atmosphere. Thermal treatment in He modifies the Raman spectrum of the sample. Raman bands unrelated to pure silica vibrational modes disappears except for the band of silanol groups (at 980 cm^{-1}), and Raman bands of silica are modified as can be seen by the presence of D2 line (605 cm^{-1}) in the Raman/PL spectrum of the treated sample. The following thermal treatment in O_2 does not modify Raman bands of the sample and induces the PL band of interstitial O_2.

Fig. 6.3 shows Raman/PL spectra of microemulsion samples of different size (average diameters equal to 25, 60 and 120 nm) both hydrophilic (named 25nm, 60nm and 120 nm) and hydrophobic (named 25nmNH_2, 60nmNH_2 and 120 nmNH_2). Raman/PL spectra are relative to as-grown and thermally treated samples. After thermal treatment at 400 °C and 90 bar in O_2, Raman/spectra of all samples become similar to that of pure silica except for the band at 980 cm^{-1} related to silanol groups and the luminescence band of interstitial O_2 peaked at 1538 cm^{-1}.

Fig. 6.4 shows Raman/PL spectra of AEOX50 sample (fumed silica with average diameter of primary particles 40 nm) both loaded with O_2 at 400 °C and 90 bar and functionalized with APTES after loading. Raman/PL spectrum of functionalized AEOX50 is different than before functionalization. In particular, Raman bands peaked at 1315 and 2900 cm^{-1} and the shoulder at 1450 cm^{-1} (highlighted by arrows in figure) appear in the spectrum of the functionalized sample. In addition to these bands, changes in the spectral region form 700 to 1100 cm^{-1} can also be seen by comparing

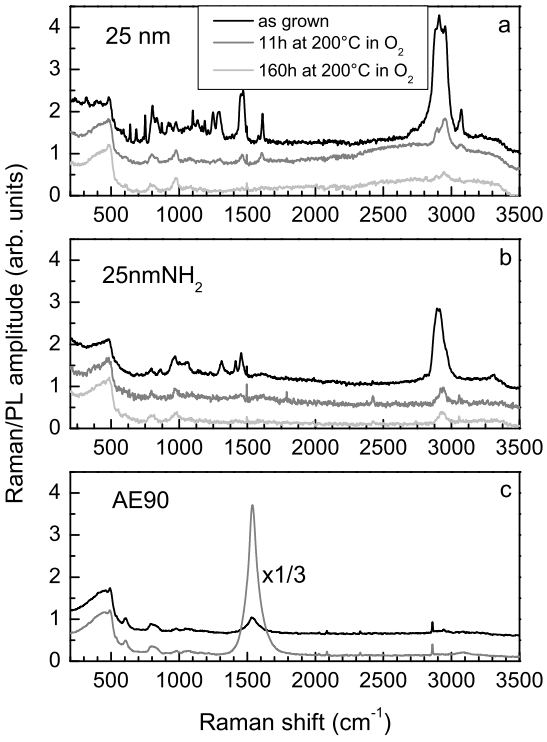

Figure 6.1: Raman/PL spectra of hydrophilic (25nm, panel a) and hydrophobic (25nmNH_2, panel b) microemulsion samples having average particles diameter 25 nm. Spectra are relative to as-grown samples and after thermal treatments of different duration at 200 °C and 50 bar in O_2 atmosphere. Raman/PL spectra of AE90 sample as-received and thermally treated in O_2 are also shown for comparison (panel c). Raman/PL spectrum of AE90 in the spectral region between 1300 and 1800 cm^{-1} has been multiplied by a factor 1/3 for clarity.

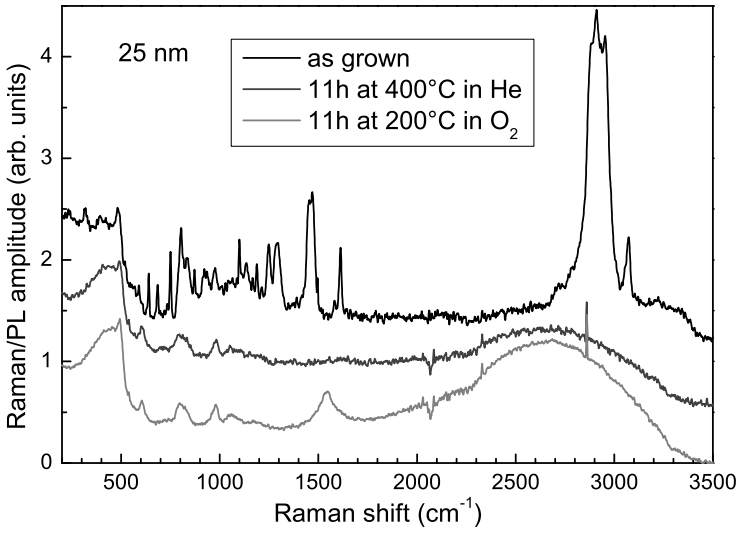

Figure 6.2: Raman/PL spectra of hydrophilic microemulsion sample having average particles diameter equal to 25 nm. Raman/PL spectra are relative to as-grown sample and to sample treated in He at 90 bar first, then in O_2 atmosphere at 50 bar for 11h.

the spectra shown in Fig. 6.4. It is worth noting that the PL band of interstitial O_2 is not affected by surface functionalization.

6.2 Discussion

The comparison between Raman/PL spectra of microemulsion samples and fumed silica shown in Fig. 6.1 reveals the presence of Raman bands unrelated to vibrational modes of pure silica in the spectral regions below 1700 cm^{-1} and from 2700 to 3000 cm^{-1}. These bands are present either in hydrophilic or in hydrophobic samples (panel a and b of Fig. 6.1, respectively) even if their amplitude in the latter one is lower. Moreover, these bands are present even in samples with bigger particles as can be seen in Fig. 6.3. They are probably due to residual presence of starting materials and could be either on surface particles or inside them as molecules trapped during the growing process of particles. These impurities bands are unstable under thermal treatments at 200 °C and 50 bar in O_2 atmosphere as can be seen by comparing Raman/PL spectra of 25nm and 25nmNH_2 before and after such thermal treatments, as reported in panels a and b of Fig. 6.1. The decrease of the amplitude of impurities Raman bands is higher after longer thermal treatments but, even after the 160 h lasting treatment, they are not completely removed as indicated by the presence of Raman bands in the spectral region from 2700 to 3000 cm^{-1}. After thermal treatment, there are other differences in addition to the presence of residual impurities related to starting materials, as can be

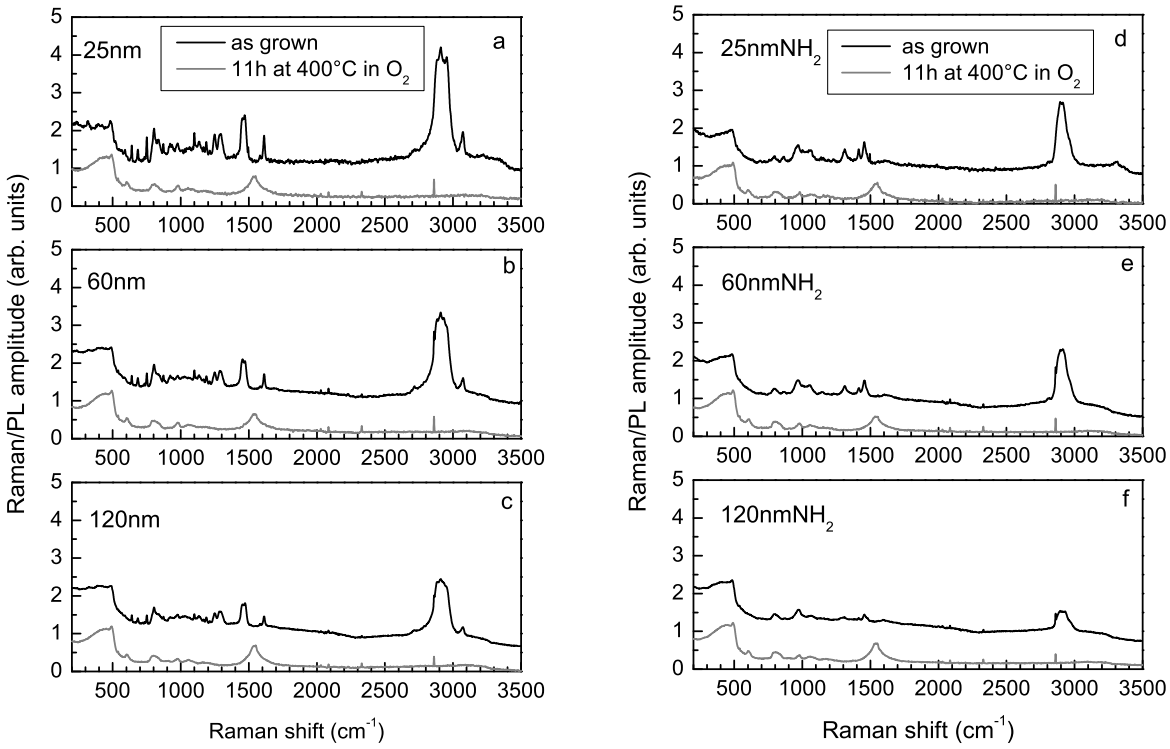

Figure 6.3: Raman/PL spectra of as-grown microemulsion samples and thermally treated at 400 °C and 90 bar in O_2 for 11h. Spectra in panel a, b and c are relative to hydrophilic samples with average particles diameter equal to 25, 60 and 120 nm, respectively. Spectra in panel d, e and f are relative to hydrophobic samples with average particles diameter equal to 25, 60 and 120 nm, respectively.

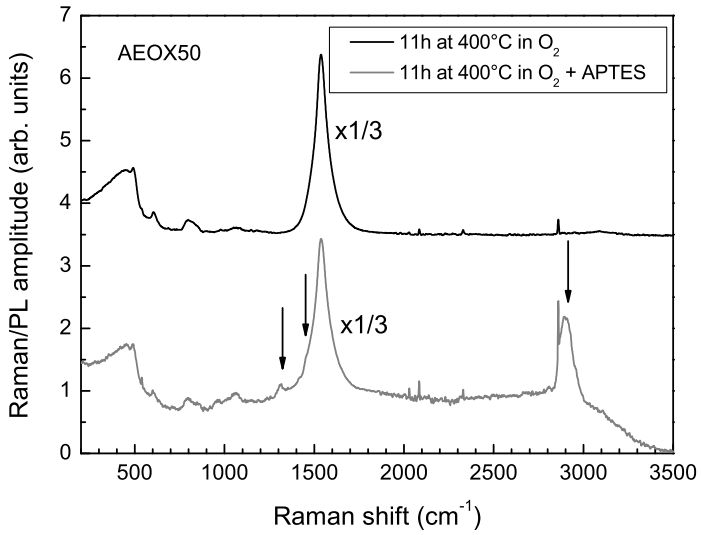

Figure 6.4: Raman/PL spectra of AEOX50 sample (fumed silica with average particles diameter 40 nm) thermally treated in O_2 at 400 °C and 90 bar for 11 h and after following functionalization with APTES. Raman/PL spectrum in the spectral region between 1300 and 1800 cm^{-1} has been multiplied by a factor 1/3 for clarity.

seen by comparing Raman/PL spectra of microemulsion samples and AE90 one after the 160 h lasting thermal treatment in O_2 (see spectra reported in Fig. 6.1). In particular, silanol Raman band, at 980 cm^{-1}, is higher in microemulsion samples and there are also differences among the bands related to silica vibrational modes as can be seen, for example, from the absence of the D2 line at about 600 cm^{-1} in microemulsion samples. Since silanol groups in silica particles are mainly placed on surface and their density is almost constant, the greater amplitude of their Raman band in microemulsion samples is probably due to a higher value of specific surface in these samples with respect to AE90 one. Furthermore, since average radius of AE90 particles is 20 nm, near that of microemulsion samples, the difference of silanol content could be due to an internal porosity of microemulsion samples that increases their specific surface. Finally, whereas the thermal treatment at 200 °C induces the O_2 PL band in AE90, no luminescence band of interstitial O_2 is observed in Raman/PL spectra of microemulsion samples.

The removal of impurities and the structural changes of silica network can also be obtained by thermal treatments in inert atmosphere of He at 400 °C as can can be seen in Fig. 6.2. Unlike the treatment in O_2 at 200 °C, the He treatments relax the network of microemulsion particles towards that of fumed silica more efficiently as indicated by the presence of the D2 line in the Raman/PL spectrum shown in Fig. 6.2. This effect is related to the higher temperature of thermal treatments since the same effect can be achieved by means of a thermal treatment in O_2 atmosphere at 400 °C, see Fig. 6.3.

After the thermal treatment at 400 °C in inert atmosphere, the subsequent treatment in O_2 at 200 °C induces the PL band of interstitial O_2 as can be seen by the presence of the band peaked at 1538 cm^{-1} in the spectrum shown in Fig. 6.2. The induction of this PL band can also be obtained by a single thermal treatment at 400 °C in O_2 atmosphere, see Fig. 6.3. Furthermore, as can be seen in Fig. 6.3, this effect is almost independent on particles size.

The absence of O_2 PL band in microemulsion samples before the thermal treatment at 400 °C could be related to different factors as low luminescence efficiency or low solubility. Indeed, the transition related to this PL band is forbidden for unperturbed O_2 molecule and its probability is strongly dependent on its surrounding. In this frame, the appearance of this PL band should be related to variation of luminescence efficiency related to changes of surrounding silica network. In this respect, it is worth noting that diffusion experiments performed on AE300 with modified network (see sec. 4.1.4) showed that the amplitude of O_2 PL band in silica is unaffected by network modifications. However, network modifications in microemulsion samples are more relevant than in the AE300 case, so the above mentioned effect could take place.

For what concerns the solubility, a dependence of solubility on specific surface in fumed silica was found in chapter 4. As above written, the amplitude of Raman band of silanol groups suggests a specific surface greater than expected for 25 nm sized particles. This could be due to the presence of internal porosity that would increase the specific surface. In this context, the appearance of O_2 PL band could be due to reduction of internal porosity at 400 °C and the minor content of interstitial O_2 in microemulsion samples with respect to AE90 should be due to higher value of specific surface in microemulsion particles because of their internal porosity. This porosity is also suggested by TEM measurements (see Ref. [148]). Even the independency of O_2 content on particles size (see Fig. 6.3) could be explained by internal porosity. In chapter 4, O_2 content was found to depend on particles size and specific surface since the specific surface is strictly related to particles size in non-porous particles. In porous particles, specific surface value depends both on particles size and internal porosity so the independence of O_2 content on particles size could be explained by supposing that the greater contribution to specific surface in this nanoparticles is related to internal porosity and that the degree of porosity is size independent.

Thermal treatments necessary to obtain microemulsion particles with interstitial O_2 destroy the surface functionalization as can be seen by the absence of Raman bands related to hydrophobic groups in Raman/PL spectra reported in Figs. 6.2 and 6.3. In order to have functionalized microemulsion particles with NIR emission, due to interstitial O_2, samples should be re-functionalized after O_2 loading. Surface functionalized and NIR emitting silica nanoparticles can also be obtained by loading fumed silica with interstitial O_2 and then functionalizing the loaded particles. Raman/PL spectra

in Fig. 6.4 are relative to O_2 loaded AEOX50 (fumed silica with average diameter of primary particles equal to 40 nm) before and after surface functionalization with APTES. In the spectrum of functionalized sample, there are Raman bands peaked at 1315 and 2900 cm^{-1} and a shoulder at 1450 cm^{-1} (marked by arrows in Fig. 6.3) related to functionalization groups after the substitution of silanol groups with APTES. The functionalization procedure does not affect the amplitude of PL band of interstitial O_2. It is worth noting that this particles have a NIR emission higher than microemulsion ones.

6.3 Conclusion

Equilibrium concentration of interstitial O_2 was studied in silica nanoparticles produced by microemulsion method. The investigation was performed on particles having average diameter 25, 60 and 120 nm and two different surface chemistries, hydrophilic (with silanol surface groups) and hydrophobic (with NH_2 groups on their surface). For comparison, same experiments were performed on AE90, fumed silica with similar size (average diameter of primary particles equal to 20 nm).

Raman/PL spectra of microemulsion samples feature Raman bands related to impurities, probably due to residual starting materials, that can be removed by thermal treatments either in O_2 or inert atmosphere. Moreover, unlike AE90, Raman/PL spectra of as-grown microemulsion samples do not contain the PL band of interstitial O_2 and it is not induced by a thermal treatment in O_2 at 200 °C. A further difference between fumed silica and that produced by microemulsion is that in the latter Raman bands of silica are modified under thermal treatments at 400°C. After these modifications, the PL band of interstitial O_2 is induced by treating the sample in O_2 atmosphere at 200 °C but its amplitude is much lower than in AE90 and almost independent on particles size. This behavior was related to internal porosity of microemulsion samples, evidenced by high silanol concentration and TEM images. In particular, internal porosity is reduced by the treatment at 400 °C and the equality among O_2 PL amplitude in samples with different size suggests that the internal porosity is size independent.

Chapter 7

Conclusions

In this thesis, the influence of thermodynamic parameters and nanoparticles properties on the diffusion kinetics and equilibrium concentration of O_2 in silica nanoparticles was investigated. The diffusion experiments were carried out in the temperature range from 98 °C to 244 °C and in the pressure range from 0.2 bar up to 76 bar range not yet explored and of interest both for applications and for extension of physics knowledge. Diffusion was studied in fumed silica with average radius of primary particles ranging from 20 nm down to 3.5 nm and for different surface morphologies. Furthermore, the influence of surface chemistry on the diffusion process was investigated by performing experiments on hydrophobic and hydrophilic fumed silica. The influence of the synthesis process on diffusion was investigated by comparing the experimental results relative to fumed silica and those of particles synthesized by microemulsion method.

Diffusion kinetics of O_2 in AEOX50, fumed silica with 20 nm average radius of primary particles, were investigated by sorption and desorption experiments at three different O_2 external pressures 0.2 (air atmosphere), 6 and 66 bar. Desorption kinetics are slower than sorption ones and sorption kinetics depend on external pressure being faster at higher pressure. Diffusion kinetics were found to be well described by the solution of Fick's diffusion equation in a sphere but only an effective diffusion coefficient is obtained by fitting experimental data with this equation due to some approximations concerning the boundary conditions, size distribution and departure from spherical shape. The effective diffusion coefficients were found to depend on the external pressure and for each pressure value they follow Arrhenius laws with pressure dependent parameters in the investigated temperature range. Despite approximations, effective diffusion coefficients are within the range of values extrapolated from Arrhenius laws valid at higher temperature and lower pressure in the case of bulk silica.

For what concerns smaller nanoparticles, desorption of interstitial O_2 present in as-received samples was investigated in AE150, AE90 and AEOX50 (average radius of primary particles 7, 10 and 20 nm, respectively). Kinetics are faster in smaller particles and the greatest part of this difference is related to longer distance that molecules have

to travel in bigger particles and can be taken into account, as a first approximation, considering powders made up by identical spherical particles having radius equal to the average one of primary particles. However, after these corrections, residual small differences among kinetics in different samples are present. These small differences cannot be related to size distribution of primary particles but could be due to the presence of aggregates and to the departure from spherical shape that are hard to estimate due to lack of information about them. Furthermore, an additional source of observed differences could be attributed to the presence of preferential pathways related to small size of medium in which diffusion occurs.

Sorption experiments were performed even on the sample with average radius of primary particles equal to 3.5 nm in addition to fumed silica investigated in desorption experiments. Sorption kinetics were found to be equal independently on the size in samples with average radius less than 7 nm, and this effect is related to the small size of particles and to the procedure of measurement that make sorption kinetics equal to dissolution one (the latter being related only to the entrance of the molecules through the nanoparticle surface). This kinetics showed that dissolution depends on external pressure, being faster at higher pressure. This finding suggests that a part of the pressure dependence observed in effective diffusion coefficient in AEOX50 could be related to dissolution kinetics. However, since the dissolution time scale is about one order of magnitude minor than the diffusion time scale in AEOX50, a contribution to pressure dependence could be also related to a concentration dependent diffusion coefficient. For what concerns the influence of the surface properties on diffusion kinetics, no dependence was found on the surface morphology and chemistry.

Equilibrium O_2 concentration values were found to increase with pressure and decrease on increasing temperature for pressure below 60 bar, whereas they are temperature and pressure independent at higher pressure in the investigated temperature range. In particular, O_2 concentration increases linearly with pressure below 13 bar according to Henry's law. The found values of solubility in AEOX50 change with temperature according to Arrhenius law and are in agreement with values extrapolated from Arrhenius laws valid in bulk silica at higher temperatures and lower pressures. The departure from Henry's law and saturation of equilibrium concentration with pressure cannot be explained by the Langmuir model. In particular, the O_2 concentration is less than predicted by this law and the difference decreases on increasing temperature suggesting that occupation of near interstices sites involves interaction and the energy of the configuration in which two or more near interstices are occupied could be greater than the sum of energies of isolated occupied interstices. For what concerns equilibrium values in smaller nanoparticles, the dependence on temperature and pressure is qualitatively equal to that observed in AEOX50 sample but absolute values are different. In particular, they depend on specific surface, being smaller in samples with higher specific

surface. A part of this dependence was related to the presence of broken interstices not able to trap O_2 molecules near the particles surface, but effects related to small size of particles could be also present. Indeed, particles volume is comparable to or less than the average volume occupied by a molecule in bulk silica.

Whereas diffusion kinetics are independent on chemistry surface, equilibrium concentration values are higher in hydrophobic nanoparticles and feature a different dependence on pressure. This difference can be related to a contribution due to interaction between organic groups and O_2 in gas phase that could be relevant to determine the chemical potential, due to the high specific surface, and hence the equilibrium value of interstitial O_2. A further contribution could be related to possible increase of the number of interstices near to the surface able to trap O_2 due to possible morphological changes of surface after silanol groups substitution.

Diffusion experiments performed on nanoparticles obtained by microemulsion method shows that this material has a behavior different with respect to fumed silica. Indeed, the PL band of interstitial O_2 is induced only by pre-treating the sample at 400 °C. Furthermore, the concentration of interstitial O_2 is lower than fumed silica having same size and it is almost independent on microemulsion particles size. This behavior was related to internal porosity of microemulsion samples, evidenced by high silanol concentration and TEM images. In particular, the equality among O_2 PL amplitude in samples with different size suggests that the internal porosity is size independent.

As a further investigations, the study of the diffusion process in non porous silica nanoparticles obtained by microemulsion method could be very interesting. Indeed, due to their sharp size distribution, such a study could elucidate the role of the size in both the transport and the equilibrium value of interstitial O_2. Furthermore, diffusion experiments on these materials at temperatures lower than those investigated in this thesis could better clarify the role played by the surface dissolution as a function of the size of the particles.

In order to overcome the difficulties related to size in smaller nanoparticles, the diffusion could also be investigated by means of the reaction among diffusing O_2 molecules and radiation induced point defects in silica nanoparticles. Indeed this process depends not only on the surface dissolution but even on the subsequent diffusion of O_2 through the nanoparticles.

Finally, a study of the diffusion process on density could be carried out by performing experiments on densified silica nanoparticles.

Appendix A

Diffusion process in silica nanoparticles distributed by Sigma Aldrich

The diffusion process in commercial silica nanoparticles produced by Evonik industries was investigated in chapters 3 and 4. In order to verify that the features of diffusion process are not peculiar of these nanoparticles, experiments were carried out on silica nanoparticles distributed by Sigma Aldrich that are not produced by Evonik industries. In particular, experiments were performed on hydrophilic silica nanoparticles having specific surface 200 m^2/g (Sig200) or specific surface 200 m^2/g and average diameter 12 nm (Sig200-12) that are similar to AE200 (see Tables 2.1 and 2.2). Sorption kinetics shown in Fig. A.1 were performed at 127 °C and 6 or 66 bar O_2 external pressure on AE200 and samples distributed by Sigma Aldrich having same values of specific surface. These kinetics are equal within experimental errors suggesting that kinetics aspects are equal in the investigated samples.

Raman/PL spectra shown in Fig. A.2 are relative to as-received and thermally treated AE200 and Sigma Aldrich samples having same values of specific surface. Thermal treatment was performed in O_2 at 127 °C and 35 bar for a time long enough to reach diffusive equilibrium. As can be seen by comparing the amplitude of interstitial O_2 PL band, peaked at 1538 cm^{-1}, O_2 concentrations are equal both in as-received samples and in samples treated in O_2. Raman/PL spectra of as-received Sig395 and AE380 samples, having specific surface 395 and 380 m^2/g (see Tables 2.1 and 2.2), are shown in the upper panel of Fig. A.3 whereas Raman/PL spectra relative to diffusive equilibrium in O_2 atmosphere at 127 °C and 35 bar are in the lower panel of Fig. A.3. PL bands of interstitial O_2 are equal in these two samples, both in as-received and treated ones as expected on the basis of their similar morphology. Experimental data shown in the previous figures suggest that the features of diffusion process found in nanoparticles produced by Evonik industries are general.

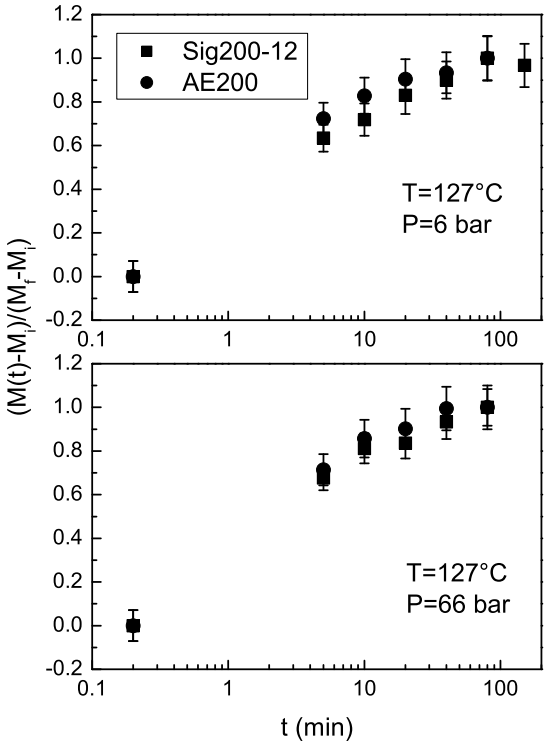

Figure A.1: Sorption kinetics in Sig200-12 and AE200 samples (average radius of primary particles equal to 6 nm) at 127 °C and 6 or 66 bar O_2 external pressure.

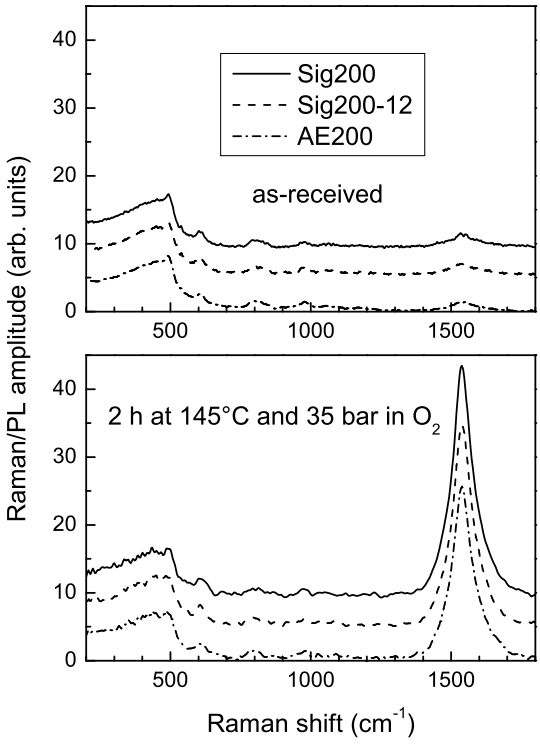

Figure A.2: Raman/PL spectra of as-received and thermally treated samples distributed by Sigma Aldrich having specific surface 200 m^2/g. Raman spectrum of AE200 is also reported for comparison. Raman/PL spectra of thermally treated samples are relative to diffusive equilibrium at 127 °C and 35 bar O_2 external pressure.

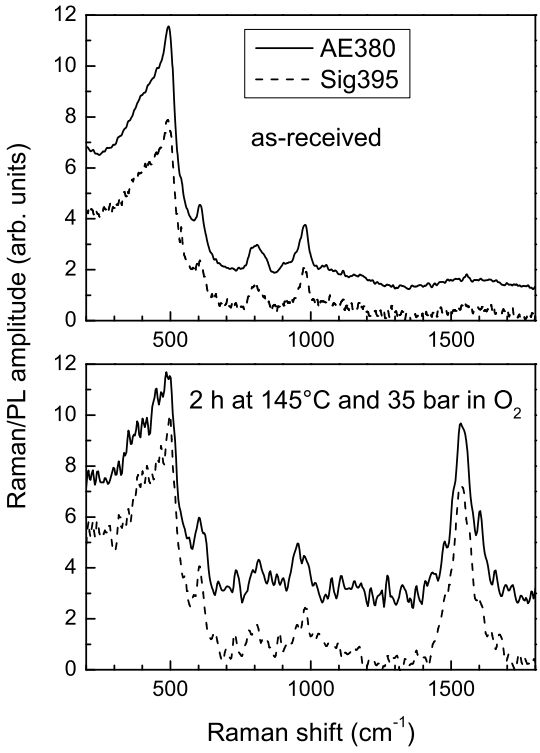

Figure A.3: Raman/PL spectra of as-received and thermally treated Sig395 sample. Raman spectrum of AE380 is also reported for comparison. Raman/PL spectra of thermally treated samples are relative to diffusive equilibrium at 127 °C and 35 bar O_2 external pressure.

Appendix B

Origin of interstitial O_2 in as-received samples

Interstitial O_2 is present in as-received silica nanoparticles produced by Evonik Industries or distributed by Sigma Aldrich, as can be seen by the presence of PL band at 1538 cm^{-1} in Raman/PL spectra of as-received samples. This O_2 could be either trapped during manufacturing process or trapped after the synthesis. Fig. B.1 shows the Raman/PL spectra of as-received AEOX50 sample (average radius of primary particles 20 nm), after a thermal treatment in air at 157 °C and two years after the treatment. The thermal treatment time was long enough for reaching diffusive equilibrium with ambient atmosphere. The O_2 content at equilibrium is lower than in as-received sample. Since the sample is held in ambient atmosphere, O_2 can diffuse into it and two years after the outgassing treatment, the O_2 content is equal to that of as-received sample. This finding suggests that O_2 in as-received samples is the value relative to diffusive equilibrium under ambient conditions. The presence of interstitial molecules and the relatively short time for equilibrium to be reached, even at room temperature, should be taken into account for the use of nanometer silica-based systems.

On the other side this is an interesting aspect related to the silica world in that the material should be subject to a "breathing" natural process by which silica incorporates O_2 or release it in ambient atmosphere, depending on temperature, and this breathing process could be of major concern projecting down to the nanoscale materials.

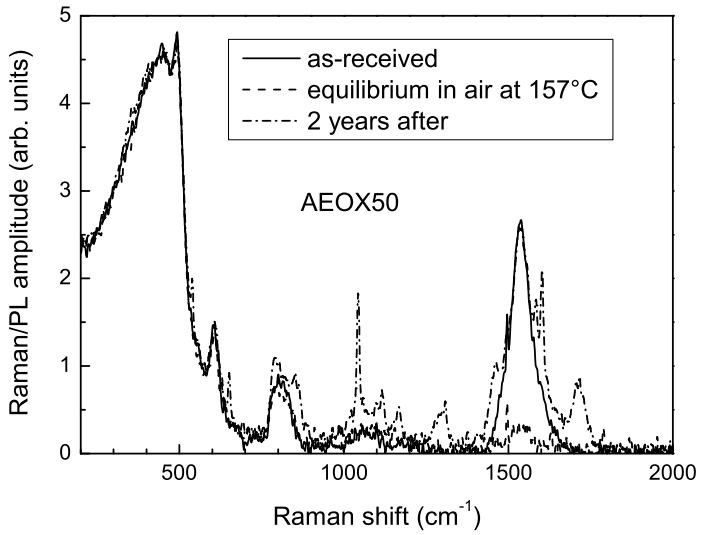

Figure B.1: Raman/PL spectra of as-received AEOX50 sample, after outgassing at 157 °C in air and 2 years after the outgassing treatment.

Appendix C

List of related papers

List of published papers related to this thesis:

• G. Iovino, S. Agnello, F. M. Gelardi, and R. Boscaino "O_2 Diffusion in Amorphous SiO_2 Nanoparticles Probed by Outgassing" J. Phys. Chem. C 2012, 116, 11351-11356

• G. Iovino, S. Agnello, F. M. Gelardi, and R. Boscaino "Effects of Pressure, Temperature, and Particles Size on O_2 Diffusion Dynamics in Silica Nanoparticles" J. Phys. Chem. C 2013, 117, 9456-9462

• G. Iovino, S. Agnello, F. M. Gelardi "Dependence of O_2 diffusion dynamics on pressure and temperature in silica nanoparticles" J. Nanopart. Res. (2013) 15:1876

• G. Iovino, M.A. Malvindi, S. Agnello, G. Buscarino, A. Alessi, P.P. Pompa, F.M. Gelardi "Optical and morphological properties of infrared emitting functionalized silica nanoparticles" Materials Chemistry and Physics 142 (2013) 763-769

• A. Alessi, G. Iovino, G. Buscarino, S. Agnello, and F. M. Gelardi "Entrapping of O_2 Molecules in Nanostructured Silica Probed by Photoluminescence" J. Phys. Chem. C 2013, 117, 2616-2622

• S. Agnello, M. Cannas, G. Iovino, L. Vaccaro, and F. M. Gelardi "Photoluminescence and diffusion properties of O_2 molecules in amorphous SiO_2 nanoparticles" Phys. Status Solidi C 10, No. 4 (2013)

• S. Agnello, D. Di Francesca, A. Alessi, G. Iovino, M. Cannas, S. Girard, A. Boukenter, and Y. Ouerdane "Interstitial O_2 distribution in amorphous SiO_2 nanoparticles determined by Raman and photoluminescence spectroscopy" J. Appl. Phys. 114, 104305 (2013)

Bibliography

[1] G. Pacchioni, L. Skuja, and D. L. Griscom, eds., *Defects in SiO_2 and Related Dielectrics: Science and Technology*. Dordrecht: Kluwer Academic Publishers, 2000.

[2] H. S. Nalwa, ed., *Silicon Based Materials and Devices*. San Diego: Academic Press, 2001.

[3] A. Burns, H. Ow, and U. Weisner *Chem. Soc. Rev.*, vol. 35, pp. 1028–1042, 2006.

[4] S. Watcharotone, D. A. Dikin, S. Stankovich, R. Piner, I. Jung, G. H. B. Dommett, G. Evmenenko, S.-E. Wu, S.-F. Chen, C.-P. Liu, S. T. Nguyen, and R. S. Ruoff *Nanoletters*, vol. 7, pp. 1888–1892, 2007.

[5] M. A. Noginov, G. Zhu, A. M. Belgrave, R. Bakker, V. M. Shalaev, E. E. Narimanov, S. Stout, E. Herz, T. Suteewong, and U. Wiesner *Nature*, vol. 460, pp. 1110–1113, 2009.

[6] K. Kajihara, T. Miura, H. Kamioka, A. Aiba, M. Uramoto, Y. Morimoto, M. Hirano, L. Skuja, and H. Hosono *J.of Non-Cryst. Sol.*, vol. 354, pp. 224–232, 2008.

[7] J. Lu, M. Liong, S. Sherman, T. Xia, M. Kovochich, A. E. Nel, J. Zink, and F. Tamanoi *Nano Biotechnology*, vol. 3, pp. 89–95, 2007.

[8] J. Lu, M. Liong, J. Zink, and F. Tamanoi *Small*, vol. 3, pp. 1341–1346, 2007.

[9] C. Hom, J. Lu, and F. Tamamoi *J. Mater. Chem.*, vol. 19, pp. 6308–6316, 2009.

[10] J.-H. Park, L. Gu, G. von Maltzahn, E. Ruoslahti, S. N. Bhatia, and M. J. Sailor *Nature Mat.*, vol. 8, pp. 331–336, 2009.

[11] S. Santra, P. Zhang, K. Wang, R. Tapec, and W. Tan *Anal. Chem.*, vol. 73, p. 4988, 2001.

[12] T. Watanabe, K. Tatsumura, and I. Ohdomari *Phys. Rev. Lett.*, vol. 96, pp. 196102 1–4, 2006.

[13] H. Ohta, T. Watanabe, and I. Ohdomari *Phys. Rev. B.*, vol. 78, pp. 155326 1–7, 2008.

[14] B. E. Deal and A. S. Grove *J. Appl. Phys.*, vol. 36, pp. 3770–3776, 1965.

[15] S. Agnello, M. Cannas, L. Vaccaro, G. Vaccaro, F. M. Gelardi, M. Leone, V. Militello, and R. Boscaino *J. Phys. Chem. C*, vol. 115, pp. 12831–12835, 2011.

[16] S. Agnello, R. Boscaino, M. Cannas, F. M. Gelardi, M. Leone, and V. Militello, "Nir nanoemitters based on silica for in-vivo applications and the related production process," p. Patent N. 0001399551 RM20104000174 19 aprile 2013 WO2011128855 A1, 2010.

[17] A. Stesmans, K. Clemer, and V. V. Afanas'ev *Phys. Rev. B*, vol. 72, p. 155335, 2005.

[18] T. Uchino, A. Aboshi, T. Yamada, Y. Inamura, and Y. Katayama *Phys. Rev. B*, vol. 77, p. 132201, 2008.

[19] A. Roder, W. Kob, and K. Binder *J. Chem. Phys.*, vol. 114, pp. 7602–7614, 2001.

[20] I. V. Schweigert, K. E. J. Lehtinen, M. J. Carrier, and M. R. Zachariah *Phys. Rev. B.*, vol. 65, pp. 235410 1–9, 2002.

[21] V. V. Hoang *J. Phys. Chem. B*, vol. 111, p. 12649, 2007.

[22] G. Vaccaro, *Structural Modification Processes in Bulk and Nano-sized Amorphous SiO_2 Systems*. Palermo: PhD thesis, 2011.

[23] G. Vaccaro, S. Agnello, G. Buscarino, and F. M. Gelardi *J. Phys. Chem. C*, vol. 114, pp. 13991–13997, 2010.

[24] G. Vaccaro, G. Buscarino, S. Agnello, A. Sporea, C. Oproiu, D. G. Sporea, and F. M. Gelardi *J. Phys. Chem. C*, vol. 116, pp. 144–149, 2012.

[25] C. Kittel and H. Kroemer, *Thermal Physics*. San Francisco: Freem and Company, 1980.

[26] K. A. Dill and S. Bromberg, *Molecular Driving Forces*. New York and London: Garland Science, 2003.

[27] J. E. Shelby, S. Keeton, and J. J. Iannucci *J. Appl. Phys.*, vol. 47, p. 3952, 1976.

[28] T. L. Hill, *Introduction to Statistical Thermodymics*. Reading, Mass.: Addison-Wesley, 1960.

[29] R. H. Fowler and E. A. Guggenheim, *Statistical Thermodynamics*. Cambridge: Cambridge University Press, 1939.

[30] R. M. Barrer and D. E. W. Waughn *J. Appl. Phys.*, vol. 63, p. 2275, 1967.

[31] J. E. Shelby *J. Appl. Phys.*, vol. 47, p. 135, 1976.

[32] J. F. Shackelford and J. S. Masaryk *J. Non-Cryst. Solids*, vol. 30, p. 127, 1978.

[33] C. M. Hartwig *J. Appl. Phys.*, vol. 47, p. 956, 1976.

[34] J. E. Shelby *J. Appl. Phys.*, vol. 48, p. 338, 1977.

[35] J. Crank, ed., *The mathematics of diffusion: Second Edition*. Oxford: Clarendon Press, 1979.

[36] A. Fick *Annln Phys.*, vol. 170, p. 59, 1855.

[37] P. Dennery and A. Krzywicki, *Mathematics for physicists*. New York: Dover Publication, Inc., 1996.

[38] R. M. Barrer *Proc. Phys. Soc.*, vol. 58, p. 321, 1946.

[39] G. S. Hartley *Discuss. Faraday Soc.*, no. 3, p. 223, 1948.

[40] L. F. Shampine *Q. appl. Math.*, vol. 30, p. 441, 1973.

[41] J. Crank and M. E. Henry *Trans. Faraday Soc.*, vol. 45, p. 636, 1949.

[42] J. Crank and S. M. Godson *Phil. Mag.*, vol. 38, p. 794, 1947.

[43] R. H. Doremus, ed., *Diffusion of reactive molecules in solids and melts*. New York: John Wiley and Sons, 2002.

[44] R. J. Borg and G. J. Dienes, *The Physical Chemistry of Solids*. Boston: Academic Press, 1992.

[45] J. E. Shelby and R. J. Eagan, *Treatise on Materials Science and Technology*, vol. 17. Academic Press, 1979.

[46] R. H. Doremus, *Glasses Science, 2nd ed.* New York: Wiley, 1994.

[47] J. E. Shelby *J. Am. Ceram. Soc.*, vol. 54, p. 125, 1971.

[48] W. M. Jones *J. Am. Chem. Soc.*, vol. 75, p. 3093, 1953.

[49] E. K. Beauchamp and L. C. Walters *Glass Thecnol.*, vol. 11, p. 139, 1970.

[50] R. H. Doremus, *Modern Aspect of the Vitreous State*, vol. 2. Washington, D. C.: Butterworth, 1962.

[51] J. E. Shelby and S. C. Keeton *J. Appl. Phys.*, vol. 45, p. 1458, 1974.

[52] J. H. Jeans, *Kinetics theory of gases*. Cambridge: Cambridge University Press, 1940.

[53] R. Ash and R. M. Barrer *Trans. Faraday Soc.*, vol. 59, p. 2260, 1963.

[54] H. L. Frisch and F. L. Galeener *J. Phys. Chem.*, vol. 62, p. 93, 1957.

[55] J. Crank and G. S. Park, *Diffusion in polymers.* New York: Academic Press, 1968.

[56] K. Kajihara, H. Kamioka, M. Hirano, T. Miura, L. Skuja, and H. Hosono *J.Appl. Phys.*, vol. 98, pp. 013529 1–7, 2005.

[57] S. Prager and F. A. Long *J. Am. Chem. Soc.*, vol. 73, p. 4072, 1951.

[58] R. J. Kokes, L. F. A., and J. L. Hoard *J. Chem. Phys.*, vol. 20, p. 1711, 1952.

[59] A. Alfrey, E. F. Gurnee, and W. G. Lloyd *J. Polym. Sci.*, vol. C12, p. 249, 1966.

[60] R. D. Shannon *Acta Crystallogr.*, vol. A32, p. 751, 1976.

[61] L. Pauling and E. B. Wilson, *Introduction to Quantum Mechanics.* New York: McGraw-Hill, 1935.

[62] J. P. Lowe, *Quantum Chemistry.* San Diego, CA: Academic Press, 1978.

[63] C. Kittel, *Quantum Theory of Solids, second ed.* New York: Wiley, 1987.

[64] G. Nakayama and S. J. F. *J. Non-Cryst. Solids*, vol. 126, p. 249, 1990.

[65] M. R. Carrol and E. M. Stolper *Geochim. Cosmochim. Acta*, vol. 55, p. 211, 1991.

[66] O. L. Anderson and D. A. Stuart *J. Am. Chem. Soc.*, vol. 37, p. 573, 1954.

[67] J. Frenkel, *Kinetic Theory of Liquids.* Oxford: Oxford University Press, 1946.

[68] J. A. E. Desa, A. C. Wright, J. wong, and N. R. Sinclair *J. Non-Cryst. Solids*, vol. 51, p. 57, 1982.

[69] R. L. Mozzi and B. E. Warren *J. Appl. Cryst.*, vol. 2, p. 164, 1969.

[70] R. Zallen, ed., *The physics of amorphous solids.* New York: Wiley-Interscience, 1983.

[71] W. H. Zachariasen *J. Amer. Chem. Soc.*, vol. 54, p. 3841, 1932.

[72] R. Wyckoff, *Crystal Structures.* New York: Interscience, 1951.

[73] R. A. B. Devine, J. P. Duraud, and E. Dooryhe, *Structure and Imperfections in Amorphous and Crystalline Silicon Dioxide.* New York: John Wiley and Sons, 2000.

[74] A. C. Wright *J. Non-Cryst. Solids*, vol. 106, p. 1, 1988.

[75] A. C. Wright, *Experimental Techniques of Glass Science.* Westerville: Amer. Ceram. Soc., 1993.

[76] J. P. Rino, I. Ebbsjo, R. K. Halia, A. Nakano, and P. Vashishta *Phys. Rev. B*, vol. 47, p. 3053, 1993.

[77] B. Hehlen *J. Phys. Condens. Matter*, vol. 22, p. 025401, 2010.

[78] F. L. Galeener *Solid State Commun.*, vol. 44, p. 1037, 1982.

[79] F. L. Galeener *Phys. Rev. B*, vol. 19, pp. 4292–4297, 1979.

[80] C. Kittel, *Introduction to Solid State Physics.* New York: John Wiley and Sons, 1981.

[81] R. Bruckner *J. Non-Cryst. Solids*, vol. 5, p. 281, 1971.

[82] R. Bruckner *J. Non-Cryst. Solids*, vol. 5, p. 123, 1970.

[83] G. Hetherington and K. H. Jack *Phys. Chem. Glasses*, vol. 3, p. 129, 1962.

[84] G. E. Walrafen *J. Chem. Phys.*, vol. 50, p. 560, 1969.

[85] V. Plotnichenko, V. Sokolov, and E. Dianov *J. Non-Cryst. Solids*, vol. 261, p. 186, 2000.

[86] L. Nuccio, S. Agnello, and R. Boscaino *Appl. Phys. Lett.*, vol. 93, pp. 151906 1–3, 2008.

[87] D. C. Harris and M. D. Bertolucci, *Symmetry and spectroscopy.* New York: Oxford University Press, 1978.

[88] B. Bransden and C. J. Joachain, *Physics of atoms and molecules.* Longman Group Limited, 1983.

[89] G. Herzberg, *Spectra of Diatomic Molecules.* New York: Van Nostrand Reinhold Co., 1950.

[90] C. Schweitzer and R. Schmidt *Chem. Rev.*, vol. 103, p. 1658, 2003.

[91] R. S. Mullikan *Rev. Mod. Phys.*, vol. 4, p. 1, 1932.

[92] J. W. Ellis and H. O. Z. Kneser *Phys.*, vol. 86, p. 583, 1933.

[93] K. J. Ritter and T. D. Wilkerson *J. Mol. Spectrosc.*, vol. 121, p. 1, 1987.

[94] J. F. Noxon *Can. J. Phys.*, vol. 39, p. 1110, 1961.

[95] A. N. Macpherson, T. G. Truscott, and P. H. Turner *J. Chem. Soc., Faraday Trans.*, vol. 90, p. 1065, 1994.

[96] W. B. Mims *Phys. Rev. B*, vol. 5, p. 2409, 1972.

[97] J. M. Wessels and M. A. J. Rodgers *J. Phys. Chem.*, vol. 99, p. 17586, 1995.

[98] R. D. Scurlock and P. R. Ogilby *J. Phys. Chem.*, vol. 91, p. 4599, 1987.

[99] L. Skuja and B. Guttler *Phys. Rev. lett.*, vol. 77, pp. 2093–2096, 1996.

[100] L. Skuja, B. Guttler, and D. Schiel *Glass Sci. Technol.*, vol. 71C, p. 73, 1998.

[101] K. Kajihara, H. Kamioka, M. Hirano, T. Miura, L. Skuja, and H. Hosono *J.Appl. Phys.*, vol. 98, pp. 013528 1–5, 2005.

[102] S. R. Dill, *Physics of amorphous materials*. New York: Longman Group Limited, 1983.

[103] F. Norton *Nature*, vol. 191, p. 701, 1961.

[104] R. M. Barrer, *Diffusion in and through Solids*. Cambridge: Cambridge University Press, 1951.

[105] H. Daynes *Proc. Roy. Soc.*, vol. 97, p. 286, 1920.

[106] C. J. Han and H. C. R. *J. Appl. Phys.*, vol. 135, p. 1824, 1988.

[107] S. Rigo, F. Rochet, B. Agius, and A. Straboni *J. Elettrochem. Soc.*, vol. 129, p. 867, 1982.

[108] F. Rochet, S. Rigo, M. Froment, C. d'Anterroches, C. Maillot, H. Roulet, and G. Dufour *Adv. Phys.*, vol. 35, p. 237, 1986.

[109] J. A. Costello and R. E. Tressler *J. Elettrochem. Soc.*, vol. 131, p. 1944, 1984.

[110] E. Rosencher, A. Straboni, S. Rigo, and G. Amsel *Appl. Phys. Lett.*, vol. 34, p. 254, 1979.

[111] F. Rochet, B. Agius, and S. Rigo *J. Elettrochem. Soc.*, vol. 131, p. 914, 1984.

[112] K. Kajihara, T. Miura, H. Kamioka, M. Hirano, L. Skuja, and H. Hosono *Phys. Rev. B*, vol. 83, pp. 064202 1–12, 2011.

[113] L. Skuja, B. Guttler, D. Schiel, and A. R. Silin *J. Appl. Phys.*, vol. 83, pp. 6106–6110, 1998.

[114] G. Hetherington and K. H. Jack *Phys. Chem. Glasses*, vol. 5, p. 147, 1964.

[115] T. Yamada, M. Nakajima, T. Suemoto, and T. Uchino *J. Phys. Chem. C*, vol. 111, p. 12973, 2007.

[116] A. Alessi, S. Agnello, G. Buscarino, and F. M. Gelardi *J. Raman Spectrosc.*, vol. 44, p. 810, 2013.

[117] C. M. Hartwig and L. A. J. Rahn *J. Chem. Phys.*, vol. 67, pp. 4260–4261, 1977.

[118] R. H. Stolen and G. E. Walrafen *J. Chem. Phys.*, vol. 64, pp. 2623–2631, 1976.

[119] C. J. Brinker and G. W. Scherer, eds., *Sol-Gel Science*. San Diego: Academic Press, Inc., 1 ed., 1990.

[120] V. M. Gun'ko and A. A. Chuiko, *Colloidal Silica*. New York: Taylor and Francis Group, 2006.

[121] F. A. Cotton and G. Wilkinson, *Advanced inorganic chemistry*. New York: Wiley-Interscience, 1972.

[122] C. A. Fyfe, G. C. Gobbi, and G. J. Kennedy *J. Phys. Chem.*, vol. 89, p. 277, 1985.

[123] L. Zhuravlev *Langmuir*, vol. 3, p. 316, 1987.

[124] A. Alessi, G. Iovino, G. Buscarino, S. Agnello, and F. M. Gelardi *J. Phys. Chem. C*, vol. 117, pp. 2616–2622, 2013.

[125] A. Burneau and O. Barres *Langmuir*, vol. 6, p. 1364, 1990.

[126] T. Uchino, A. Aboshi, S. Kohara, Y. Ohishi, M. Sakashita, and K. Aoki *Phys. Rev. B*, vol. 69, p. 155409, 2004.

[127] G. Buscarino, V. Ardizzone, G. Vaccaro, S. Agnello, and F. M. Gelardi *J.Appl. Phys.*, vol. 108, pp. 074314 1–9, 2010.

[128] B. A. Morrow and A. J. McFarlain *J. Phys. Chem.*, vol. 96, pp. 1395–1400, 1992.

[129] K. Kajihara, M. Hirano, M. Uramoto, Y. Morimoto, L. Skuja, and H. Hosono *J.Appl. Phys.*, vol. 98, p. 013527, 2005.

[130] Basic Characteristics of Aerosil, 4^{th} ed., Degussa, Frankfurt, 2001.

[131] http://www.aerosil.com/product/aerosil/en/products/hydrophilic-fumed-silica/pages/default.aspx, 2013.

[132] http://www.sigmaaldrich.com/materials-science/material-science-products.html?TablePage=18010474, 2013.

[133] W. Stober, A. Fink, and E. Bohn *Colloid Interface Sci.*, vol. 26, p. 62, 1968.

[134] J. Schulman, W. Stoeckenius, and L. Prince *J. Phys. Chem.*, vol. 63, p. 1677, 1959.

[135] H. Hauser, *Reverse Micelles*. New York: Plenum Press, 1984.

[136] M. Robbins, *Micellization, Solubilization and Microemulsions*, vol. 2. Plenum Press, 1977.

[137] I. Abarkan, T. Doussineau, and M. Smaihi *Polyhedron*, vol. 25, pp. 1763–1770, 2006.

[138] M. A. Malvindi, V. Brunetti, G. Vecchio, A. Galeone, C. R., and P. P. Pompa *Nanoscale*, vol. 4, pp. 486–495, 2012.

[139] A. Meijerink, *Luminescence of Solids*. New York: Plenum Press, 1998.

[140] H. H. Perkampus, *UV-vis spectroscopy and its application*. Berlin: Springer-Verlag, 1992.

[141] K. Nakamoto, *Infrared and Raman spectra of inorganic and coordination compounds*. New York: J.Wiley and Sons Inc., 1997.

[142] C. Cohen-Tannoudji, J. Dupont-Roc, and G. Grynberg, *Atom-photon interactions*. New York: John Wiley and Sons, 1992.

[143] S. Agnello *J. Appl. Phys.*, 2013.

[144] A. Bongiorno and A. Pasquarello, "Multiscale modeling of oxygen diffusion through the oxide during silicon oxidation," *Phys. Rev. B*, vol. 70, no. 19, pp. 195312 1–14, 2004.

[145] K. Kajihara, T. Miura, H. Kamioka, M. Hirano, L. Skuja, and H. Hosono *Journal of the Ceramic Society of Japan*, vol. 112, p. 559, 2004.

[146] S. Sohn and D. Kim *Chemosphere*, vol. 58, p. 115, 2005.

[147] J. Burgin, C. Guillon, P. Langot, F. Valle, B. Hehlen, and M. Foret *Phys. Rev. B*, vol. 78, p. 184203, 2008.

[148] G. Iovino, M. A. Malvindi, S. Agnello, G. Buscarino, A. Alessi, P. P. Pompa, and F. M. Gelardi *Mat. Chem. Phys.*, vol. 142, pp. 763–769, 2013.